Investigation into The Stability of Low-Inertia Micro-Grids

by

Ahmed Sheir

A thesis submitted to the
School of Graduate and Postdoctoral Studies in partial
fulfillment of the requirements for the degree of

Doctor of Philosophy in Electrical Engineering

Department Electrical and Computer Engineering

Faculty of Engineering and Applied Science

University of Ontario Institute of Technology (Ontario Tech University)

Oshawa, Ontario, Canada

May 2023

THESIS EXAMINATION INFORMATION

Submitted by: **Ahmed Sheir**

Doctor of Philosophy in **Electrical Engineering**

Investigation into The Stability of Low-Inertia Micro-Grids

An oral defense of this thesis took place on May 3rd, 2023 in front of the following examining committee:

Examining Committee:

Chair of Examining Committee	Dr. Zeinab El-Sayegh
Research Supervisor	Dr. Vijay K. Sood
Examining Committee Member	Dr. Ruth Milman
Examining Committee Member	Dr. Jing Ren
University Examiner	Dr. Tarlochan Sidhu
External Examiner	Dr. Afshin Rezaei-Zare, York University

The above committee determined that the thesis is acceptable in form and content and that a satisfactory knowledge of the field covered by the thesis was demonstrated by the candidate during an oral examination. A signed copy of the Certificate of Approval is available from the School of Graduate and Postdoctoral Studies.

Abstract

This work examines the stability of low inertia micro-grids (MGs). The lack of inertia in such power electronics dominated grid is a pressing matter that directly impacts its operation and stability. The investigated MG is formed by power electronics-based DC-AC converters; each of them is controlled by a virtual inertia controller to emulate certain characteristics of the existing synchronous generators-based grid. Two methods to study the stability of the given MG are discussed. The first one is a systematic construction of Lyapunov's energy function using Popov's criterion. This function is used to construct a region of attraction (ROA) that defines the stability boundary of the multi-VSG MG. A systematic calculation of the Critical Clearing Time is also introduced here to provide a quantitative measure of MG stability to complete the study.

The second method to study the MG stability is a proposed convex hull-based trajectory reversing method. The proposed method estimates and enlarges the ROA of grid connected VSGs MG, regardless of complexity of its model or control scheme. A family of trajectories initiated close to the VSG equilibrium point is generated and evaluated at successive time steps Δt. Then, convex hull algorithm finds the minimum region that contains all these points. Moreover, this work proposed a new technique to define the set of initial points needed by the algorithm. Compared to Lyapunov's method, the proposed method does not rely on finding a specific Lyapunov function or satisfying certain conditions. A case study is conducted to validate the algorithm performance and its estimated ROA by both methods.

Finally, this work also proposes a new nonlinear controller that enhances system response and increases stability. The proposed enhanced virtual inertia controller (EVIC) changes VSG inertia as a function of the disturbance introduced to the system. It relies on a simple tunable nonlinear equation without any extra sensors, complex algorithms, or prior knowledge of MG configuration or parameters. The results show the validity of the proposed EVIC to reduce oscillations in grid frequency and output power, as well as increase the area of attraction, and hence, MG overall stability and robustness.

AUTHOR'S DECLARATION

I hereby declare that this thesis consists of original work of which I have authored. This is a true copy of the thesis, including any required final revisions, as accepted by my examiners.

I authorize the University of Ontario Institute of Technology (Ontario Tech University) to lend this thesis to other institutions or individuals for the purpose of scholarly research. I further authorize University of Ontario Institute of Technology (Ontario Tech University) to reproduce this thesis by photocopying or by other means, in total or in part, at the request of other institutions or individuals for the purpose of scholarly research. I understand that my thesis will be made electronically available to the public.

Ahmed Sheir Ahmed Sheir

STATEMENT OF CONTRIBUTIONS

The main contributions of this work can be summarized as follows:

- Providing a large-signal stability study of power electronics dominated MG based on Popov's multivariable criterion which systematically constructs the Lyapunov function. Then estimation of the MG region of attraction (stability margins) is done based on the nearest unstable point. This is used to calculate the critical time of an MG in the presence of faults.
- Proposing an alternative method to study the large signal stability of power electronic dominated MGs. The proposed method and algorithm can be applied to any MGs regardless of its construction or model. moreover, the proposed method defines a fast and systematic way to solve its initial points problem and to reduce them to increase computational efficiency.
- Proposing a new enhanced virtual inertia controller EVIC which can further improve the MG stability margins and reduced power oscillations. The proposed controller provides adaptive alternating inertial dynamics in proportion to the applied disturbances.

Part of the work has been published as:

1. Ahmed Sheir, Ruth Milman and V. K. Sood, "***Large Signal Stability of Grid-Tied Virtual Synchronous Generator Using Trajectory Reversing***," IEEE Electrical Power and Energy Conference (EPEC 2022).

2. Ahmed Sheir and V. K. Sood, "***Effect of Low Pass Filter in Governor Model on Large Signal Stability of Virtual Synchronous Generator***," IEEE 12th International Symposium on Power Electronics for Distributed Generation Systems, (PEDG 2021).

3. J. Patel, **Ahmed Sheir** and V. K. Sood**, "*Impact of Sampling Time of Digital Controllers on The Harmonic Spectrum in Power Converters*,"** IEEE 12th International Symposium on Power Electronics for Distributed Generation Systems, (PEDG 2021).

4. Ahmed Sheir and V. K. Sood, "***Dual-Input H-bridge Based Three-Phase Cascaded Multilevel Converter for Utility-Scale Battery Applications***," IEEE Electrical Power and Energy Conference (EPEC), ON, 2021.

5. Youssef El Haj, **Ahmed Sheir**, Ruth Milman and V. K. Sood, "***Design of a Nonlinear Controller for a Two-Stage DC-AC Converter For DC-Link Drive Applications***," IEEE Electrical Power and Energy Conference (EPEC), ON, 2021.

6. Youssef El Haj, **Ahmed Sheir**, Ruth Milman and V. K. Sood, "***Robust Integral Sliding Mode Control of Non-minimum Phase DC-DC Converters***," 2020 IEEE Electrical Power and Energy Conference (EPEC), Edmonton, ON, 2020.

7. Ahmed Sheir and V. K. Sood, "***Cascaded Modular Converter with Reduced Output Voltage Ripple***," 2019 IEEE Electrical Power and Energy Conference (EPEC), Montreal, ON, 2019.

8. Ali Sunbul, **Ahmed Sheir** and V. K. Sood, "***High Performance Multilevel Power Factor Correction Boost-Buck Converter***," 2019 IEEE Electrical Power and Energy Conference (EPEC), Montreal, ON, 2019.

Sole authorship

I hereby certify that I am the sole author of this thesis and that no part of this thesis has been published or submitted for publication. I have used standard referencing practices to acknowledge ideas, research techniques, or other materials that belong to others. Furthermore, I hereby certify that I am the sole source of the creative works and/or inventive knowledge described in this thesis.

ACKNOWLEDGEMENTS

First and foremost, I am extremely grateful to my supervisor, Prof. Vijay K. Sood, for his support, invaluable advice, and his patience during my PhD study. His vast knowledge and experience encouraged me throughout my academic research.

I would also like to thank Dr. Ruth Milman for her guidance and continuous support during my study.

My gratitude extends to the Faculty of Electrical and Applied Science for the funding opportunity to undertake my studies at the Department of Electrical and Computer Engineering, University of Ontario Institute of Technology (Ontario Tech University).

Additionally, I would like to express my gratitude to my parents, brothers, and sister and to my child. Without their encouragement and understanding for the past few years, it would not have been possible for me to complete my study. To my one true friend, Thank you.

Above all, I would like to thank God for His Blessing in the completion of this thesis.

This work is dedicated to my late mother…

Samia

Contents

List of Tables

List of Figures

Abbreviations

AC	Alternating Current
HV	High Voltage
EHV	Extra High Voltage
UHV	Ultra High Voltage
RES	Renewable Energy Sources
PCC	Point of Common Coupling
ESS	Energy Storage System
MG	Micro-Grid
SG	Synchronous Generator
HVDC	High Voltage DC
VSG	Virtual Synchronous Generator
RoCoF	Rate of Change of Frequency
DG	Distributed Generation
P_m	Mechanical Power
P_e	Electrical Power
KE_i	Kinetic Energy of the Machine Rotor in MJ
P_d	Damping Power In MW
f	Grid Frequency
δ	Power Angle (Rotor Angle) (°)
ω	Deviation from Reference Frequency (Rad /s)
D	Damping Coefficient
M	Inertia Coefficient
Y_{ji}	Admittance Between Bus j And i
E	Bus Voltage
k_p	Active Power Droop Coefficient
k_q	Reactive Power Droop Coefficient
T_d	Filter Time Delay
x_g	Line Impedance
$V(x)$	Lyapunov Function Of X States

$f(\sigma)$	Nonlinear Term in Swing Equation
Re{}	Real Part
EVIC	Enhanced Alternating Inertia Controller

1. Introduction and literature review

1. 1. Introduction

AC power system was first introduced to the United States in 1885 and in 1886 the first 1-phase, 13-mile-long transmission line was installed to carry electricity generated by waterpower; this power was used only for lighting. A 2-phase system was later introduced by Tesla in 1888, and more importantly, he introduced the 3-phase system which started the transition to a poly-phase system. AC-based power systems benefit from cheaply available AC transformers which, without controls, enabled transmitting power at much higher voltages than generation voltages, which in return resulted in highly-efficient transmission lines [1], [2]. Generation voltages range from 13.8 kV to 24 kV, and they can be stepped up using transformers to higher voltages (HV) i.e., up to 230 kV, extra high voltage (EHV) up to 765 kV, or ultra high voltage (UHV) up to 1500 kV. In return, the capacity of the transmission line is significantly increased roughly by the square of the voltage (assuming that the thermal limit is maintained).

The search for more energy sources has continued, powered by the need to match the increasing demand in electricity. With oil, gas, coal facing political and environmental headwinds and increased awareness of their long-term impacts on global warming, renewable energy sources (RESs) become more attractive as they inherently provide an "endless" supply of energy with much less damage to the environment. The raw data as well as the ongoing transformation to RES in pioneering countries, such as Denmark, shows that 100% RES based generation is possible [3]. However, hybrid generation using small safe and efficient nuclear reactors powering steam turbines and synchronous generators (SGs), and RESs may be seen to be the future suppliers of electricity.

However, bringing in RESs to an already established AC power system raises many challenges mainly due to their intermittent and distributed nature. Many other technologies have merged to offer solutions for such challenges. Power electronic converters, in conjunction with proper control and energy storage systems (ESSs), were able to convert RESs to constant, dispatchable, and reliable generators which are compatible with current AC grid standards. Due to their distributed nature, transmission lines are needed to transfer

RESs from remote areas such as off-shore wind farms to the closest grid connection point. With the location limit, AC transmission lines are not suitable as they require transformers stations every 250 km or so. High voltage dc (HVDC) solves this issue by offering much higher efficiency and transmission voltages than what AC transmission lines provide [4].

Moreover, instead of remote large power generation stations that transfer all the generated power to remote consumers, a more integrated power generation / consumption approach is considered. In this, RES power is generated and consumed locally, forming a new structure concept in power systems, known as a micro-grid (MG). These MGs are to be interconnected to each other and to the main utility grid. Such integration, while it is economically and environmentally plausible, produces challenges to the overall grid stability and reliability.

Fundamentally, two basic metrics that define the operational behavior of the AC grid are its constant voltage and constant frequency (within a few percent of a nominal range). In a typical AC power system, the grid frequency reflects the balance between grid total power generation and its total power consumption. Hence, based on its deviation from its standard value (60 Hz in North America, and 50 Hz in Europe and other parts of the world), the generated power is to be reduced (if the frequency is higher) or increased (if the frequency is lower). Moreover, such deviations can be easily detected by power generation units and are used to enable equal or proportional load sharing among them. The rate of change of frequency (RoCoF) is an important criterion to study AC system stability at large [5]. It is also worth mentioning that this is not limited to large-scale utility grids or microgrids. Small-scale power systems also exist in ships, trains, and aircrafts. They operate on a wider range of frequencies from 16.7 Hz to 400 Hz, based on a trade-off between weight and efficiency [6].

What has been established so far is that by controlling grid frequency we can, in fact, guarantee system stability by matching the generated power to the consumed power. Also, based on its deviation from the nominal frequency, power sharing among multiple generating units can be achieved. Hence, the aim here is to reserve these characteristics while enabling more renewable energy integration and merging technology.

1. 2. Literature review

Over the years, the legacy electric grid has been successful to supply its customers with electricity at constant voltage and constant frequency during both steady-state and transient operations. This has been achieved by continuously balancing the input mechanical power with the output electrical power of each generating unit while maintaining the grid frequency substantially constant. During steady-state, to keep the load sharing between the connected generators (mostly SG) at the desired levels, the controller of each generator monitors the grid frequency and adjusts the amount of input power accordingly. During transient conditions, the system kinetic energy is stored in the rotating mass of each generator (collectively known as the grid inertia) and it allows a gradual change in the grid frequency in proportion to the amount of the load transient. This allows the other generators to gradually adjust their input power as well. Hence, the grid stability is preserved [1].

The energy stored in the inertia constant M of a SG is the maximum amount of kinetic energy a SG can release to supply its connected load (i.e. power reference) before losing its reference frequency and voltage [7]. By contrast, a power electronic converter does not possess any such kinetic energy buffers, hence, it has no "inertia" associated with it. This imposes a serious constraint to the power system stability as more renewable energy sources are continuously being added to the grid which rely on power electronics-based converters [8]. A lower grid inertia implies that the grid is more susceptible to fast dynamics which may result in poor regulation, cascaded failures, or even load shedding [9].

Different approaches are being taken to mitigate these issues from the grid-side and as well as the converter-side. From grid-side, instead of running fewer SGs when power electronics-based generation is increased (i.e. high penetration level), multiple SGs are run at partial loading to keep the grid inertia as high as possible [1]. The advantages of such a solution are a) There is no major modification of the up and running utility grid; b) It is an easy fix to deploy; c) It requires no modifications from power electronics-based generation; and d) It requires no energy storage to be added. The short comings of such a solution are that; a) It is a temporary fix, and it has an upper limit; b) SGs will be running at low efficiency which ultimately negate the original intention of reducing carbon emissions while increasing the overall production; and c) MGs are based on distributed generations

that localize power production and consumption which are by-and-large interfaced with power electronic converters. Thus, presence of SGs is limited if any.

A more practical solution, from the converters-side, is to take advantage of their fast response (in the range of hundreds of microseconds to a couple of milliseconds) to track a desired reference. That is, by solving the SG mathematical model online, a slower reference signal is generated that holds all characteristics of SGs and, more importantly, their inertial behavior. This solution was introduced in [10], [11] and was referred to as a virtual synchronous generator (VSG) or virtual synchronous machine (VISMA) [12], [13]. A similar concept was introduced in [14] as a synchronverter. This idea attracted much interest from different research groups such as the VSYNC project [10], [12], [15]–[21], Institute of Electrical Power Engineering at Clausthal University of Technology in Germany [22], Kawasaki Heavy Industries (KHI) [23], and ISE laboratory in Osaka University [24]–[28]. These virtual machines have proven to be effective in mimicking the desired SG characteristics and maintain MG stability at high penetration levels (ratio of RES based generation to conventional generation).

However, in the literature, mainly small-signal analysis is provided despite the fact that MGs are more likely to experience large-signal disturbances [29]–[32]. Moreover, large-signal modelling and stability are performed considering only one or two VSG MG references [33]–[35]. In these references, the VSG model is mostly based on an ideal machine model which is not suitable for power electronics converters [14], [34]. While many studies have been introduced in the literature that focus on estimating the region of attraction (stability) of SG and VSG, they either only based on deriving a Lyapunov or Lyapunov-like function for a MG with only one or two-VSGs [34], [35], or they lacked a systematic methodology to construct it for a MG with n-VSGs, as the focus is on enlarging the estimated region of attraction [36], [37]. By contrast, this work provides a large-signal stability study of a MG with n-VSGs through a systematic approach to model such a MG and estimate its region of attraction. The estimation method adopted here gives slightly more conservative results than the ideal estimation. However, it has considerably higher accuracy when compared with the reduced models introduced in [33]. It is therefore,

considered to be sufficient considering other operating limitations and assumed to-be-installed protection equipment. It is also preferred for its systematic construction.

Finally, many virtual inertia controllers are proposed in [35], [38] to enhance VSG performance and stability. However, in [24], [38] inertia controller discontinuously varies the inertia coefficient using a piecewise function, in which, the inertia coefficient has only two values (maximum and minimum) which are assigned based on the sign of the rate of variation of the power angle and rate of variation of the frequency (positive or negative). Thus, for any given small variation in either quantity, the inertia coefficient varies by a very large magnitude. Moreover, in the presence of measurement noise, there is no way to know the value of inertia assigned to a given VSG in the MG. This adds more ambiguity to the VSG parameters at any given operating point (even at steady state) and adds complexity to any MG stability analysis.

In [39], VSG inertia coefficient is varied between two levels based on a complex algorithm where a fuzzy-logic based AI algorithm is designed and trained to adjust the value of the inertia coefficient of a given VSG based on the rate of variation of its power angle and rate of variation of the frequency, instead of using a discontinuous piecewise function as in [24], [38]. While it provides a good adaptive behavior to the VSG, it adds to the system complexity and degrades the reliability. In this work, an enhanced virtual inertia controller using a simple analytical function is proposed which gives adaptive characteristics to the VSG controller. Variation of the inertia coefficient is proportional to the amount of variation of VSG's power angle and frequency instead of the sign of their product as in [24], [38], or a complex algorithm as in [39]. It also, has the advantage of being able to bring the VSG to a steady state more quickly by changing the inertia coefficient in a computable predictable manner.

1. 3. Problem statement

Compared to a legacy-type large-scale electric grid, power generation within new emerging micro-grids (MGs) is mostly dominated by renewable energy sources (RESs) or energy storage units fed by power electronic converters. Such converters do not have any rotating mass (inertia) or have very minimal inertia at best. Therefore, such a MG is referred to as a low-inertia MG. To overcome such issues, these converters are controlled in such a way to mimic similarly power rated synchronous generators (SGs). Hence, they are referred to as virtual synchronous generators (VSGs).

Determining the stability of a low-inertia MG becomes a challenge for two reasons:

1. First, due to their relatively small size (in terms of power ratings), they are more prone to be affected by large amplitude disturbances, such as loss of one of the VSGs, large load switching or faults. By comparison, the conventional grid has many interconnected SGs and many integrated transmission and distribution networks which makes it much more resilient to such disturbances. Studying small MGs, using linear techniques, does not provide an accurate estimation of stability, as in the presence of large amplitude disturbances, the non-linear terms (typically ignored in linear techniques) become dominant and can not be ignored. Nonetheless, non-linear techniques developed to study non-linear systems rely on finding proper bounding functions for the system using a set of predefined constraints. In other words, non-linear techniques do not have a systemic approach to study stability, unlike their linear techniques which have approaches such as Nyquist criterion, root locus etc., for studying them.
2. The second reason is that low-inertia MGs often contain many feeds from power electronics converters. This is due to:
    a) Low-power capability of power electronic switches, which limits their ability to manufacture high power converters (typically, above several megawatts each),
    b) The locations of different types of RESs which may not necessarily be in proximity of each other, hence, the term *distributed generation*; and

c) Structure and safety constraints, such as those for utility-scale battery banks which require specific construction with proper ventilation, safety, and access.

All these reasons make it more likely to have several power electronic converters within a MG. Therefore, a given MG can not be reduced satisfactorily to a single generating unit (single VSG) and single load bus, as is done by most of the previous work in the literature. Studying non-linear stability of such a high number of interconnected VSGs adds more complexity to the analysis in systematically constructing a proper Lyapunov function. Such a function is crucial in analysing the non-linear dynamics of a given MG under large-signal disturbances and estimate its dynamic behavior.

The problems in analysing low-inertia micro-grids can be summarized as follows:

- Due to their size and low-inertia, their stability can not be easily determined using linear techniques which necessitates conducting non-linear stability analysis.
- Power electronic-based MGs are mainly formed by many interconnected VSGs. Hence, approximating a given MG to a single power generating unit and load bus is not strictly accurate.
- Non-linear techniques, in general, do not have a systematic approach to analyse stability and demand different treatment of each system separately.
- Unlike SGs, both inertia and damping coefficients of such VSGs are configurable parameters even when the VSG is online. However, designing a reliable and robust virtual inertia-based controller is still a challenge.

The above statements summarize the challenges faced for analysing future power electronics-dominated and interconnected MGs. The aim of this work is then to develop a systematic approach to determine stability of a given MG, propose new ways to improve its margins, and tune its virtual inertia controllers.

2. Modelling and control of VSG based microgrid.

2. 1. Large-signal model

The stability in a MG is generally defined by the ability of the distributed generators (DGs) to maintain synchronism similar to a multi-machine power system [40]. Synchronism is defined as the relative motions between synchronized machines with respect to a reference angle. Such a reference angle can be set as the angle of the largest DG (i.e., DG with the highest installed Wh capacity and the highest sinking/sourcing capability). This is common practice in large-scale power system analysis where the reference angle is the angle of the generator with the highest inertia [1].

On the other hand, in a DG, a more suitable approach is to define the reference angle as the center of angle (COA) which is proportional to the inertia-weighted angles of all DGs. Such a concept is analogous to the definition of center of mass in mechanical systems [41]. The large-signal model defined here can be based on either definition and will be used to construct the Lyapunov function and compute the regions of attraction. And hence, facilitating the study of system stability in the presence of large disturbances. It is worth mentioning that the model introduced here does not assume the existence of an infinite bus in the power electronics-based MG, unlike other models introduced in the literature. Thus, this model is valid in both grid-connected and islanding operational modes by simply including the grid with high inertia and constant voltage. More importantly, future power system will be based on inter-connected MGs (through a high voltage direct current (HVDC) transmission line), and hence, infinite bus-based models will not describe properly the system.

In large-scale power system, from a physical and operational point of view, a system is stable if all connected synchronous generators can keep their synchronism after faults (large disturbances). In general, faults of interest can be line faults, disconnection of large generating unit or a large load transient. The latter two are more common in MGs, and hence, are a focus in this study [8]. Large disturbances create an unbalance between generation and load demand. Thus, a momentary input-output power unbalance occurs at each generating unit. In electro-mechanical based generation, this means a mismatch

between input mechanical power and output electrical power. Hence, based on power capacity and load sharing, some units will have accelerating power while others will have decelerating power.

The same definition is valid in MGs with power electronics-based DGs, where, each power converter is controlled in a way to mimic the behavior of a synchronous generator [25]. In other words, a virtual-inertia control block is added to their control loop, which converts them to virtual synchronous generators (VSGs). Nonetheless, assuming that such behavior is maintained despite the source of generation, the rate of change of frequency (RoCoF) is a function of the difference between the input (mechanical or virtual prime mover) and output power as is defined by the swing equation. Therefore, the swing equation provides a sufficient means to describe system dynamics and its energy transfer, which has been already used in a large-scale power system stability analysis [2].

Thus, in this work, assuming DGs in a MG display similar dynamic behavior under virtual inertia, the large-signal model of a MG is to be derived before applying the Lyapunov stability criteria. At this point, all DGs in the MG are synchronous generators, or virtual synchronous generators VSGs. Moreover, within this manuscript 'generator' or 'VSG converter' is a reference to all "synchronous-like" generation units, while 'machine' is strictly referred to as "actual synchronous generators". This is done for clearer representation and notation. Hence, mechanical input power, rotor kinetic energy, … etc., are equivalent to virtual mechanical input power, virtual kinetic energy … etc., respectively.

2. 1. 1. State space model of multi-VSG converter

In steady-state operation, for energy balance input mechanical power P_m is equal to the output electrical power P_e (assuming no losses), as follows [42] [43]:

$$P_m = P_e \tag{2.1}$$

Conventionally, P_m refers to the input mechanical power (generator's prime mover). However, in power electronics-based MG, it refers to the virtually calculated mechanical

power as will be explained later, and P_e refers to machine / VSG converter electrical output power. Following a disturbance, a mismatch occurs between input and output power which appears as a change in the kinetic energy and absorbed damping power for the i^{th} machine as follows:

$$\frac{d}{dt} KE_i + P_{d,i} = P_{m,i} - P_{e,i} \tag{2.2}$$

Where,

KE_i is the kinetic energy of the machine rotor in Mega Joules

$P_{d,i}$ is the damping power in MW

$P_{m,i}$ is the input mechanical power in MW

$P_{e,i}$ is the output electrical power in MW

and $i = 1, 2, 3, \ldots n$, where n is the total number of synchronous generators connected to the MG.

For a synchronous machine, the kinetic energy KE_i is proportional to the square of the rotational frequency f_i (rad/s). Thus, the change in the kinetic energy KE_i with respect to the kinetic energy at the synchronous frequency (f_o) KE_i^o can be expressed as follows:

$$KE_i = KE_i^o \left(\frac{f_i}{f_o}\right)^2 \tag{2.3}$$

If the deviation Δf_i from the synchronous frequency f_o is small enough, equation (2.3) can be written as:

$$KE_i = KE_i^o \left(\frac{\Delta f_i + f_o}{f_o}\right)^2 \tag{2.4}$$

$$KE_i = KE_i^o \left(1 + \frac{2\Delta f_i}{f_o}\right) \tag{2.5}$$

If the rotor angle with respect to a fixed reference is α_i of the i^{th} VSG converter, and δ_i is its angle with respect to a rotating synchronous reference $w_o t$, hence:

$$\delta_i = \alpha_i - w_o t \tag{2.6}$$

Where, w_o is the synchronous frequency in radians/s

Therefore, the change in the relative rotating angle δ_i is:

$$\frac{d\delta_i}{dt} = \frac{d\alpha_i}{dt} - w_o \tag{2.7}$$

$$\frac{d\delta_i}{dt} = 2\,\pi\,(f_i - f_o) = 2\,\pi\,\Delta f_i \cong w_i \tag{2.8}$$

Thus, w_i is the deviation (Δ) in frequency from the synchronous frequency under disturbed condition. It is important to note, where w_i is conventionally denoted the frequency in radians/sec, here it is denoted the deviation in frequency of each i^{th} VSG converter. That is, the frequency deviation is the quantity more related to this study, and for proper mathematical notation as using the notation Δw_i might be confusing with dw_i later.

For the first half of the left side of equation (2.2), the change in the kinetic energy can be expressed as follows:

$$\frac{d}{dt}\,KE_i = \frac{KE_i}{\pi f_o}\frac{d^2\delta}{dt^2} \tag{2.9}$$

For the second half, the damping power $P_{d,i}$ has two components. The first one is directly proportional to the deviation from the synchronous frequency w_i. The second one is the resultant of the asynchronous torque between all connected machines / VSG converters.

The total expression is the summation of the two components as follows:

$$P_{d,i} = D_i w_i + \sum_{j=1}^{n} D_{ij}\,(\frac{d\delta_i}{dt} - \frac{d\delta_j}{dt}) \tag{2.10}$$

In [1], [41], [42], the asynchronous torque is set to zero which significantly simplifies the equation and the modeling. Also, there is no need to emulate such behavior by VGS. The same approach is followed here as well.

Hence, equation (2.2) can be rewritten using equations (2.9) and (2.10) as follows:

$$\frac{H_i}{\pi f_o}\frac{d^2\delta_i}{dt^2} + D_i\frac{d\delta_i}{dt} = P_{m,i} - P_{el,i} \tag{2.11}$$

Where, $H_i = \frac{KE_i}{base\ MVA}$ and all quantities ($D_i,\ P_{m,i},\ P_{el,i}$) are expressed in $base\ MVA$.

Moreover, inertia coefficient $\frac{H_i}{\pi f_o}$ can be expressed as M_i as in [44]. Both are known as inertia coefficients but in different units. Equation (2.11) then represents the basic form of the swing equation of a synchronous DG (machine or VSG).

It is important to note that, while both the inertia coefficient M_i and the damping factor D_i are measured and defined once the synchronous generator is built, this is not the case in VSG converters (which essentially mimic and emulate the behavior of such generators). Therefore, defining the appropriate boundaries to select coefficients with respect to the available maximum power of the connected sources such as batteries or photovoltaic panels, and their maximum power sourcing / sinking capabilities form one of the main objectives of this study. As will be shown later, design criteria of M_i (and based upon the design of D_i) is based on dc-link inertia as it is more suitable for power electronics-based DGs [7].

Up to this point, the left-half side of the swing equation is defined and the problem statement of finding its coefficients is mentioned. Although, the right-half side of the equation seems simple and direct as it is a subtraction of the output power $P_{e,i}$ from the input power $P_{m,i}$. Calculating $P_{e,i}$ in terms of δ_i for a synchronous machine is complex. Fortunately, because the dynamics of the SG itself isn't the focus, rather than the dynamics of the VSG in a given MG, the following assumptions can be made without affecting the fidelity of the model [35], [43]:

a) The time constant of the network is negligible compared to the time constant of power-frequency control loop (which mimics the SG). In a VSG, this also implies that the converter time constant (and all its associated control loops which are defined by the overall system bandwidth), is negligible as well.

b) The VSG converter is defined by a constant voltage source equal to the steady state value prior to the fault (pre-fault). In a VSG, this voltage source is connected in series with a reactance which represents the output filter reactance.
c) The phase angle of the voltage source, correlated to the rotor angle or virtual angle, is δ_i.
d) The loads are represented as constant impedances. This is important to simplify the study of the MG stability in terms of inertia and damping constants, and converter's minimum output filter. However, constant power loads (CPLs) can be considered as well, which will change the reduced admittance matrix.
e) The input power is assumed to be constant before and after the faulty condition and during the clearing time t_{cr}. Input power $P_{m,i}$ is virtual mechanical power generated for example from power-frequency droop control unit.

These conditions enable the derivation of the expression of the active output power of $P_{e,i}$ as follows:

$$P_{e,i} = Re(E_i\, I_i) = Re(E_i\, \sum_{j=1}^{n} Y_{ij}\, E_j) \tag{2.12}$$

Where, $i = 1, 2, 3, \ldots n$ and $j = 1, 2, 3 \ldots n$

The admittance Y_{ij} represents the admittance connected between the i^{th} and jth generators. It is calculated from the reduced admittance matrix that describes the internal bus configuration of n^{th} multi-machine system [2]. In which the buses without generators are eliminated to simplify the model, despite masking the topological aspects of the MG at large (i.e., the way loads are connected to their respected buses and the way buses are connected to each other).

Now, let

$$E_i = |E_i| \angle \delta_i$$

$$Y_{ij} = G_{ij} + jB_{ij} = |Y_{ij}| \angle \phi_{ij}$$

$$G_{ij} = |Y_{ij}| cos\phi_{ij} \text{ and } B_{ij} = |Y_{ij}| sin\phi_{ij}$$

Hence, the active output power $P_{e,i}$ becomes:

$$P_{e,i} = |E_i|^2 G_{ii} + \sum_{j=1 \neq i}^{n} |E_j| |E_j| |Y_{ij}| \cos[\phi_{ij} - (\delta_i - \delta_j)] \quad (2.13)$$

The trigonometric function $\cos[\phi_{ij} - (\delta_i - \delta_j)]$ can be decomposed as follows:

$$\cos[\phi_{ij} - (\delta_i - \delta_j)] = \cos\phi_{ij} \cos(\delta_i - \delta_j) + \sin\phi_{ij} \sin(\delta_i - \delta_j)$$

Then,

$$P_{el,i} = |E_i|^2 G_{ii} + \sum_{j=1 \neq i}^{n} |E_j| |E_j| |Y_{ij}| \{\cos\phi_{ij} \cos(\delta_i - \delta_j) + \sin\phi_{ij} \sin(\delta_i - \delta_j)\} \quad (2.14)$$

For better representation, let:

$$D_{ij} = |E_j| |E_j| |Y_{ij}| \cos\phi_{ij} = |E_j| |E_j| G_{ij}$$

and

$$C_{ij} = |E_j| |E_j| |Y_{ij}| \sin\phi_{ij} = |E_j| |E_j| B_{ij}$$

Thus, equation (2.14) can be written as follows:

$$P_{el,i} = |E_i|^2 G_{ii} + \sum_{j=1 \neq i}^{n} \mathrm{D_{ij}} \cos(\delta_i - \delta_j) + \mathrm{C_{ij}} \sin(\delta_i - \delta_j) \quad (2.15)$$

The aim from manipulating equation (2.14) to become (2.15) is to mask out the power consumed by the impedance between the generators using the two constants D_{ij} and C_{ij}. Such power is assumed constant and does not provide any dynamics. This is valid under the assumptions stated above (from (a) to (e)), where, the voltages of all generators are constant, and no line switching occurs during fault / transient condition. Nevertheless, in power electronics-based MG, a change in bus voltage can occur due to the limit rate of change of dc supply side, e.g., battery storage unit, or short circuit protection. Therefore, the proposed model for multi-VSG MG at the end of this section will include such limitations.

This concludes the derivation of the right-hand side of the swing equation (2.2) and (2.11), as the generated output power $P_{e,i}$ is expressed in terms of δ_i.

Therefore, the swing equation becomes:

$$M_i \frac{d^2\delta_i}{dt^2} + D_i \frac{d\delta_i}{dt} = P_{ii} - P_{ij} \tag{2.16}$$

Where,

$$P_{ii} = P_{m,i} - |E_i|^2 G_{ii}$$

$$P_{ij} = \sum_{j=1 \neq i}^{n} \mathrm{D_{ij}} \cos(\delta_i - \delta_j) + \mathrm{C_{ij}} \sin(\delta_i - \delta_j)$$

Hence, by adding the term P_{ij}, equation (2.16) now describes the dynamics of the i^{th} synchronous generator with respect to the j^{th} machine. This is appreciated in studying, for example, the stability of MG with centralized batteries feeding VSG, while the rest of the converters act as current source converters (i.e., Photovoltaic inverters in grid connection mode). Therefore, the system stability will define the optimal battery size versus the maximum penetration level.

Finally, based on the afore mentioned discussion, the state space model of n generators are formulated as:

$$\dot{\delta}_\imath = w_i \qquad\qquad i = 1,2,3, \dots n$$

$$\dot{w}_\imath = -\frac{D_i}{M_i} w_i + \frac{P_{ii} - P_{ij}}{M_i} \qquad i = 1,2,3, \dots n \tag{2.17}$$

Moreover, the state space model in case n^{th} machine / VSG converter is taken as a reference:

$$\dot{\delta}_\imath - \dot{\delta}_n = w_i - w_n \qquad i = 1,2,3, \dots n-1$$

$$\dot{w}_\imath = -\left(\frac{D_i}{M_i} w_i - \frac{D_n}{M_n} w_n\right) + \frac{P_{ii} - P_{ij}}{M_i} - \frac{P_{nn} - P_{nj}}{M_n} \tag{2.18}$$

2. 1. 2. State space model of multi-VSG converters with stable equilibrium point (SEP) transferred to the origin.

To enable a systematic approach in constructing Lyapunov functions, it is important to have the system stable equilibrium point (SEP) at the origin. Therefore, the state space model of multi converters / machines is to be reformulated to transfer its post-fault SEP at the origin. This is done to construct the region of stability around the post-fault SEP [45].

The equilibrium point of the post-fault can be calculated from equation (2.17), as follows:

$$\dot{\delta_i} = w_i = 0 \tag{2.19}$$

$$P_{ii} = P_{ij} \tag{2.20}$$

Where,

$P_{ii} = P_{m,i} - |E_i|^2 G_{ii}$

$P_{ij} = \sum_{j=1 \neq i}^{n} \mathrm{D_{ij}} \cos(\delta_i - \delta_j) + \mathrm{C_{ij}} \sin(\delta_i - \delta_j)$

In fact, equation (2.20) contains n equations each in $n-1$ variables (δ_{ij}). Hence, only $n-1$ equations are needed to solve the system (as it is in $n-1$ variables). The remaining equation is then reserved as a constraining condition. It will help in preserving the solution formulated in equation (2.20) and satisfy the following summation:

$$\sum_{i=1}^{n} P_{ii} - P_{ij} = 0 \tag{2.21}$$

In other words, the power of center of angle (P_{COA}) (or center of mass) becomes zero. This implies that the system regains its steady-state angle and frequency as per the pre-fault condition. Also, it means that:

$$\sum_{i=1}^{n} P_{ii} = 0$$

and

$$\sum_{i=1}^{n} P_{m,i} - |E_i|^2 G_{ii} = 0$$

Thus, for post-fault the SEP is at $\delta_i = \delta_i^s$; where, δ_i^s is the relative stable angle (virtual rotor relative angle or in better term relative power angle) that is commonly corresponding to the slack bus angle (the VSG converter / machine with the highest power).

The solution of (2.20) at steady-state can be written as follows:

$$P_{m,i} - |E_i|^2 G_{ii} = \sum_{j=1 \neq i}^{n} \mathrm{D_{ij}} \cos(\delta_i - \delta_j^s) + \mathrm{C_{ij}} \sin(\delta_i - \delta_j^s) = P_{ij}(\delta^s) \qquad (2.22)$$

Hence, the swing equation is obtained with SEP at the origin, as follows:

$$M_i \frac{d^2\delta_i}{dt^2} + D_i \frac{d\delta_i}{dt} = P_{ij}(\delta^s) - P_{ij}(\delta) \qquad (2.23)$$

As an example, to construct the detailed state space model with SEP at the origin for a MG with four generators, the model is constructed as follows:

Based on equations (2.22) and (2.23), the state variables for four generators ($n = 4$) with the 4^{th} one taken as reference [42], [43] are listed as follows:

$$x = [w_1, w_2, w_3, w_4, \ (\delta_{14} - \delta_{14}^s), (\delta_{24} - \delta_{24}^s), (\delta_{34} - \delta_{34}^s)]^T \qquad (2.24)$$

Where

$\delta_{i4} = \delta_i - \delta_4$ for $(i = 1,2,3)$

For better notation, a shorthand σ_i variable is introduced as follows:

$$\sigma_1 = \delta_{14} - \delta_{14}^s \quad ; \sigma_2 = \delta_{24} - \delta_{24}^s \quad ; \sigma_3 = \delta_{34} - \delta_{34}^s$$

Hence, the state variables become:

$$x = [w_1, w_2, w_3, w_4, \quad \sigma_1, \sigma_2, \sigma_3]^T$$

It is worth mentioning that the state variable x is of the minimal order to represent the four generators system. Adding more states will be redundant and will not contribute to a

better system description. Moreover, it is clear from equation (2.22) from the summation side, that the effect of the relative angles is already included. Hence, these angles can be expressed as follows:

$$\sigma_k = \delta_{mn} - \delta_{mn}^s \qquad \text{for} \qquad m = 1, 2, 3, \ldots \qquad \text{and} \qquad n = m - 1 \tag{2.25}$$

Then,

$$\sigma_4 = \delta_{12} - \delta_{12}^s \quad ; \sigma_5 = \delta_{13} - \delta_{13}^s \quad ; \sigma_6 = \delta_{23} - \delta_{23}^s$$

Finally, the state space model can be arranged as follows [41]:

$$\left.\begin{aligned} \dot{x} &= Ax - B_1 f(\sigma) - B_2 g(\sigma) \\ \sigma &= Cx \\ x &= [w_1, w_2, w_3, w_4, \sigma_1, \sigma_2, \sigma_3]^T \\ \sigma &= [\sigma_1, \sigma_2, \sigma_3, \sigma_4, \sigma_5, \sigma_6]^T \\ f(\sigma) &= [f_1(\sigma_1), f_2(\sigma_2), f_3(\sigma_3), f_4(\sigma_4), f_5(\sigma_5), f_6(\sigma_6)]^T \\ g(\sigma) &= [g_1(\sigma_1), g_2(\sigma_2), g_3(\sigma_3), g_4(\sigma_4), g_5(\sigma_5), g_6(\sigma_6)]^T \end{aligned}\right\} \tag{2.26}$$

Where,

$$A = \begin{bmatrix} \frac{D_1}{M_1} & 0 & 0 & 0 & 0 & 0 & 0 \\ 0 & \frac{D_2}{M_2} & 0 & 0 & 0 & 0 & 0 \\ 0 & 0 & \frac{D_3}{M_3} & 0 & 0 & 0 & 0 \\ 0 & 0 & 0 & \frac{D_4}{M_4} & 0 & 0 & 0 \\ 1 & 0 & 0 & -1 & 0 & 0 & 0 \\ 0 & 1 & 0 & -1 & 0 & 0 & 0 \\ 0 & 0 & 1 & -1 & 0 & 0 & 0 \end{bmatrix}$$

$$C = \begin{bmatrix} 0 & 0 & 0 & 0 & 0 & 0 & 0 \\ 0 & 0 & 0 & 0 & 0 & 0 & 0 \\ 0 & 0 & 0 & 0 & 0 & 0 & 0 \\ 0 & 0 & 0 & 1 & -1 & 0 & 0 \\ 0 & 0 & 0 & 1 & 0 & 0 & -1 \\ 0 & 0 & 0 & 0 & 0 & 1 & -1 \end{bmatrix}$$

$$B_1 = \begin{bmatrix} \frac{1}{M_1} & 0 & 0 & \frac{1}{M_1} & \frac{1}{M_1} & 0 \\ 0 & \frac{1}{M_1} & 0 & \frac{-1}{M_2} & 0 & \frac{-1}{M_2} \\ 0 & 0 & \frac{1}{M_3} & 0 & \frac{-1}{M_3} & \frac{-1}{M_3} \\ \frac{-1}{M_4} & \frac{-1}{M_4} & \frac{-1}{M_4} & 0 & 0 & 0 \\ 0 & 0 & 0 & 0 & 0 & 0 \\ 0 & 0 & 0 & 0 & 0 & 0 \\ 0 & 0 & 0 & 0 & 0 & 0 \end{bmatrix}$$

$$B_2 = \begin{bmatrix} \frac{1}{M_1} & 0 & 0 & \frac{1}{M_1} & \frac{1}{M_1} & 0 \\ 0 & \frac{1}{M_2} & 0 & \frac{1}{M_2} & 0 & \frac{1}{M_2} \\ 0 & 0 & \frac{1}{M_3} & 0 & \frac{1}{M_3} & \frac{1}{M_3} \\ \frac{1}{M_4} & \frac{1}{M_4} & \frac{1}{M_4} & 0 & 0 & 0 \\ 0 & 0 & 0 & 0 & 0 & 0 \\ 0 & 0 & 0 & 0 & 0 & 0 \\ 0 & 0 & 0 & 0 & 0 & 0 \end{bmatrix}$$

$$f(\sigma) = \begin{bmatrix} |E_1||E_4|\, B_{14}\, (\sin(\sigma_1 + \delta_{14}^s) - \sin \delta_{14}^s) \\ |E_2||E_4|\, B_{24}\, (\sin(\sigma_2 + \delta_{24}^s) - \sin \delta_{24}^s) \\ |E_3||E_4|\, B_{34}\, (\sin(\sigma_3 + \delta_{34}^s) - \sin \delta_{34}^s) \\ |E_1||E_2|\, B_{12}\, (\sin(\sigma_4 + \delta_{12}^s) - \sin \delta_{12}^s) \\ |E_1||E_3|\, B_{13}\, (\sin(\sigma_5 + \delta_{13}^s) - \sin \delta_{13}^s) \\ |E_2||E_3|\, B_{23}\, (\sin(\sigma_6 + \delta_{23}^s) - \sin \delta_{23}^s) \end{bmatrix}$$

$$g(\sigma) = \begin{bmatrix} |E_1||E_4|\, G_{14}\, (\cos(\sigma_1 + \delta_{14}^s) - \cos\delta_{14}^s) \\ |E_2||E_4|\, G_{24}\, (\cos(\sigma_2 + \delta_{24}^s) - \cos\delta_{24}^s) \\ |E_3||E_4|\, G_{34}\, (\cos(\sigma_3 + \delta_{34}^s) - \cos\delta_{34}^s) \\ |E_1||E_2|\, G_{12}\, (\cos(\sigma_4 + \delta_{12}^s) - \cos\delta_{12}^s) \\ |E_1||E_3|\, G_{13}\, (\cos(\sigma_5 + \delta_{13}^s) - \cos\delta_{13}^s) \\ |E_2||E_3|\, G_{23}\, (\cos(\sigma_6 + \delta_{23}^s) - \cos\delta_{23}^s) \end{bmatrix}$$

Note: B_{ij} and G_{ij} are defined by equation (2.14) parameters.

Finally, in this study, the model is extended to include the following parameters: a) effect of dc-link inertia; b) effect of droop control unit with high bandwidth low-pass filter; c) effect of reduction in converter's output voltage due to added short-circuit protection.

a) Effect of dc-link inertia

In VSGs, virtual inertia is supplied by releasing a portion of energy stored within the converter's dc-link capacitor. Analogous to kinetic energy stored in SG's rotor ($H_i = \frac{KE_i}{base\ MVA}$), capacitor energy can be express as follows:

$$H_{ci} = \frac{C_{dc}\, E_i^2}{mi^2\, MVA} \tag{2.27}$$

Where,

H_{ci} is dc-link inertia constant,

E_i is VSG output voltage (Vrms),

mi is VSG modulation index,

MVA is VSG rated power in MVA.

However, it is not possible to drain all the energy stored in the dc-link capacitor as it will result in severe reduction in dc-link voltage, increase of converter's output harmonics and poor dynamics. Therefore, only a portion of this power is to be utilized based on maximum allowable voltage variation with respect to maximum allowable frequency deviation as follows:

$$H_{ci} = \frac{\Delta E_{i_{max}} C_{dc_1} E_i^2}{\omega_{max} mi^2 MVA} \tag{2.28}$$

Where, $\Delta E_{i_{max}}$ is maximum per unit change in VSG output voltage, ω_{max} is maximum per unit frequency deviation, and C_{dc_1} is the capacitance of dc-link capacitor.

b) Effect of droop control unit with high bandwidth low-pass filter

In the literature, a low-pass filter is added to the $\omega - P$ droop control loop of VSG to its virtual governor unit [46]. Such a low-pass filter is required to filter out measurement noise superimposed on the frequency or power measurement. Hence, these filters are either set with relatively high cut-off frequency or completely ignored. While filtration function is indeed required, such a low-pass filter also provides delay and slow change in droop control operating point with respect to grid disturbances. In other words, the low-pass filter ensures that virtual mechanical input power of VSG remains constant during grid disturbance which is a fundamental assumption in power system analysis as mentioned earlier. Nonetheless, if low-pass filter with high bandwidth (and hence, short delay) is used or completely removed, the model provided in (2.26) is no longer valid. In such a case, the swing equation is first updated as follows:

For droop control equation,

$$-\frac{1}{k_{p_i}}\frac{d\delta_i}{dt} + P_{ref,i} = P_{m,i} \tag{2.29}$$

VSG swing equation become:

$$M_i \frac{d^2\delta_i}{dt^2} = P_{ref,i} - P_{el,i} - \left(D_i + \frac{1}{k_{p_i}}\right)\frac{d\delta_i}{dt} \tag{2.30}$$

Where,

$P_{ref,i}$ is VSG setpoint at nominal frequency in p.u.

k_{p_i} is VSG droop coefficient (between 3 - 5%).

Remark: In (2.30) the reciprocal of k_{p_i} becomes dominant over per unit quantities such as D_i , $P_{ref,i}$ and $P_{el,i}$. This will completely change the dynamic behavior of VSG from what is expected. Hence, an investigation of such effects will be provided in later stages of this study.

c) Effect of reduction in converter's output voltage due to added short-circuit protection

As mentioned earlier, unlike a SG, over-load capabilities of a VSG are very limited due to the inherent limitation of its semiconductor switches. Thus, a current limiter block is added to the converter's internal control loop. This can result in changing the converter's mode of operation from being a voltage source to a current source if the applied disturbance is large enough. This translates into a reduction of the converter's output voltage in favor of supplying is maximum allowable current. Such an effect can be formulated similar to machine flux decay model [1] as follows:

$$\frac{dE_i}{dt} = -l_{I1}\left(E_i - E_{nom,i}\right) - l_{I2}\sum_{j=1}^{n} B_{ij}\,E_j\,(\cos\,\delta_{ij}^{s} - \cos\,\delta_{ij}) \qquad (2.31)$$

Where,

$\frac{dE_i}{dt}$ is variation in VSG output voltage in p.u.

$E_{nom,i}$ is VSG nominal output voltage in p.u.

l_{I1} and l_{I2} are arbitrary constants defined by the maximum and minimum current limits.

Finally, based on the effect of the afore mentioned parameters, the model introduced in this study is as follows:

$$\left.\begin{aligned} \dot{x} &= Ax - B_1 f(\sigma) - B_2 g(\sigma) \\ \sigma &= Cx \\ x &= [w_1, w_2, w_3, w_4, \sigma_1, \sigma_2, \sigma_3]^T \\ \sigma &= [\sigma_1, \sigma_2, \sigma_3, \sigma_4, \sigma_5, \sigma_6]^T \\ f(\sigma) &= [f_1(\sigma_1), f_2(\sigma_2), f_3(\sigma_3), f_4(\sigma_4), f_5(\sigma_5), f_6(\sigma_6)]^T \\ g(\sigma) &= [g_1(\sigma_1), g_2(\sigma_2), g_3(\sigma_3), g_4(\sigma_4), g_5(\sigma_5), g_6(\sigma_6)]^T \end{aligned}\right\} \quad (2.32)$$

Where,

$A =$

$$\begin{bmatrix} \frac{\omega_{max,1}\, mi_1^2 (D_1 + \frac{1}{k_{p_1}})}{\Delta E_{1_{max}}\, C_{dc_1}\, E_1^2} & 0 & 0 & 0 & 0 & 0 & 0 \\ 0 & \frac{\omega_{max,2}\, mi_2^2 (D_2 + \frac{1}{k_{p_2}})}{\Delta E_{2_{max}}\, C_{dc_2}\, E_2^2} & 0 & 0 & 0 & 0 & 0 \\ 0 & 0 & \frac{\omega_{max,3}\, mi_3^2 (D_3 + \frac{1}{k_{p_3}})}{\Delta E_{3_{max}}\, C_{dc_3}\, E_3^2} & 0 & 0 & 0 & 0 \\ 0 & 0 & 0 & \frac{\omega_{max,4}\, mi_4^2 (D_4 + \frac{1}{k_{p_4}})}{\Delta E_{4_{max}}\, C_{dc_4}\, E_4^2} & 0 & 0 & 0 \\ 1 & 0 & 0 & -1 & 0 & 0 & 0 \\ 0 & 1 & 0 & -1 & 0 & 0 & 0 \\ 0 & 0 & 1 & -1 & 0 & 0 & 0 \end{bmatrix}$$

$$C = \begin{bmatrix} 0 & 0 & 0 & 0 & 0 & 0 & 0 \\ 0 & 0 & 0 & 0 & 0 & 0 & 0 \\ 0 & 0 & 0 & 0 & 0 & 0 & 0 \\ 0 & 0 & 0 & 1 & -1 & 0 & 0 \\ 0 & 0 & 0 & 1 & 0 & 0 & -1 \\ 0 & 0 & 0 & 0 & 0 & 1 & -1 \end{bmatrix}$$

B_1

$$= \begin{bmatrix} \frac{\omega_{max,1}\, mi_1^2}{\Delta E_{1_{max}}\, C_{dc_1}\, E_1^2} & 0 & 0 & \frac{\omega_{max,1}\, mi_1^2}{\Delta E_{1_{max}}\, C_{dc_1}\, E_1^2} & \frac{\omega_{max,1}\, mi_1^2}{\Delta E_{1_{max}}\, C_{dc_1}\, E_1^2} & 0 \\ 0 & \frac{\omega_{max,1}\, mi_1^2}{\Delta E_{1_{max}}\, C_{dc_1}\, E_1^2} & 0 & \frac{-\omega_{max,2}\, mi_2^2}{\Delta E_{2_{max}}\, C_{dc_2}\, E_2^2} & 0 & \frac{-\omega_{max,2}\, mi_2^2}{\Delta E_{2_{max}}\, C_{dc_2}\, E_2^2} \\ 0 & 0 & \frac{\omega_{max,3}\, mi_3^2}{\Delta E_{3_{max}}\, C_{dc_3}\, E_3^2} & 0 & \frac{-\omega_{max,3}\, mi_3^2}{\Delta E_{3_{max}}\, C_{dc_3}\, E_3^2} & \frac{-\omega_{max,3}\, mi_3^2}{\Delta E_{3_{max}}\, C_{dc_3}\, E_3^2} \\ \frac{-\omega_{max,4}\, mi_4^2}{\Delta E_{4_{max}}\, C_{dc_4}\, E_4^2} & \frac{-\omega_{max,4}\, mi_4^2}{\Delta E_{4_{max}}\, C_{dc_4}\, E_4^2} & \frac{-\omega_{max,4}\, mi_4^2}{\Delta E_{4_{max}}\, C_{dc_4}\, E_4^2} & 0 & 0 & 0 \\ 0 & 0 & 0 & 0 & 0 & 0 \\ 0 & 0 & 0 & 0 & 0 & 0 \\ 0 & 0 & 0 & 0 & 0 & 0 \end{bmatrix}$$

B_2

$$= \begin{bmatrix} \frac{\omega_{max,1}\, mi_1^2}{\Delta E_{1_{max}}\, C_{dc_1}\, E_1^2} & 0 & 0 & \frac{\omega_{max,1}\, mi_1^2}{\Delta E_{1_{max}}\, C_{dc_1}\, E_1^2} & \frac{\omega_{max,1}\, mi_1^2}{\Delta E_{1_{max}}\, C_{dc_1}\, E_1^2} & 0 \\ 0 & \frac{\omega_{max,1}\, mi_1^2}{\Delta E_{1_{max}}\, C_{dc_1}\, E_1^2} & 0 & \frac{\omega_{max,1}\, mi_1^2}{\Delta E_{1_{max}}\, C_{dc_1}\, E_1^2} & 0 & \frac{\omega_{max,1}\, mi_1^2}{\Delta E_{1_{max}}\, C_{dc_1}\, E_1^2} \\ 0 & 0 & \frac{\omega_{max,3}\, mi_3^2}{\Delta E_{3_{max}}\, C_{dc_3}\, E_3^2} & 0 & \frac{\omega_{max,3}\, mi_3^2}{\Delta E_{3_{max}}\, C_{dc_3}\, E_3^2} & \frac{\omega_{max,3}\, mi_3^2}{\Delta E_{3_{max}}\, C_{dc_3}\, E_3^2} \\ \frac{\omega_{max,4}\, mi_4^2}{\Delta E_{4_{max}}\, C_{dc_4}\, E_4^2} & \frac{\omega_{max,4}\, mi_4^2}{\Delta E_{4_{max}}\, C_{dc_4}\, E_4^2} & \frac{\omega_{max,4}\, mi_4^2}{\Delta E_{4_{max}}\, C_{dc_4}\, E_4^2} & 0 & 0 & 0 \\ 0 & 0 & 0 & 0 & 0 & 0 \\ 0 & 0 & 0 & 0 & 0 & 0 \\ 0 & 0 & 0 & 0 & 0 & 0 \end{bmatrix}$$

$$f(\sigma) = \begin{bmatrix} |E_1||E_4|\, B_{14}\, (\sin(\sigma_1 + \delta_{14}^s) - \sin \delta_{14}^s) \\ |E_2||E_4|\, B_{24}\, (\sin(\sigma_2 + \delta_{24}^s) - \sin \delta_{24}^s) \\ |E_3||E_4|\, B_{34}\, (\sin(\sigma_3 + \delta_{34}^s) - \sin \delta_{34}^s) \\ |E_1||E_2|\, B_{12}\, (\sin(\sigma_4 + \delta_{12}^s) - \sin \delta_{12}^s) \\ |E_1||E_3|\, B_{13}\, (\sin(\sigma_5 + \delta_{13}^s) - \sin \delta_{13}^s) \\ |E_2||E_3|\, B_{23}\, (\sin(\sigma_6 + \delta_{23}^s) - \sin \delta_{23}^s) \end{bmatrix}$$

$$g(\sigma) = \begin{bmatrix} |E_1||E_4|\, G_{14}\, (\cos(\sigma_1 + \delta_{14}^s) - \cos \delta_{14}^s) \\ |E_2||E_4|\, G_{24}\, (\cos(\sigma_2 + \delta_{24}^s) - \cos \delta_{24}^s) \\ |E_3||E_4|\, G_{34}\, (\cos(\sigma_3 + \delta_{34}^s) - \cos \delta_{34}^s) \\ |E_1||E_2|\, G_{12}\, (\cos(\sigma_4 + \delta_{12}^s) - \cos \delta_{12}^s) \\ |E_1||E_3|\, G_{13}\, (\cos(\sigma_5 + \delta_{13}^s) - \cos \delta_{13}^s) \\ |E_2||E_3|\, G_{23}\, (\cos(\sigma_6 + \delta_{23}^s) - \cos \delta_{23}^s) \end{bmatrix}$$

And

$$\dot{E}_i = -l_{I1}\left(E_i - E_{nom,i}\right) - l_{I2}\sum_{j=1}^{n} B_{ij}\,E_j\,(\cos\,\delta_{ij}^{s} - \cos\,\delta_{ij})$$

The stability study conducted in the coming chapters will be based on this model. Unlike models introduced in the literature which are limited to two VSGs, this model provides a structure to model n VSGs. It also models unique properties of power electronics converters that are different from classical SGs. Next, the small-signal model is presented and used to design VSG control loops. This design is later used to validate stability margins and analysis using simulation and practical real-time systems.

2. 1. 3. Effect of Low-Pass Filter in Governor

Many efforts have been dedicated to properly select VSG control parameters, such as damping coefficient M and damping ratio D, and to study their effect on the system [38], [39]. However, the low-pass filters (LPFs) added to their virtual prime mover control blocks are mostly overlooked and neglected in large signal stability analysis [34].

A main reason for this is that, adding LPFs model to VSGs model transforms it to a non-autonomous system which requires a different treatment [47], [48]. This paper highlights the impact of such LPFs on VSG large-signal dynamics using a nonlinear model and geometrical approach. This is done by considering different time delays (that impact LPF bandwidth) to show how they affect VSG dynamics during its inertial action following a large system disturbance.

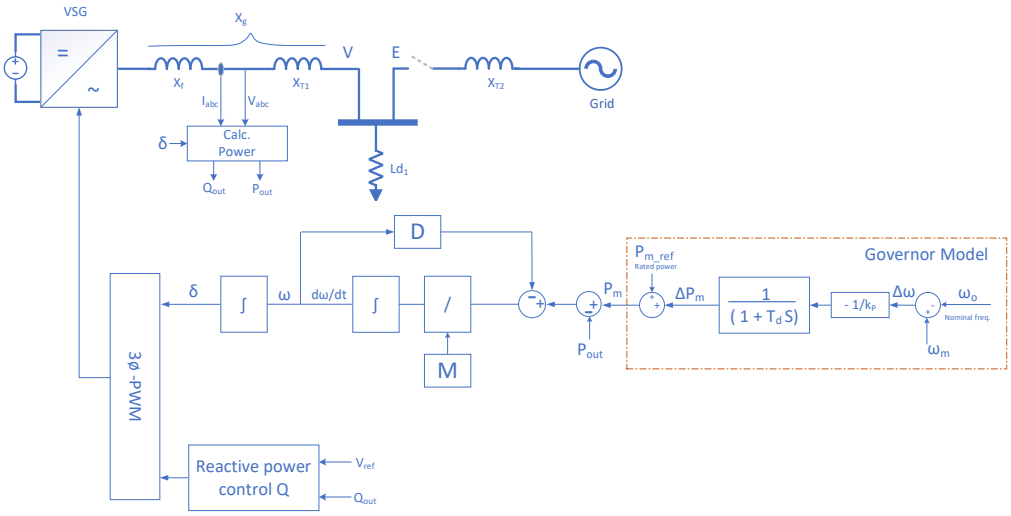

Fig. 2.1. VSG control loop block diagram

In steady-state operation, for energy balance, input mechanical power P_m equals to the output electrical power P_e (assuming no losses) $P_m = P_e$ [42] [43]. In SG, P_m refers to the input mechanical power (generator's prime mover). However, in VSG, it refers to the virtually calculated mechanical power using virtual inertia control loops as shown in Fig. 2.1. Following a disturbance, a mismatch occurs between input and output powers which appears as a deviation from the steady-state frequency and non-zero rate of change as follows:

$$\frac{H}{\pi f_o}\frac{d^2\delta}{dt^2} + D\frac{d\delta}{dt} = P_m - P_e \sin(\delta) \tag{2.33}$$

Where, $\mathrm{H} = \frac{KE}{base\ MVA}$, KE is the kinetic energy of the machine rotor in Mega Joules, δ is the power angle of the VSG with respect to the grid aggregated model, D is the damping coefficient, f_o is nominal frequency in Hz, P_m is the virtual mechanical input power, E is the grid side voltage, V is VSG side voltage, and x_g is impedance between VSG and grid side. All quantities are expressed in $base\ MVA$.

In the block diagram in Fig. 2.2, mechanical input power is supplied virtually by a governor model. It consists of $(\omega - P)$ droop control and low-pass filter. VSG output frequency ω is fed back to the $(\omega - P)$ droop control which computes the corresponding

adjustment to the virtual mechanical input power P_m based on its droop coefficient k_p , as shown in the Fig. 2.3 [1].

As mentioned before, the LPF in the governor model in VSG application is a means to reduce noise and line frequency ripple superimposed on the feedback measurements. Hence, these filters are either set with a relatively high cut-off frequency or completely ignored. While a filtration function is indeed required, such a low-pass filter also causes a delay and slow change in droop control operating point with respect to grid disturbances.

In other words, the low-pass filter ensures that virtual mechanical input power of VSG remains constant during a grid disturbance which is a fundamental assumption in power system analysis. Wherein, to achieve stable operation, generator's mechanical power reference which is set by the droop control outer loop (in SG or VSG), must slowly change to give time to the inertia controller (inner loop) to follow such a reference. Otherwise, if the mechanical power reference changes faster than the inertia controller, it will lead to unstable operation, even though VSG seems stable within a range. This issue is well studied in input-output stability in nonlinear systems [49]. Therefore, if LPF with high bandwidth (and hence, short delay) is used or completely removed, the assumption that mechanical power reference slowly changes is no longer valid, and hence, the model provided in (2.33) is not valid as well.

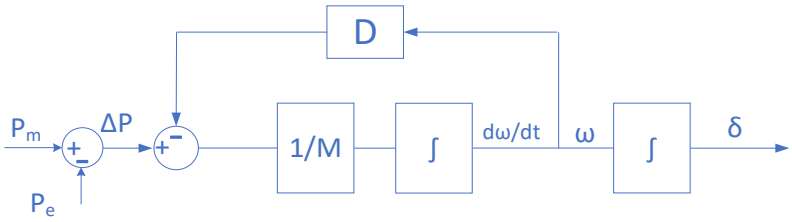

Fig. 2.2. Typical virtual inertia control block diagram

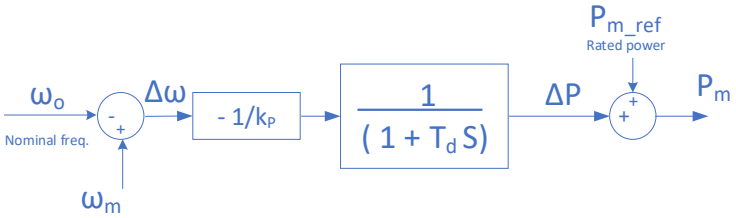

Fig. 2.3. Virtual governor model block diagram

To account for LPF effect, the time domain model of VSG control loop including governor model LPF is derived as follows:

LPF time domain model $q_{LPF}(t)$ is:

$$q_{LPF}(t) = \left(1 - e^{-\frac{t}{Td}}\right) \tag{2.34}$$

The mechanical power P_m of governor model, shown in the block diagram in Fig. 2.2., is as follows:

$$P_m = P_{m\_ref} + \left(-\frac{\Delta\omega}{k_p}\right) q_{LPF}(t) = P_{m\_ref} + \left(-\frac{\Delta\omega}{k_p}\right)\left(1 - e^{-\frac{t}{Td}}\right) \tag{2.35}$$

Where, Td is low-pass filter time delay (reciprocal of its cut off frequency), and P_{m_ref} is nominal power reference of given VSG. By combining equations (2.34) and (2.35), and considering $M = 2H$ as inertia coefficient in per unit system, the overall model in (2.33) is rewritten as follows:

$$M\frac{d^2\delta}{dt^2} = P_{m\_ref} + \left(-\frac{1}{k_p}\frac{d\delta}{dt}\right)\left(1 - e^{-\frac{t}{Td}}\right) - \frac{E\,V}{3\,x_g}\sin(\delta) - D\frac{d\delta}{dt} \tag{2.36}$$

Unlike the typical swing equation (2.33), equation (2.36) is a non-autonomous differential equation as adding LPF model explicitly expresses time t as system variable. This imposes a challenge in representing and analyzing large-signal stability as stability techniques deals in most cases with autonomous time invariant systems.

Here, the study of the impact of LPF is done using a geometrical approach to highlight the effect of its time delay Td , and consequently its bandwidth, on the converter's dynamic behavior. This is done by fixing LPF's Td and plotting the converter's vector field at successive time steps.

For the VSG design parameters listed in Table I, three time-constants for Td are considered to represent high, medium, and low bandwidth LPFs:

Table 2.1. VSG parameters

Parameter	Value
Virtual input power P_m	$0.4\ p.u.$
Base power P_e	$3.125\ MVA$
Grid power angle δ_g	$0\ rad$
Line impedance x_g	$0.41\ p.u.$
Bus line voltage E	$2.4\ kV$
Active power droop coefficient k_p	0.03
Reactive power droop coefficient k_q	0.03
Damping constant D	$1\ p.u.$
Inertial Constant H	$10\ s$

High bandwidth LPF

In the high bandwidth case, Td is set to 0.001s. After 0.01 second, the exponential term becomes very small which makes the droop term $\left(-\frac{1}{k_p}\frac{d\delta}{dt}\right)$ dominant as $\frac{1}{k_p}$ ≈33 (based on parameters in Table 2.1) compared to other per unit terms (P_{m_ref}, $\frac{E\,V}{3\,x_g}$, and D). Hence, the system effectively becomes a linear system with a very fast decaying dynamic either towards stable point (highlighted in green in Fig. 2.4) or unstable point (highlighted in red in Fig. 2.4). This means, the converter will not exercise any inertial dynamics during large-signal transients, which does not allow proper time for other connected VSGs to adjust their operating point, as shown in Fig. 2.4. This would result in oscillation in grid power and frequency, especially in the case of a temporary fault. That is, the converter frequency and power angle trajectory will travel faster towards the unstable region and can cross it before the fault is cleared.

It is worth mentioning that, based on the stability definition revised in [40] that addresses power system stability under high renewable energy penetration, the transient time of inertia action should be between 5 to 10 s. This behavior is consistent with time progression between $t = 1\ s$ and $5\ s$.

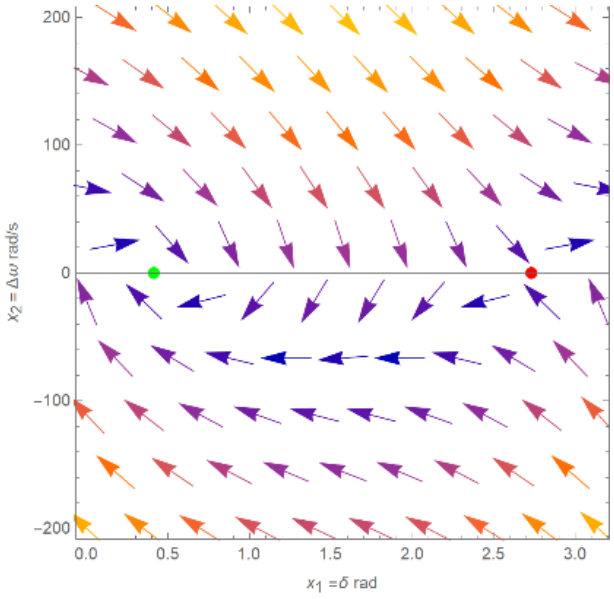

Fig. 2.4. VSG large signal dynamics at $Td = 0.001s$ at $t = 0.01s$

Fig. 2.5. shows the change in the VSG frequency $\Delta\omega$ and power angle δ with respect to each other and more importantly with respect to the time t. The system inertial effect only lasts less than 0.01s before the droop control term in equation (2.36) becomes too dominant and overrides the inertia controller.

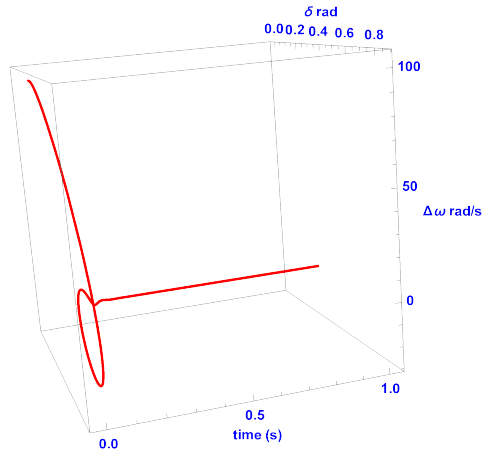

Fig. 2.5. Parametric 3D plot of VSG frequency $\Delta\omega$ and power angle δ as function of time t for high bandwidth LPF

Medium bandwidth LPF

In medium bandwidth case, Td is set to 0.1s, the exponential term becomes less dominant after $t = 0.01s$, which allows some inertial transient to show up in VSG dynamics, as shown in Fig. 2.6 (a). However, the decaying time is fast after $t = 1s$, as the droop control dominates the dynamics, as shown in Fig. 2.6 (b). The change in frequency $\Delta\omega$ and power angle δ with respect to each other as a function of time t is shown in Fig. 2.7. VSG inertial action lasts that 0.1s before the droop control term in equation (2.36) becomes too dominant and overrides the inertia controller.

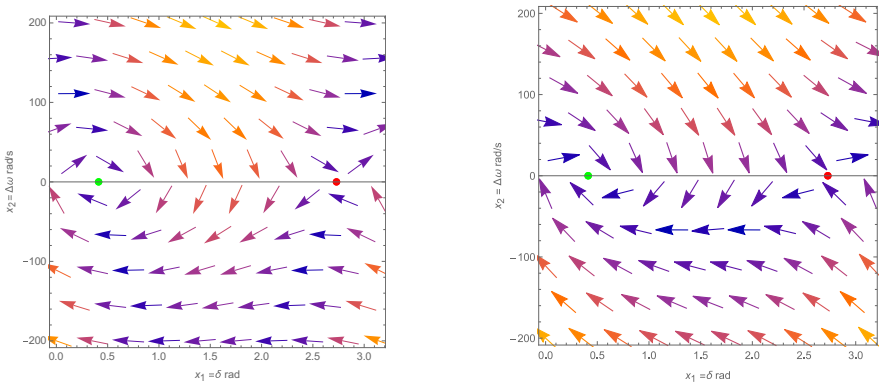

(a) (b)

Fig. 2.6. VSG large signal dynamics at $Td = 0.1s$ at (a) $t = 0.01s$; (b) $t = 1s$

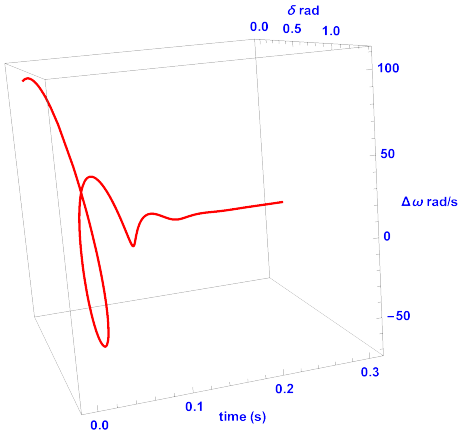

Fig. 2.7. Parametric 3D plot of VSG frequency $\Delta\omega$ and power angle δ as function of time t for medium bandwidth LPF

Low bandwidth LPF

In low bandwidth case, Td is set to 5s, the VSG now experiences full inertia dynamics like synchronous generators, as shown in Fig. 2.8 (a) at $t = 0.01s$. In Fig. 2.8 (b), after 5s, converter slowly regulates its frequency and power angle based on its droop control unit as planned and in comply with [40]. This is shown clearly in Fig. 2.9, where the inertia controller dominated the system dynamics after high disturbance before the droop control takes over and slowly regulates system towards its stable operation.

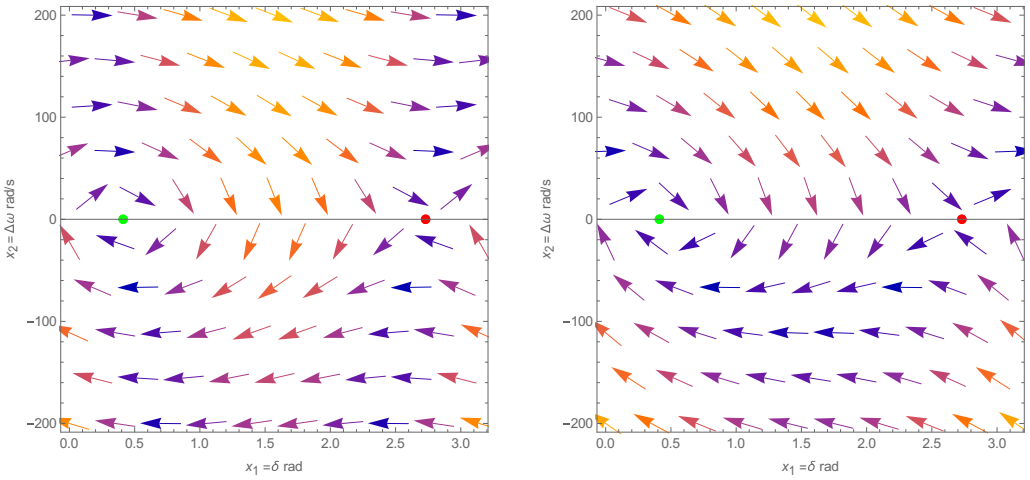

(a) (b)

Fig. 2.8. VSG large signal dynamics at $Td = 5s$ at (a) $t = 0.01s$; (b) $t = 5s$

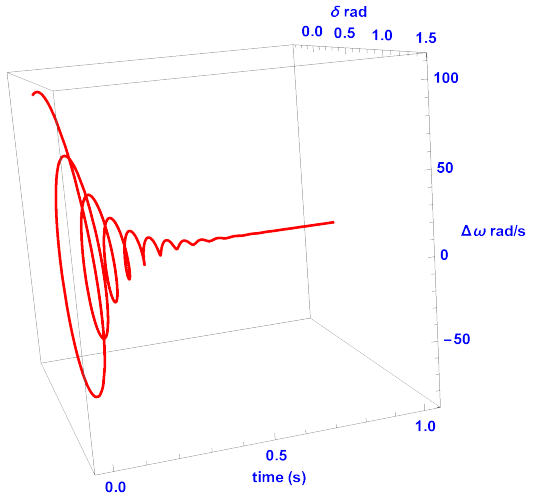

Fig. 2.9. Parametric 3D plot of VSG frequency $\Delta\omega$ and power angle δ as function of time t for low bandwidth LPF

The low-pass filter provides a proper delay that keeps the virtual mechanical input power constant during virtual inertial action. Then it slowly adjusts VSG operating point to regulate grid frequency and power. This emulates the delay provided by the mechanical transient of the prime movers of synchronous generators. This is particularly important to keep the grid stable during and after temporary faults in power electronic dominated power systems. Whether such an inertial action, that is accompanied with large long oscillations, is beneficial to the microgrid or not is still an open topic [14]. However, damping of grid frequency oscillation should be done using proper tuning of inertia controller parameters namely inertia M and damping D, rather than forcing it by the droop control unit.

2. 1. 4. Simulation Results

The performance of a VSG using different LPFs is simulated using a Matlab / Simulink model. A VSG is connected to a single ac bus by a short ac transmission line x_{T1} where the load LD_1 is connected. VSG output filter x_f is considered to be part of the transmission line inductance to keep high inductive transmission line x_g. The simulation parameters are listed in Table I and its block diagram is shown in Fig. 2.1.

First, VSG with high bandwidth LPF in the governor model is simulated. The bandwidth of the LPF is set to 1 kHz which supplies a delay of $Td = 1\ ms$. The power reference P_{m_ref} is stepped from 0 to 0.4 p.u. to be large amplitude disturbances at $t = 0s$. Then, small signal disturbance is applied at $t = 2s$ by stepping the P_{m_ref} again from 0.4 to 0.45 p.u., as shown in Fig. 2.10 (a). Under large disturbances, Fig. 2.10 (b) shows sharp transient in VSG frequency towards its steady-state value. This confirms the analysis provided in this study that the droop control unit in the governor model becomes dominant and overtakes the dynamics. Meaning, the VSG didn't experience any inertia reaction and it can be considered as pure droop control unit. Similar behavior is shown during VSG response to small disturbances, as shown in Fig. 2.10 (c). Furthermore, converter frequency-angle trajectory shows how it moves directly towards steady-state point (approaches the stable equilibrium point) very quickly without proper inertial reaction normally dictated by swing equation in (2.33), as shown in Fig. 2.10 (d).

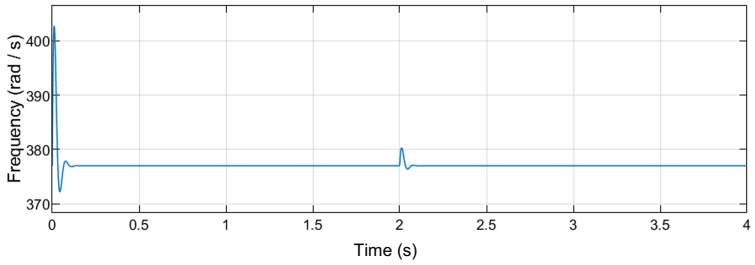

(a)

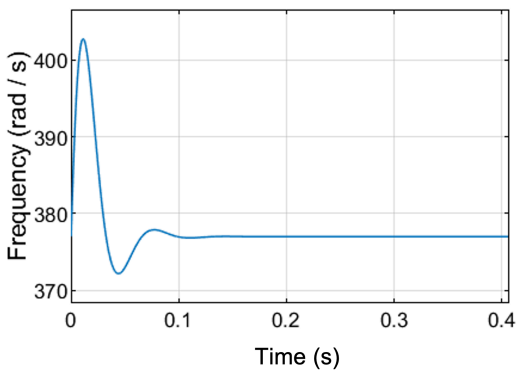

(b)

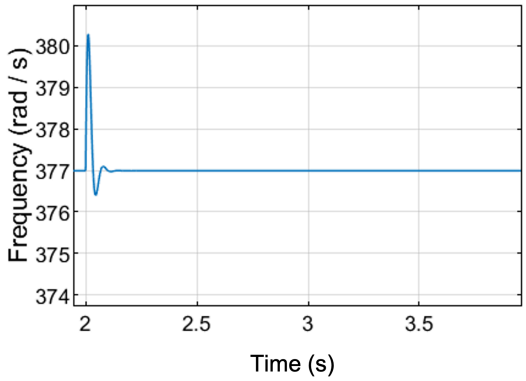

(c)

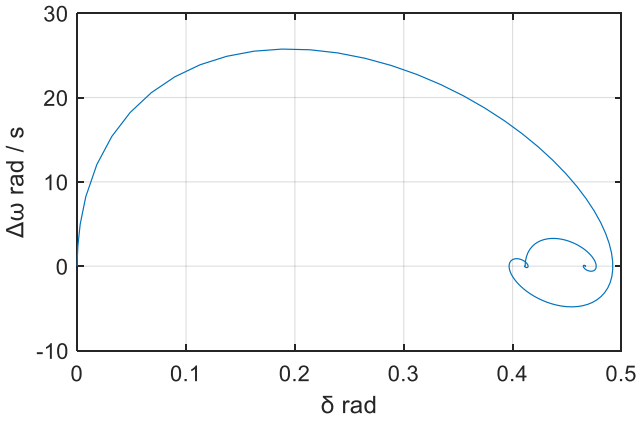

(d)

Fig. 2.10. High bandwidth LPF case (Td=1 ms) (a) VSG frequency in rad /s; (b) zoomed view at VSG response to large disturbance at $t = 0s$; (c) zoomed view at VSG response to small disturbance at $t = 2s$; (d) VSG frequency-angle trajectory during both step responses.

Although in some cases it seems that such a response is desirable as the VSG exhibits well damped transient, regardless of the amplitude of the applied disturbance. The issue becomes clearer by seeing converters reference power P_{m_ref} and its output power P_o. Ideally, for stable operation, the reference signal that is generated by the outer control loop

must remain constant to allow the inner control loop to follow it. However, the power transient of VSG using LPF with high bandwidth, shown in Fig. 2.11 (a), doesn't agree with this fundamental rule.

Instead, Fig. 2.11 (b) and (c) show that the converter's virtual mechanical reference varies simultaneously with the actual electrical output power. Meaning that the reference power does not remain constant for long enough time for the inertia controller to perform its action and follow it. This can easily lead to unstable operation despite the apparent damping. It is worth mentioning that better damping of grid frequency should be pursued by adjusting and tuning the inertia control loop parameters, either online or offline, but not with allowing unstable control loops.

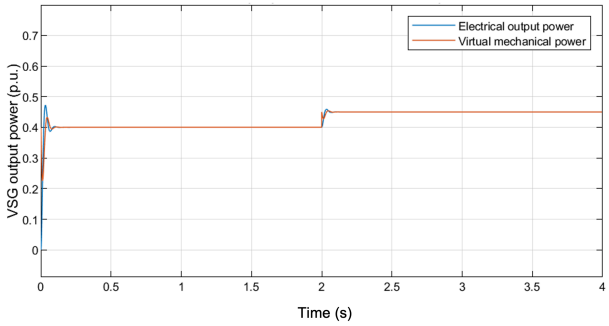

(a)

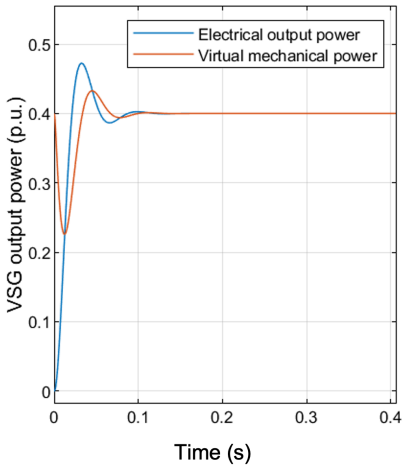

(b)

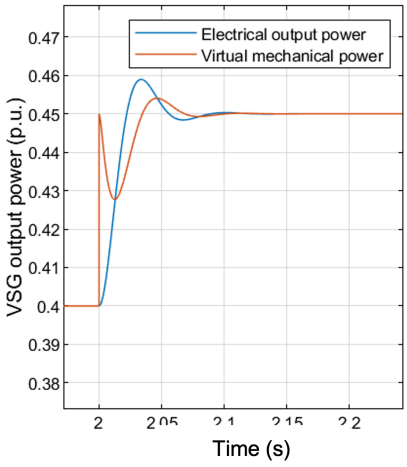

(c)

Fig. 2.11. High bandwidth LPF case (Td=1 ms) (a) VSG output power in p.u.; (b) zoomed view at VSG response to large disturbance P_{m_ref} from 0 to 0.4 p.u. at $t = 0s$; (c) zoomed view at VSG response to small disturbance P_{m_ref} from 0.4 to 0.45 p.u. at $t = 2s$;

In the second case, the same VSG is simulated using the same parameters in Table 2.1 but with medium bandwidth LPF in the governor model instead. The bandwidth of the LPF is set to 100 Hz which supplies a delay of $Td = 10\ ms$. Identical step changes to the first case are applied to the VSG. The power reference P_{m_ref} is stepped from 0 to 0.4 p.u. to apply a large amplitude disturbance at $t = 0s$. This is followed by a small signal disturbance applied at $t = 2s$ by stepping the P_{m_ref} again from 0.4 to 0.45 p.u., as shown in Fig. 2.12 (a). Under large disturbances, Fig. 2.12 (b) shows better transients in VSG frequency compared with the first case where the delay introduced by the LPF in this case allows the inertia control loop (inner loop) to adjust VSG frequency and power angle and follow its reference power P_{m_ref}. In this case, the VSG experiences better inertial reaction. However, since the delay provided by the LPF in this case wasn't long enough, this causes the droop control loop to interfere with the transient. Similar behavior is shown during VSG response to small disturbances as shown in Fig. 2.12 (c). Moreover, the frequency-angle trajectory, shown in Fig. 2.12 (d), shows how the VSG has better dynamics compared with the first case (high bandwidth LPF).

The transient of the VSG output power due to the applied step change in its reference power is shown in Fig. 2.13 (a). Fig. 2.13 (b) and (c) show that, although the converter's virtual mechanical reference varies simultaneously with the actual electrical output power, it varies with much smaller amplitude as compared with the first case. Meaning that the reference power has less impact on the converter inertial reaction and its control loop stability.

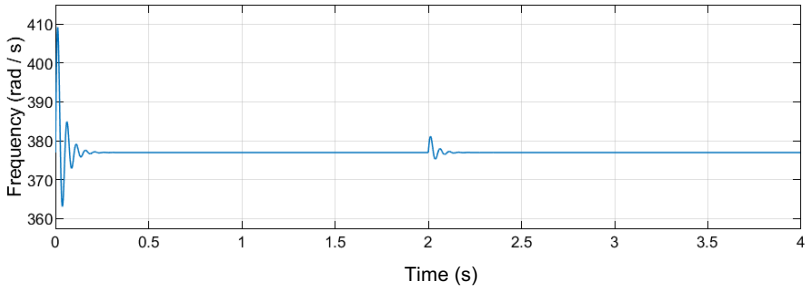

(a)

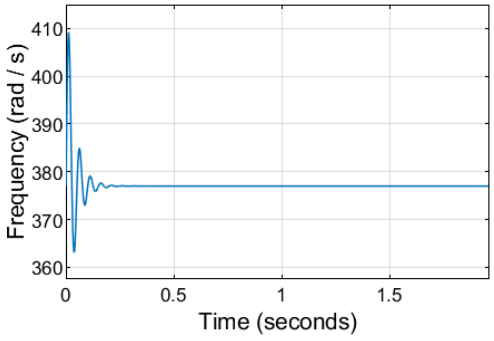

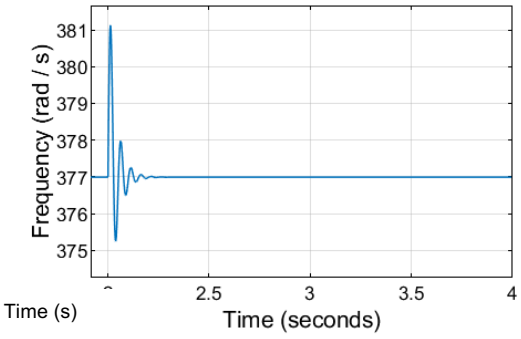

(b) (c)

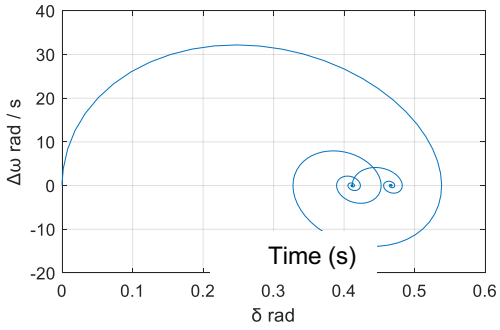

(d)

Fig. 2.12. Medium bandwidth LPF case (Td=10 ms) (a) VSG frequency in rad /s; (b) zoomed view at VSG response to large disturbance at $t = 0s$; (c) zoomed view at VSG response to small disturbance at $t = 2s$; (d) VSG frequency-angle trajectory during both step responses.

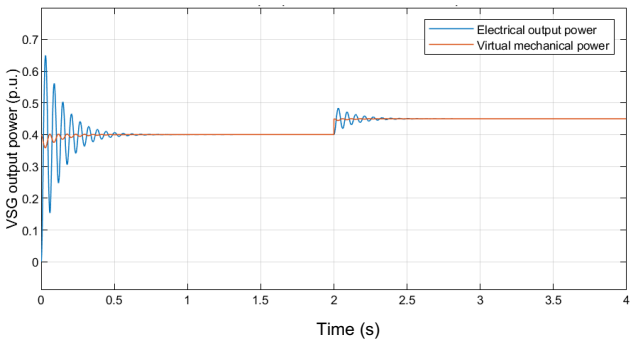

(a)

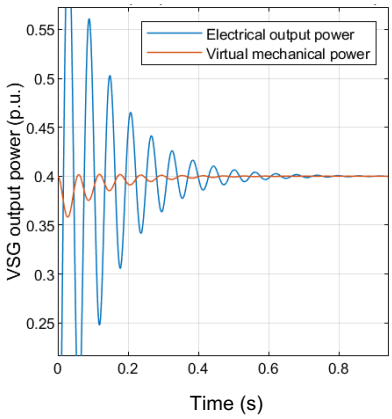

(b)

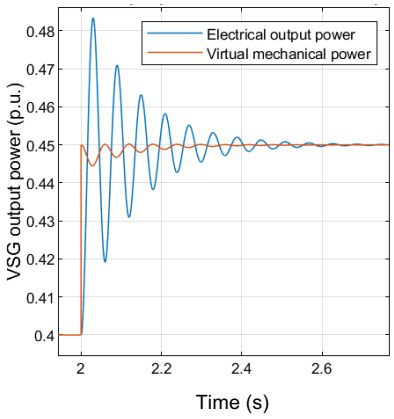

(c)

Fig. 2.13. Medium bandwidth LPF case (Td=10 ms) (a) VSG output power in p.u.; (b) zoomed view at VSG response to large disturbance P_{m_ref} from 0 to 0.4 p.u. at $t = 0s$; (c) zoomed view at VSG response to small disturbance P_{m_ref} from 0.4 to 0.45 p.u. at $t = 2s$;

Finally, in the third case, the VSG is simulated using low bandwidth LPF in the governor model. The bandwidth of the LPF is set to 1 Hz which supplies a delay of $Td = 1\ s$. Identical step changes to the first and second cases are applied to the VSG. The power reference P_{m_ref} is stepped from 0 to 0.4 p.u. at $t = 0s$, and at $t = 2s$ by stepping the P_{m_ref} again from 0.4 to 0.45 p.u., as shown in Fig. 2.14 (a).

During both step changes, better transients are seen in VSG frequency as they are in complete agreement with the swing equation in (2.33) and the dynamical behavior shown in converter's vector field in Fig. 2.8 (a). Where, the delay introduced by the LPF in this case, allows the inertia control loop (inner loop) to adjust VSG frequency and power angle and

follow its reference power P_{m_ref}, as shown in Fig. 2.14 (b) and (c). In this case, the VSG reference power remains constant during the transient which enables stable operation in both control loops (namely droop control loop and inertia control loop). Moreover, the frequency-angle trajectory, shown in Fig. 2.14 (d), shows how the VSG has full inertial dynamics compared with the first case (high and medium bandwidth LPF). The converter has high oscillatory transient which isn't ideal. However, as mentioned, reducing the oscillation should not be at the expense of an unstable inner control loop. Furthermore, the only difference in all simulated cases is the bandwidth of the low-pass filter itself. The parameters of the VSG always remain constant as well as the testing conditions. This proves the study conclusion, that the LPF in VSG control loop has a significant impact on the converter's dynamics if it is not properly selected.

Finally, the transient of the VSG output power due to the applied step change in its reference power is shown in Fig. 2.15 (a). Fig. 2.15 (b) and (c) show that the proper LPF keeps the converter's virtual mechanical reference constant during the transient which gives time to the inertia control loop to adjust converter's frequency and angle to match its reference. The droop control unit later regulates the frequency and power sharing within the MG. This complies with the definition of power system stability criterion provided in [40].

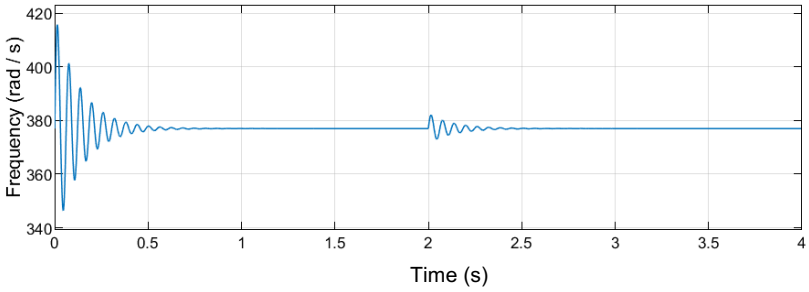

(a)

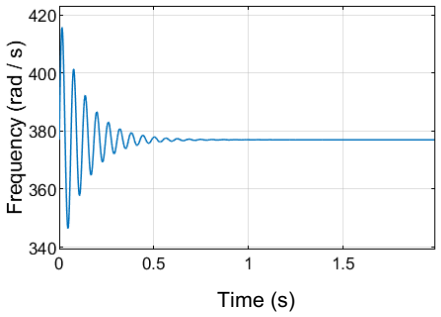

(b)

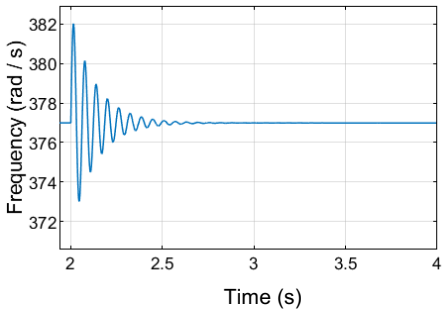

(c)

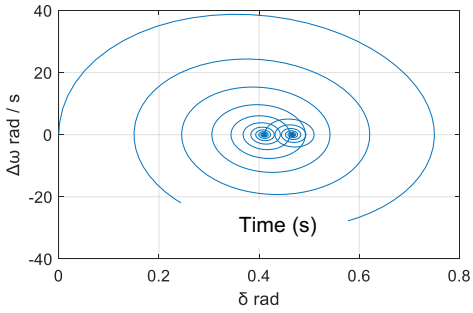

(d)

Fig. 2.14. Low bandwidth LPF case (Td=1s) (a) VSG frequency in rad /s; (b) zoomed view at VSG response to large disturbance at $t = 0s$; (c) zoomed view at VSG response to small disturbance at $t = 2s$; (d) VSG frequency-angle trajectory during both step responses.

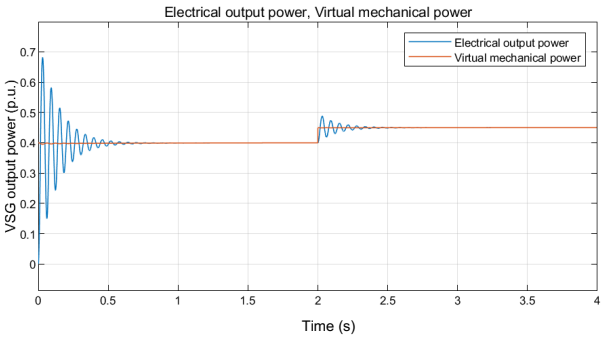

(a)

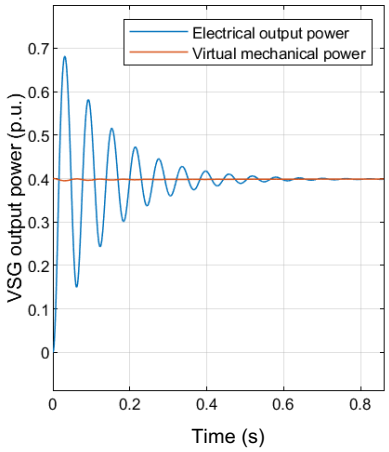

(b)

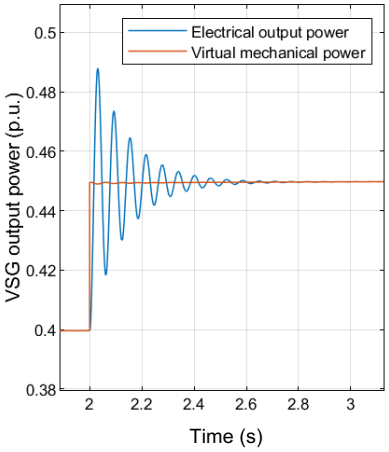

(c)

Fig. 2.15. Medium bandwidth LPF case (Td=1s) (a) VSG output power in p.u.; (b) zoomed view at VSG response to large disturbance P_{m_ref} from 0 to 0.4 p.u. at $t = 0s$; (c) zoomed view at VSG response to small disturbance P_{m_ref} from 0.4 to 0.45 p.u. at $t = 2s$;

2. 2. Small-signal model

A small-signal model can be directly evaluated from the large-signal model by taking its Jacobian at an equilibrium point. This can be effectively done by linearizing the system within the vicinity of the operating point (i.e., $SEP + \varepsilon$). At this point, only linear terms are considered as they become more dominant closer to the equilibrium point. Such an approach might result in rather complex mathematical manipulations in a multi-VSG MG [50].

Therefore, first the small-signal model is derived based on the small perturbation concept around the operating point of one generator (VSG). The model is then extended for a multi generator system in the MG. This is based on the work introduced in [35], [46]. It is important to note that the aim of developing this model is to study the stability of the MG which is largely dominated by power converters with added virtual inertia. Thus, a detailed dynamic description of the synchronous machines is not necessary. Only the dynamics and characteristics related to the generated output power fall within the scope of this work and offer the proper approximation in the model.

2. 2. 1. Small-signal model of single VSG converter

As mentioned earlier, the swing equation of a synchronous generator defines the relation between the mismatch between the input mechanical power and output electrical power, and the change in output frequency weighted by the inertia and damping constants. Fig. 2.16 shows a single VSG converter connected to a one load bus. Its model can be expressed as follows:

$$P_{in}(t) - P_{out}(t) = M\,\omega\frac{d\omega}{dt} + D(\omega - \omega_b) \tag{2.37}$$

Where,

$P_{in}(t)$ is the input mechanical power,

$P_{out}(t)$ is the output electrical active power,

M is the inertia coefficient,

D is the damping coefficient,

ω is the generator frequency,

ω_b is the load bus frequency at load side.

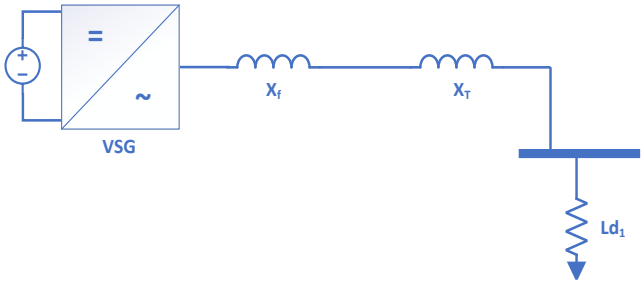

Fig. 2.16. Single VSG converter connected to single load bus.

In [26], both inertia and damping coefficients are defined as follows:

$$D = D' \frac{P_{base}}{\omega_o} \tag{2.38}$$

Where,

D' is damping constant,

P_{base} is power rating of the generator,

ω_o is the nominal frequency.

$$M = 2\,H \frac{S_o}{\omega_o^2} \tag{2.39}$$

Where,

S_o is the nominal apparent output power at nominal frequency,

H is the time during which the generator can supply nominal load using solely its kinetic energy. Typically, it ranges between 2s to 10s [44].

Virtual mechanical input power can also be expressed in terms of generator base power P_{base}, nominal power P_o and droop coefficient K_p using $\omega - P$ droop control relationship as follows [24], [51]:

$$P_{in} = P_o - K_p P_{base} \frac{\omega - \omega_0}{\omega_o} \tag{2.40}$$

As P_{base}, K_p and ω_o are all constants, they can be combined into the droop constant as follows:

$$P_{in} = P_o - K_p \, (\omega - \omega_0)$$

Hence, by substituting equation (2.36) in equation (2.33), the swing equation becomes:

$$P_o - K_p \, (\omega - \omega_0) - P_{out}(t) = M \, \omega \frac{d\omega}{dt} + D(\omega - \omega_b) \tag{2.41}$$

Assuming a small perturbation (Δ) that will affect each variable causing it to move within the vicinity of the original operating point, the resultant small-signal model can be evaluated as follows:

$$-K_p \, \Delta\omega - \Delta P_{out} = M \, (\omega \, S\Delta\omega + S\Delta\omega^2) + D(\Delta\omega - \Delta\omega_b) \tag{2.42}$$

Where, $\Delta\omega$ is the deviation from the nominal frequency ω_o.

If the second order perturbation term $\Delta\omega^2$ is neglected, and for a small frequency deviation $\omega \approx \omega_o$, then,

$$-K_p \, \Delta\omega - \Delta P_{out} = M \, \omega_o \, S\Delta\omega + D(\Delta\omega - \Delta\omega_b) \tag{2.43}$$

To have an explicit transfer function between $\Delta\omega/\Delta P$, anther equation is needed to eliminate $(\Delta\omega - \Delta\omega_b)$.

For the system shown in Fig. 2.16, the change in generator output power can also be expressed as follows:

$$\Delta P_{out} = \frac{E_b \, E \cos\delta}{X_{line}} \, \Delta\delta \tag{2.44}$$

This is valid for small values of $\Delta\delta$, highly inductive transmission lines, small change in the output / load power, and load bus the reference voltage $E_b \angle 0°$.

For simplification, K_s is appointed as the synchronization coefficient and is equal to:

$$K_s = \frac{E_b E \cos\delta}{X_{line}} \tag{2.45}$$

Moreover, $\Delta\delta$ can be expresses as $(\Delta\omega - \Delta\omega_b)/s$, which leads to:

$$\Delta P_{out} = K_s \frac{\Delta\omega - \Delta\omega_b}{s}$$

By applying Laplace differential operator S,

$$\mathrm{S}\,\Delta P_{out} = K_s\,(\Delta\omega - \Delta\omega_b) \tag{2.46}$$

Finally, by substituting equation (2.42) into equation (2.37):

$$-K_p\,\Delta\omega - \Delta P_{out} = M\,\omega_o\,S\Delta\omega + D\,\frac{S\Delta P_{out}}{K_s} \tag{2.47}$$

The transfer function is obtained:

$$\frac{\Delta\omega}{\Delta P_{out}} = -\frac{1 + \left(\frac{D}{K_s}\right)\,S}{K_p + M\omega_0\,S} \tag{2.48}$$

Equation (2.48) then describes the frequency change corresponding to a small load change in a system consisting of a single generator connected to a single load bus. Despite the simplicity of the topology itself, it can be extended to a system of n generators.

Moreover, it facilitates the study of power converters under virtual inertia control and conventional droop control as well. By setting both inertia and damping coefficients to zero, equation (2.48) turns into droop control transfer function $\left(-\frac{1}{k_P}\right)$. Furthermore, it enables the study of MG stability (subject of this work) in terms of the other parameters such as line impedance, amount of virtual damping in VSG, effect of virtual governor model (virtual prime mover). Although equation (2.48) is a compact form, it contains all needed performance parameters.

A step response is then applied to MG's small-signal model, where a small change in the connected loads is created by increasing the load by 1.8%. The system performance is evaluated under different parameters. The corresponding change in the output frequency $\Delta\omega$ with respect to time is depicted in Fig. 2.17. under different inertia coefficients by

reducing the inertia coefficient M from its selected nominal value $M_o = 2$ (from 1.0 to 0.75, to 0.5 then 0.25) while keeping all other parameters constant. The rate of changing of $\Delta\omega$ becomes higher (faster) which is expected and consistent. Furthermore, the steady-state value of $\Delta\omega$ is decided by the droop coefficient $K_p$which aligned with the expectations from a droop-controlled unit (equation (2.40)).

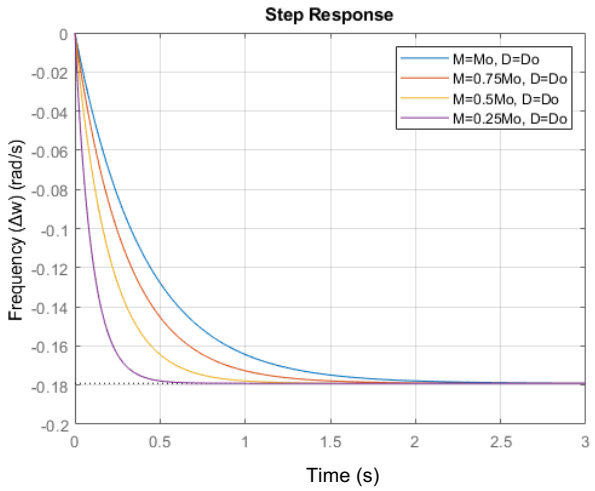

Fig. 2.17. Change in the output frequency $\Delta\omega$ after 1.8% load step change at different inertias.

On the other hand, changing the damping coefficient D does not have any effect on the $\Delta\omega$ as shown in Fig. 2.18. (a) and Fig. 2.18. (b), where the damping coefficient D is reduced from its selected nominal value D_o (from 1.0 to 0.75 to 0.5 then 0.25) while keeping all other parameters constant. However, it has been reported in [7], [46], [51] that the damping coefficient D might cause power oscillations and affects active power sharing. Hence, it will not be neglected throughout this study.

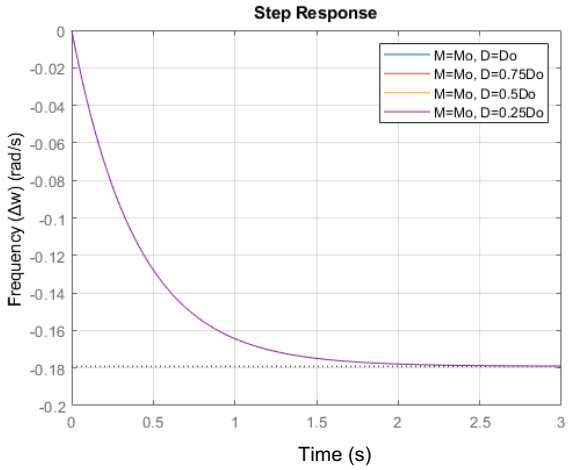

(a)

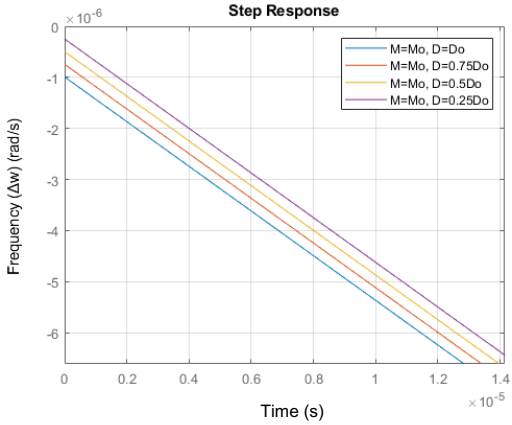

(b)

Fig. 2.18. (a) Change in the output frequency $\Delta\omega$ after 1.8% load step change at different damping ratio; (b) zoomed version to show identify the overlapped signals.

Finally, system step response under different values of M and D is compared against conventional droop-controlled case; the results are depicted in Fig. 2.19. Based on the above discussion, reducing the amount of inertia M results in reducing the rate of change of $\Delta\omega$, while the damping coefficient D has a minimal effect so far. However, by comparison, in the droop-controlled case, where the frequency of the system has an almost instantaneous frequency transient, this is particularly an undesirable behaviour from a

power system point of view, where a slower rate of change in frequency allows other connected generators to detect the occurrence of a load transient (by detecting the change in the frequency) and adjusting their powers accordingly.

A noteworthy remark here is that the small delay in the droop-controlled case is caused by inserting a delay (low-pass filter) to the droop-control unit. This is a common practice in power system control [1] to provide a means to increase system stability. However, it does not solve the stability issue in low inertial MG as the delay is fixed despite the amount of load transition which results in poor load sharing.

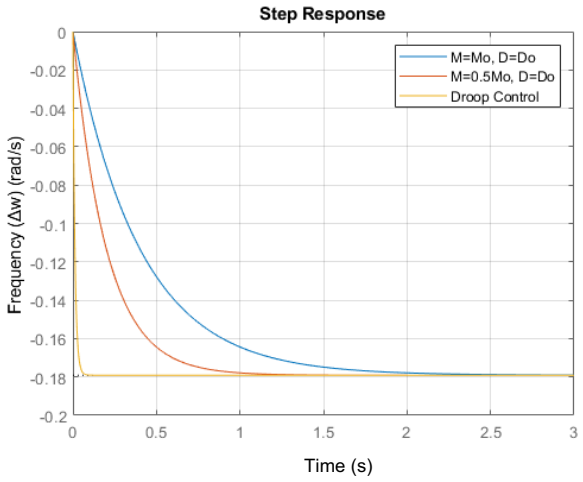

Fig. 2.19. Change in the output frequency $\Delta\omega$ after 1.8% load step change at different inertia (100% and 50%) and compared to droop-controlled case.

2. 2. 2. Small-signal model of multi-VSG

The small-signal model is extended to two machines configuration, as shown in Fig. 2.20 [51].

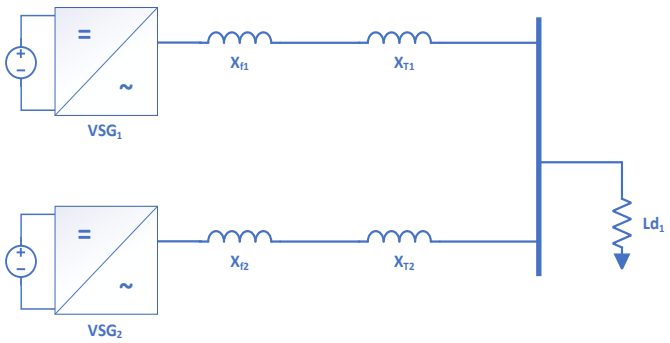

Fig. 2.20. Two VSG converters connected to single-load bus

The load (Ld_1) total power P_{load} is the sum of the powers of the two generators, $P_{out,1}$ and $P_{out,2}$. Therefore, the perturbation of the load power (Δ) can be expressed as follows:

$$\Delta P_{out} = \Delta P_{out,1} + \Delta P_{out,2} \tag{2.49}$$

The variation in the load frequency $\Delta\omega_b$ with respect to the variation in its power ΔP_{out} is:

$$\frac{\Delta P_{load}}{\Delta \omega_b} = \frac{\Delta P_{out,1}}{\Delta \omega_b} + \frac{\Delta P_{out,2}}{\Delta \omega_b} \tag{2.50}$$

Letting,

$$A = \frac{\Delta P_{out,1}}{\Delta \omega_b} \qquad and \qquad B = \frac{\Delta P_{out,2}}{\Delta \omega_b}$$

Then,

$$\frac{\Delta P_{load}}{\Delta \omega_b} = A + B \tag{2.51}$$

Equation (2.46) holds as well for the second generator as follows:

$$S\,\Delta P_{out,2} = K_{s,2}\,(\Delta\omega_2 - \Delta\omega_b) \tag{2.52}$$

Equation (2.50) can also be rewritten in terms of $\Delta P_{out,2}$, A, and B:

$$\Delta P_{load} = \left(1 + \frac{A}{B}\right)\Delta P_{out,2} \tag{2.53}$$

By eliminating $\Delta P_{out,2}$ from equation (2.53) using equation (2.52):

$$\Delta P_{load} = \left(1 + \frac{A}{B}\right)\left(\frac{K_{s,2}}{s}\right)\ (\Delta\omega_2 - \Delta\omega_b) \tag{2.54}$$

However, as the intention is to find a relationship between $\Delta\omega_2$ of second generator and ΔP_{load}. Then, $\Delta\omega_b$ must be eliminated.

Knowing that,

$$\frac{\Delta P_{load}}{\Delta\omega_b} = B + A$$

$$\Delta\omega_b = \frac{\Delta P_{load}}{B + A} \tag{2.55}$$

Hence, equation (2.54) becomes,

$$\Delta P_{load} = \left(1 + \frac{A}{B}\right)\left(\frac{K_{s,2}}{s}\right)\ (\Delta\omega_2 - \frac{\Delta P_{load}}{B + A})$$

$$\Delta P_{load}\left(1 + \left(\frac{K_{s,2}}{B\ s}\right)\right) = \left(1 + \frac{A}{B}\right)\left(\frac{K_{s,2}}{s}\right)\ \Delta\omega_2$$

$$\frac{\Delta\omega_2}{\Delta P_{load}} = \frac{K_{s,2} + Bs}{K_{s,2}(A + B)} \tag{2.56}$$

Equation (2.56) then stands for the transfer function that links the change in the second generator output frequency $\Delta\omega_2$ with respect to the load variation ΔP_{load}. A similar relationship can be found for the first generator; the only difference is the synchronous constant $K_{s,2}$ will now become $K_{s,1}$.

Moreover, the transfer function that relates the change in the generator output power ($P_{out,1}$ or $P_{out,2}$) to the change in the bus frequency $\Delta\omega_b$ can also be derived similar to the single generator case by solving for $\Delta\omega_b$ instead of $\Delta\omega_1$. Consequently,

$$A = \frac{\Delta P_{out,1}}{\Delta\omega_b} = \frac{K_{p,1} + M_1\omega_o s}{1 + \frac{K_{p,1} + D_1}{K_{s,1}} + \frac{M_1\omega_o}{K_{s,1}}\ s^2} \tag{2.57}$$

$$B = \frac{\Delta P_{out,2}}{\Delta \omega_b} = \frac{K_{p,2} + M_2 \omega_o s}{1 + \frac{K_{p,2} + D_2}{K_{s,2}} + \frac{M_2 \omega_o}{K_{s,2}} s^2} \tag{2.58}$$

The step response of the case of two generators is performed under different inertias ($M_2 = M_o$, $M_2 = 0.5M_o$, and $M_2 = 0$) for the second generator (equation (2.56)). This is being done while keeping the droop constant K_p of both generators like the one generator case.

Fig. 2.21 shows that the system acts as a typical over-damped, second-order system and getting closer to the first-order system response as M_2 approaches zero. Furthermore, the trend in the change in the generator frequency $\Delta\omega_2$ with respect to the change in the load power P_{load} is consistent with the single generator case studied earlier. Nonetheless, at $M_2 = 0$ an abrupt change in the output frequency has not occurred as the other generator still contributes to the overall system inertia.

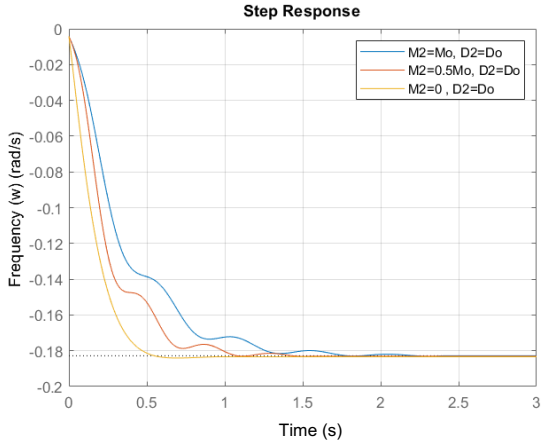

Fig. 2.21. Step response of the case of two generators under different inertias ($M_2 = M_o$, $M_2 = 0.5M_o$, and $M_2 = 0$)

Finally, the small-signal state space model of the system is expressed as follows, based on [46]:

$$\left.\begin{aligned} \dot{x} &= Ax + Bu \\ \dot{y} &= Cx + Du \end{aligned}\right\} \tag{2.59}$$

$$x = \begin{bmatrix} \Delta\omega_2 + \dfrac{D_2}{M_2\omega_o\left(K_{s,2}+K_{s,1}\right)}\Delta P_{load} \\ \Delta\omega_1 + \dfrac{D_1}{M_1\omega_o\left(K_{s,2}+K_{s,1}\right)}\Delta P_{load} \\ \Delta\delta_2 - \dfrac{1}{\left(K_{s,2}+K_{s,1}\right)}\Delta P_{load} \\ \Delta P_{in,2} \\ \Delta P_{in,1} \end{bmatrix}$$

$$u = [\Delta P_{load}]$$

$$y = \begin{bmatrix} \Delta\omega_2 \\ \Delta\omega_1 \\ \Delta P_{out,2} \\ \Delta P_{out,2} \end{bmatrix}$$

$$A = \begin{bmatrix} \dfrac{K_{s,1}D_2}{M_2\omega_o\left(K_{s,2}+K_{s,1}\right)} & \dfrac{K_{s,1}D_2}{M_2\omega_o\left(K_{s,2}+K_{s,1}\right)} & -\dfrac{K_{s,2}}{M_2\omega_o} & \dfrac{1}{M_2\omega_o} & 0 \\ \dfrac{K_{s,2}D_1}{M_1\omega_o\left(K_{s,2}+K_{s,1}\right)} & -\dfrac{K_{s,2}D_1}{M_1\omega_o\left(K_{s,2}+K_{s,1}\right)} & \dfrac{K_{s,2}}{M_1\omega_o} & 0 & \dfrac{1}{M_1\omega_o} \\ \dfrac{K_{s,1}}{\left(K_{s,2}+K_{s,1}\right)} & -\dfrac{K_{s,1}}{\left(K_{s,2}+K_{s,1}\right)} & 0 & 0 & 0 \\ -\dfrac{K_{p,2}}{T_{d,2}} & 0 & 0 & -\dfrac{1}{T_{d,2}} & 0 \\ 0 & -\dfrac{K_{p,1}}{T_{d,1}} & 0 & 0 & -\dfrac{1}{T_{d,1}} \end{bmatrix}$$

$$B = \begin{bmatrix} -\dfrac{K_{s,2}}{M_2\omega_o\left(K_{s,2}+K_{s,1}\right)} - \dfrac{K_{s,1}D_2D_1}{M_1M_2\omega_o^2\left(K_{s,2}+K_{s,1}\right)^2} + \dfrac{K_{s,1}D_2^2}{M_2^2\omega_o^2\left(K_{s,2}+K_{s,1}\right)^2} \\ -\dfrac{1}{M_1\omega_0} + \dfrac{K_{s,2}}{M_1\omega_o\left(K_{s,2}+K_{s,1}\right)} - \dfrac{K_{s,2}D_2D_1}{M_1M_2\omega_o^2\left(K_{s,2}+K_{s,1}\right)^2} + \dfrac{K_{s,2}D_1^2}{M_1^2\omega_o^2\left(K_{s,2}+K_{s,1}\right)^2} \\ -\dfrac{K_{s,1}D_2}{M_2\omega_o\left(K_{s,2}+K_{s,1}\right)^2} + \dfrac{K_{s,1}D_1}{M_1\omega_o\left(K_{s,2}+K_{s,1}\right)^2} \\ \dfrac{1}{T_{d,2}}\dfrac{K_{p,2}D_2}{M_2\omega_o\left(K_{s,2}+K_{s,1}\right)} \\ \dfrac{1}{T_{d,1}}\dfrac{K_{p,1}D_1}{M_1\omega_o\left(K_{s,2}+K_{s,1}\right)} \end{bmatrix}$$

$$D = \begin{bmatrix} \dfrac{D_2}{M_2\omega_o\left(K_{s,2}+K_{s,1}\right)} \\ \dfrac{D_1}{M_1\omega_o\left(K_{s,2}+K_{s,1}\right)} \\ \dfrac{K_{s,2}}{\left(K_{s,2}+K_{s,1}\right)} \\ \dfrac{K_{s,1}}{\left(K_{s,2}+K_{s,1}\right)} \end{bmatrix}$$

$$C = \begin{bmatrix} 1 & 0 & 0 & 0 & 0 \\ 0 & 1 & 0 & 0 & 0 \\ 0 & 0 & K_{s,2} & 0 & 0 \\ 0 & 0 & -K_{s,2} & 0 & 0 \end{bmatrix}$$

2. 3. Control architecture of virtual synchronous generators (VSGs)

Regulation in a power system relies on the multi-level control architecture to regulate its voltage, frequency, generated power, load sharing, perfect resources utilization, protection, and general asset management. Management and coordination between the generation units is done within the upper (supervisory or master) control layer with the help of communication links for data exchange. The power regulation and protection, on the other hand, are localized and done in the first (local) control layer. Although, advanced communication mediums can be used within this layer, it is not preferable from a reliability point of view. Therefore, such core functions are performed in an autonomous manner, while accepting further enhancements offered by communications and data exchange.

Droop control is widely adopted in power systems as it offers a simple yet reliable regulation technique [52]. Fundamentally, droop control linearly links the variation in the frequency to the power change needed to restore it to its nominal value. The coefficient (slope) of this linear function is known as droop constant *k* and is shown in Fig. 2.22. It is designed based on the generator nominal power, and hence, it enables proportional load sharing among the grid forming generators.

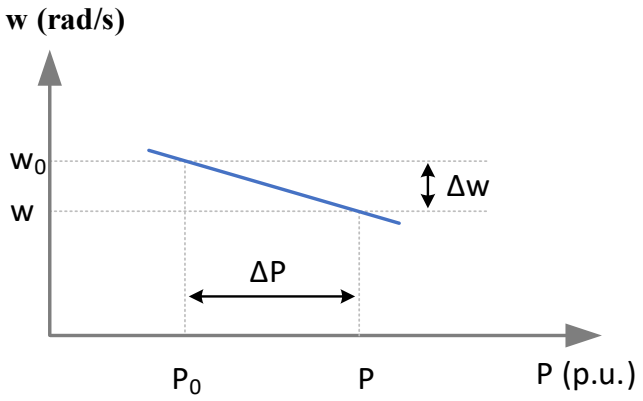

Fig. 2.22. Droop control relation for $\omega - P$ islanding regulation

However, in power electronics dominated MG, the converters' frequency is fixed despite their output power or grid transient. A solution was to insert a droop control block within the converter's control loops as shown in Fig. 2.23. It changes the modulating signal frequency ω_m in proportion to the load power. Typical block diagram of such $\omega - P$ droop control is shown in Fig. 2.24. Nonetheless, the frequency rate of change is fixed (despite the amount of the load transient) and depends only on the time delay of the droop control (which is present because of its filter time delay T_d). This would significantly affect the grid stability, or at best, result in very poor load sharing in the presence of large disturbances.

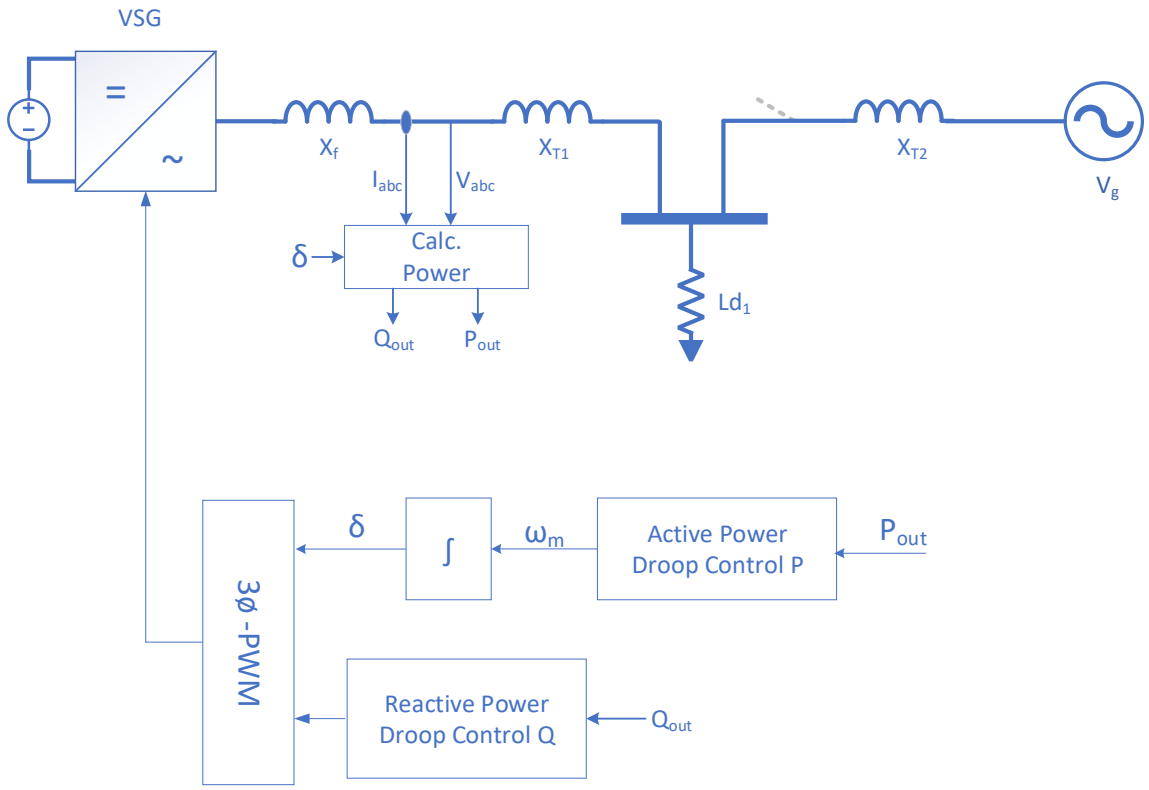

Fig. 2.23. Control loops of droop-controlled grid connected dc-ac power converter

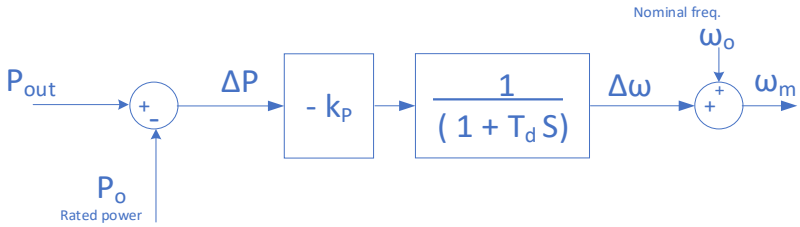

Fig. 2.24. Block diagram of $\omega - P$ droop control in grid connecting

To provide better steady-state and transient responses, emulation of swing equation of synchronous machine is implemented within a converter's control loop. That is, the frequency of the converter's modulating signal is varied based on the mismatch between the electrical output power and a virtual input mechanical power, as explained in section 2.1. Thus, the rate of change in a converter's frequency and its output power is largely dependent on the virtual inertia constant (M), where the steady-state depends on the

reciprocal of the droop constant ($-\frac{1}{k_P}$). The block diagram of the control loop with virtual inertia is shown in Fig. 2.25, and for the sake of completion, the swing equation (equation (2.37)) is stated as follows in p.u.:

$$P_{in}(t) - P_{out}(t) = M\frac{d\omega}{dt} + D(\omega - \omega_b) \tag{2.60}$$

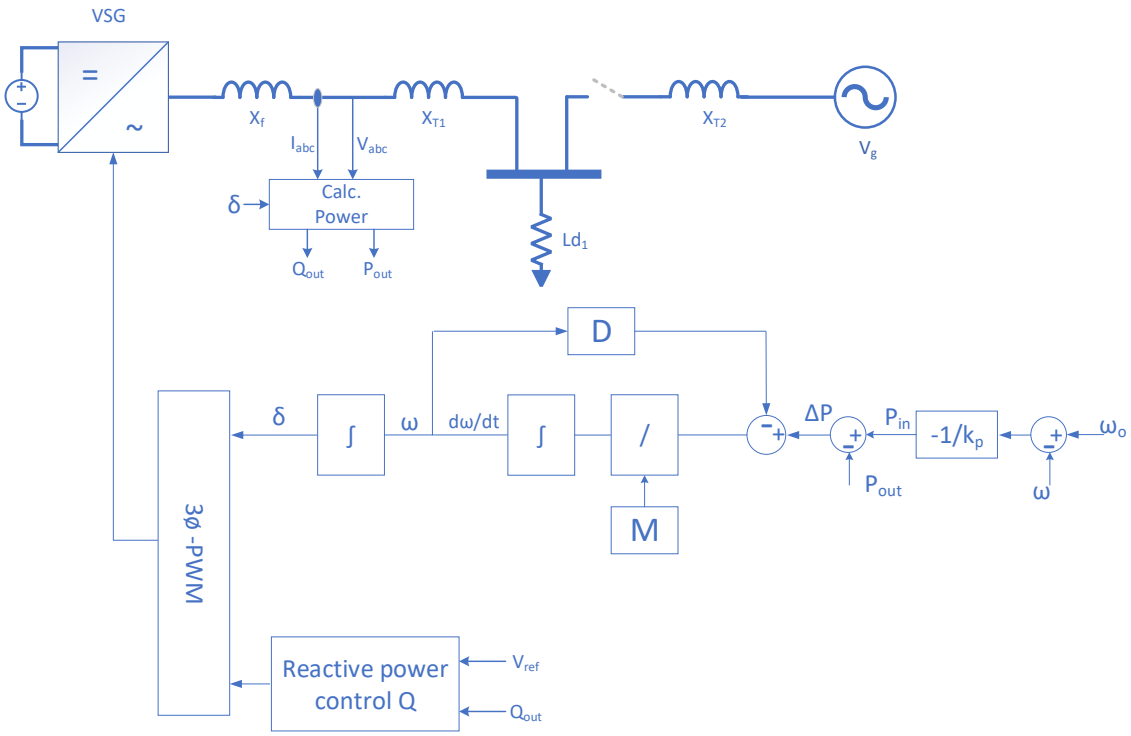

Fig. 2.25. The block diagram of the control loop with virtual inertia in islanding mode.

It is clear that equation (2.60) is a nonlinear differential equation which does not have a closed-form solution [45], [50] to find ω. Solving such equations can be done by applying numerical methods. A family of solvers, based on the Runge-Kutta algorithm, offers a direct one-step method to obtain the solution by implementing a fixed number of sub-steps spaced by properly selected (Δt) [53]. The chart to calculate the proper frequency is shown in Fig. 3.5. Such a flow chart provides a simplified way to experimentally implement virtual inertia using current digital controllers. However, in simulation (which generally uses Runge-Kutta based solvers) a more convenient way is to implement a virtual inertia based on the block diagram shown in Fig. 2.26.

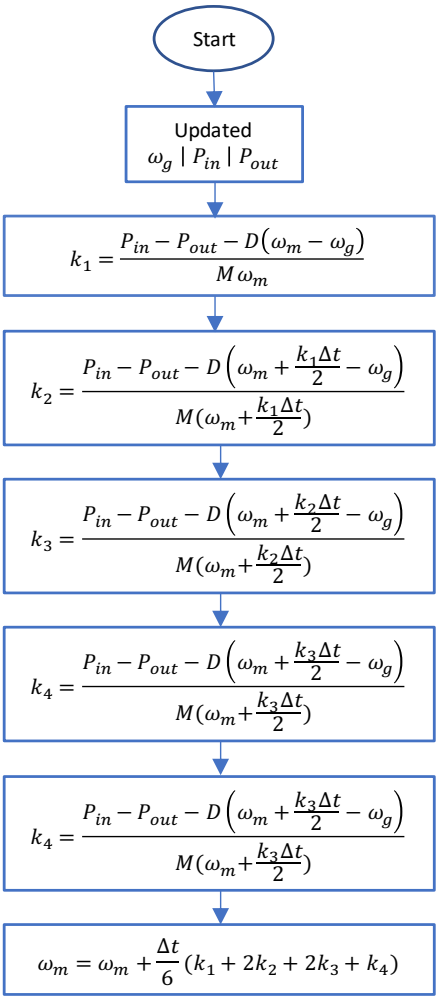

Fig. 2.26. Runge-Kutta flow chart to solve SG swing equation for ω [51]

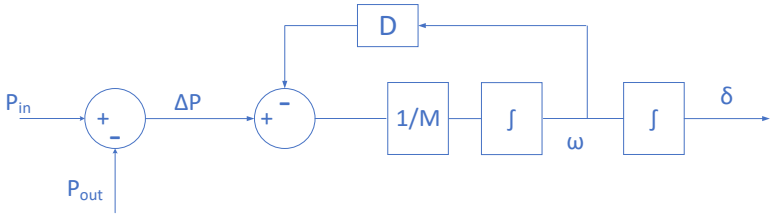

Fig. 2.27. Block diagram of virtual inertia controller

The calculated frequency is, then, fed back to the $\omega - P$ droop control (in islanding mode) which computes the corresponding adjustment to the virtual mechanical input power P_{in} (using droop control). Because of the dependency of the change in the power on the small change in the frequency, a low-pass filter is used with time constant (T_d) to reduce noise effects. The control block diagram of the governor model is shown in Fig. 2.28. (a).

Finally, the grid voltage is typically regulated to (E_o) by ($v - Q$) droop control, as shown in Fig. 2.28. (b).

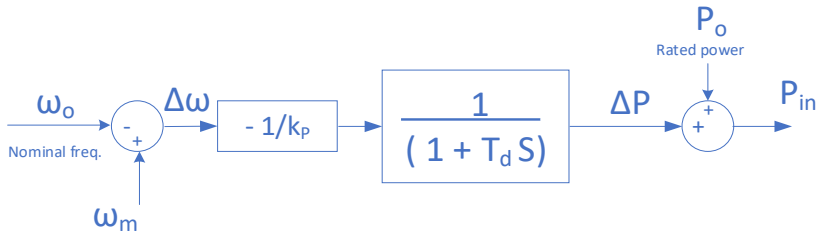

(a)

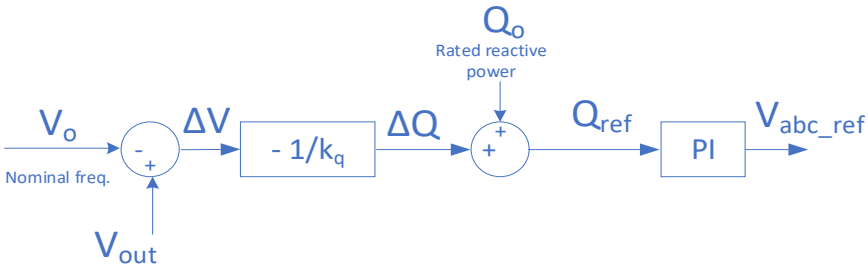

(b)

Fig. 2.28. Active and reactive power control loops in islanding mode (a) $\omega - P$ droop control; (b) $V - Q$ reactive power control loop.

2. 4. Simulation results

The performance of the afore mentioned control loops is validated using a Matlab / Simulink model. A VSG is connected to a single ac bus by a short ac transmission line X_{T1} where the load LD_1 is connected. VSG output filter X_f is part of the transmission line inductance to keep high inductance transmission line assumption valid. Simulation parameters are listed in Table 2.2 and its block diagram is shown in Fig. 2.29. Fig. 2.30 shows change in VSG's virtual input power P_{in} with respect to its electrical output power P_{out} at different levels of load disturbances ΔP. Fig. 2.31 depicts the variation in load bus frequency ω_b with respect to VSG virtual mechanical power frequency ω_m.

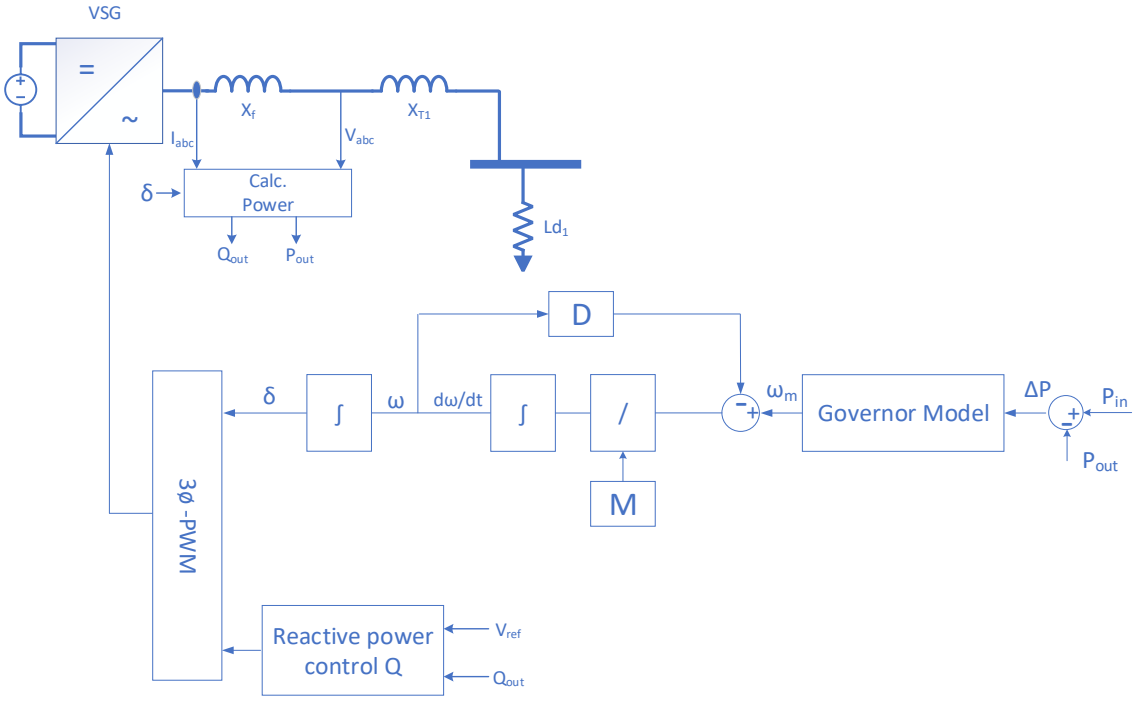

Fig. 2.29. Block diagram of simulated control loop with virtual inertia in islanding mode.

Table 2.2. VSG parameters

Parameter	Value
Virtual input power P_m	4.3 kW
Power electrical power P_e	5.1 kW
VSG output filter X_f	2.5 mH
Line impedance X_{T1}	250 uH
Load bus voltage v_b	110 V
Active power droop coefficient k_p	0.03
Reactive power droop coefficient k_q	0.03
Damping constant D	17 p. u.
Inertial Constant M normalized	2 s

When the VSG starts from rest, mechanical input power P_{in} slowly increases from its initial setpoint $P_{in} = 4.3\ kW$ till it matches its electrical output power $P_{out} = 5.1\ kW$ at $t = 1s$. This slow damped behavior is due to the virtual delay implemented in the governor model (shown in Fig. 2.24). In a SG machine, such a delay comes from the time constant of mechanical system itself. The corresponding frequency deviation (shown in Fig. 2.21) is slowing down because of the increased output power with respect to initial mechanical input power. The damped transient behavior and delay is caused by a virtual inertia controller, as explained earlier, and is mainly dependent on inertia constant M. The steady-state value of bus frequency $\Delta\omega_b$ is determined by the droop control coefficient $-1/k_p$ and, in the absence of frequency regulation block or infinite bus (grid), load bus frequency does not come back to its setpoint. This is acceptable here as the aim is to verify the virtual inertia controller design and observe its transient behavior. A final remark, the delay introduced in the governor model is very important from a system stability analysis point of view as mentioned earlier; that is, mechanical input power is assumed to be constant during any load disturbances or fault conditions. Hence, prime mover delay is introduced in the model.

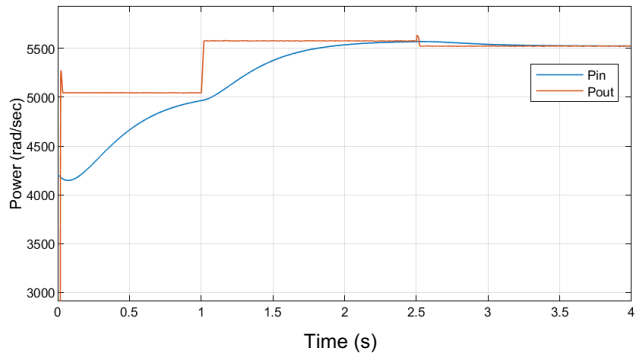

Fig. 2.30. VSG input mechanical power with respect to input mechanical power

Finally, two load step changes are applied to further examine the controller dynamics. First one is applied at $t = 1s$ for $\Delta P = 600\ W$ and second one is applied at $2.5s$ for $\Delta P = 100\ W$. It can be seen in Fig. 2.30 and Fig. 2.31 that the virtual inertia controller is able to supply the desired frequency transient and frequency deviation proportional to the amplitude of the applied disturbances as per the design. Both load (and VSG) output voltages and currents at each step change are shown in Fig. 2.32 (a) and (b). Selected parameters (inertia M and damping D) have not caused any oscillation in output voltage / current and hence output electrical power.

This confirms the controller design and linear analysis and provides proof of its ability to mimic the SG behavior under the afore mentioned assumptions. The stability analysis, simulation, and later experimental work, based on this controller is discussed next.

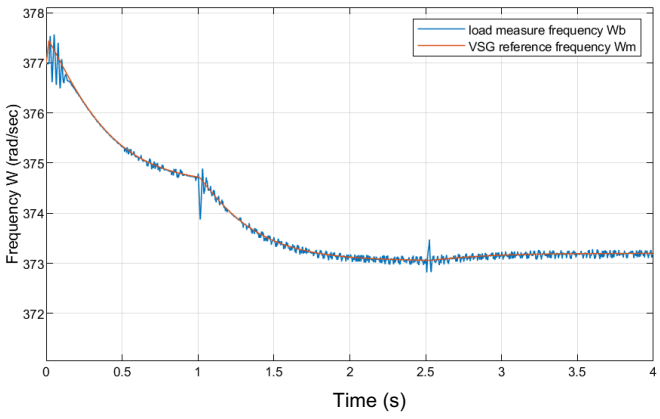

Fig. 2.31. VSG calculated virtual mechanical frequency ω_m versus load frequency ω_b

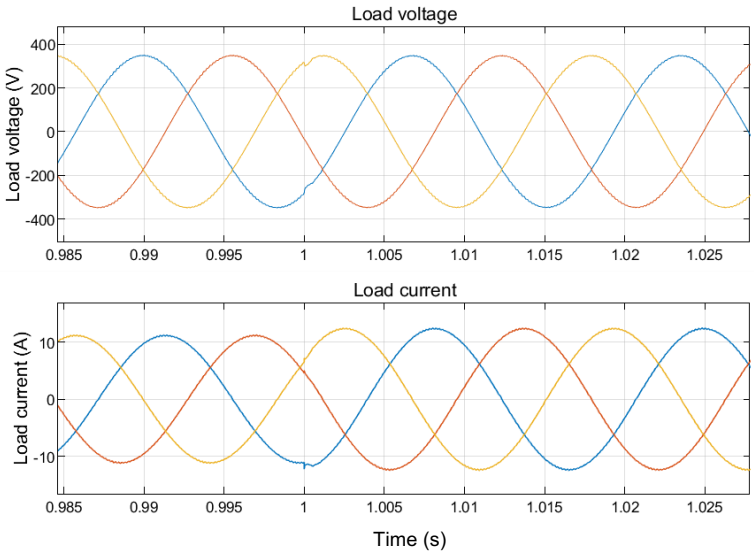

(a)

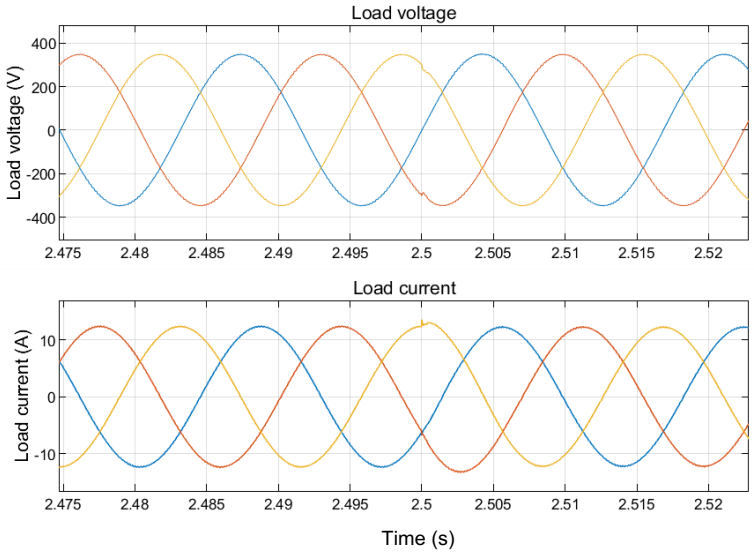

(b)

Fig. 2.32. Load voltage and current at step change; (a) at $t = 1s$ and $\Delta P = 600\ W$; (b) at $t = 1s$ and $\Delta P = 100\ W$.

3. Lyapunov Based Stability Analysis

3. 1. Introduction

A physical system is described as stable if it returns to its original equilibrium point (or one nearby) after a disturbance is applied. It is also stable if its states are bounded within some region, rather than going back to a certain point. It is unstable if its states grow continuously and cannot be bounded as $t \to \infty$. Such a generic definition of stability applies to both linear and nonlinear systems considering that in linear systems the bounded region of stability is shrunk to a single point which satisfies the linearization conditions.

A power system is considered stable if its forming VSGs keep their synchronism in the presence of disturbances at constant power angles, frequency, and voltage. If the disturbances are small i.e., they cause small changes in the system's states; therefore, a linearized microgrid model around its equilibrium point is sufficient to analyze its stability. In such a case, this analysis is referred to as small-signal stability analysis. In this regard, many techniques are available (such as Nyquist and Routh-Hurwitz) which provide a systematic approach to define system stability and its margins [54].

In case of disturbances of large magnitudes, the nonlinearities in a microgrid model become dominant and the linearized model is no longer valid. Examples of large disturbances are loss of a large load or occurrence of faults. In the literature, this type of stability study is often referred to as a transient stability [6], [35], [35], [55]. There are, in general, limited theories or criterions that provide a systematic approach to investigate the stability of such nonlinear systems [45], [48], [49]. The challenge is to accurately determine the bounds within which the microgrid's VSG will maintain their synchronism. The general intention is to track the amount of energy a system would gain and its rate of change. If such energy can be bounded in such a way that the system will lose it and go back to its equilibrium state, the system is then considered stable, and this bounded area is its stability margin. Otherwise, the system is unstable. The preceding general definitions of a nonlinear system and its stability are stated in technical terms in the following section [49].

3. 2. Stability of nonlinear systems

Stability of large dynamical system originally started with efforts to study the stability of the solar system, which is generalized and formulated as "the N-body problem". The aim was to understand the gravitational forces between N planets in the solar system that allows every planet's position to be fixed (be an equilibrium point) and to follow its own orbit without collision. It was found later by Laplace and Lagrange that in conservative systems, the state corresponding to zero kinetic energy and minimum potential energy is a stable equilibrium point. Later, it was shown that in dissipative systems at equilibrium, the total energy is decreasing along all trajectories. The formal definition and characterisation of stability was later done by Lyapunov in 1892 [45].

Lyapunov based his theory upon tracking the rate of change of energy of the overall system. If the rate of change dE/dt of the overall system energy $E(X)$ is negative for every system state $X = [x_i]$, except at the equilibrium state, such energy will decrease until it reaches its minimum value at the equilibrium state. In microgrid systems, finding $E(X)$ of a system that contains system states X is not guaranteed, especially in complex high order systems (as in the case of multiple VSGs).

In Lyapunov's approach, $E(X)$ is expressed by a scalar function $v(X)$ such that, the energy of each subsystem (VSG in a microgrid) can be aggregated by addition ($v(X) = v_1(x_1) + v_2(x_2) + v_3(x_3) \dots v_i(x_i)$). In order to be a Lyapunov candidate function, $v(X)$ must satisfy two conditions [49],

1) It must be positive definite for all states X within the area of interest (range of operation), and
2) Its derivative dv/dt must be negative everywhere for all $t > 0$ (not necessarily negative definite). This is true except at the equilibrium state X^s where $v(X^s)$ must approach its minimum value and its derivative $dv/dt = 0$ at $t \to \infty$.

In other words, in each microgrid transient (e.g., load transient), the difference between output power and input virtual power appears as exciting energy ΔE which is expressed by $v(X)$. Such energy will continually dissipate or be absorbed by *a priori* knowledge of system dynamics. Thus, the condition, $dv/dt < 0$ is satisfied. Eventually it will either

approach zero when the balance between input virtual power and output power is restored ($v(x) = 0$), or reach a minimum value $v(x) = v_{min}$, for example in case of sustained oscillation. In either case, the exciting energy is constant, and hence, its derivative is zero. A more formal definition of stability is discussed next.

3. 2. 1. Local stability:

An equilibrium point is stable (specifically at the origin in Lyapunov's definition) if for every $\varepsilon \in \mathbb{R}$ and $\varepsilon > 0$ there exists $\delta \in \mathbb{R}$ and $\delta > 0$ which depends on ε. Such that, for every initial condition X_o at $t = t_o$ the following inequality is satisfied:

$$||X_o|| < \delta$$

Hence, if for all $t > t_o$, the following inequality is satisfied, the system is said to be stable:

$$||X(t)|| < \varepsilon$$

In other words, the system is said to be stable, if when it starts from some initial condition X_o (close to the equilibrium point) with upper limit δ, it can go beyond that limit. However, it will not exceed another limit ε at all times. This means, the system experiences some sort of local stability, even though it doesn't necessarily go back to its equilibrium point, as illustrated in Fig. 3.1. Although, this is mathematically sufficient, it doesn't suffice in electrical systems, where it is desired that the system goes back to its reference equilibrium point once the transient ends.

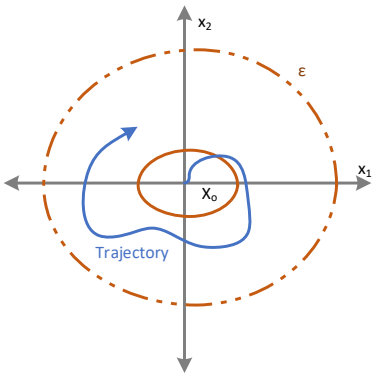

Fig. 3.1. Illustrative trajectory of local stable system

3. 2. 2. Local asymptotic stability:

The system is said to be asymptotically stable, if for every $\varepsilon \in \mathbb{R}$ and $\varepsilon > 0$ there exists $\delta \in \mathbb{R}$ and $\delta > 0$ which depends on ε, such that for every initial condition X_o at $t = t_o$ the following inequality is satisfied:

$$||X_o|| < \delta$$

The system will converge back and asymptotically approach the equilibrium point X_e:

$$\lim_{t \to \infty} ||X(t)|| = X_e = 0$$

This form of stability is the desired one in electrical systems. It states that if the system i.e., microgrid is excited due to a short fault, for example, it will go back to its exact operating point once the fault is cleared. Typical illustrative trajectory of such a system is shown in Fig. 3.2. As mentioned in the pervious section, microgrid linearized model has only one equilibrium point (due to linearization around that one point), thus asymptotic stability is guaranteed. The microgrid is nonlinear, and it has multiple equilibrium points.

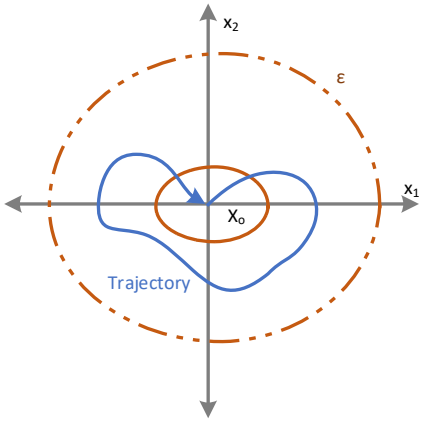

Fig. 3.2. Illustrative trajectory of local asymptotic stable system

Two remarks are worth mentioning. First, the areas defined by ε and δ are not necessarily circles and can be of any irregular shape and dimensions. Second, earlier definitions describe stability locally. A global definition of stability is possible by setting

$\varepsilon \to \infty$ and $\delta \to \infty$, as shown in Fig. 3.3. Such definitions are not common in electrical systems and specially in microgrids, and it is not within the scope of this study.

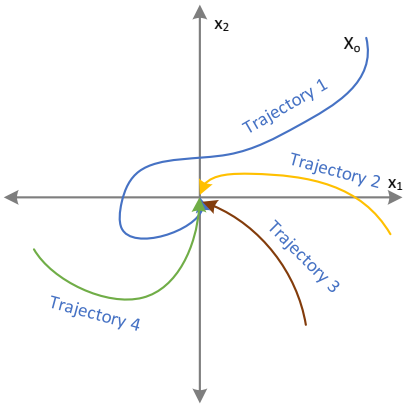

Fig. 3.3. Illustrative trajectories of global asymptotic stable system

3. 2. 3. Region of attraction:

In a nonlinear stability study, the challenge is to find the region ε which surrounds the equilibrium point and gives the boundaries of stability [56]. Such that, if a VSG trajectory in a microgrid stays within it will go back to stability (after a fault, for example), or becomes unstable if the trajectory crosses it to the next undesirable equilibrium point. This region is known as the region of attraction or the area of attraction in two dimensional systems [49]. The time a microgrid takes to reach its boundary is known as the maximum clearing time t_{cr} [41]. This time is tied to the smallest amount of energy defined by the Lyapunov energy function $v(X)$ that enables the system to reach the boundary of the stability region ε. This concept forms the basis of this stability study. Therefore, stability conditions of a microgrid can be determined by performing the following steps sequentially:

1- Construct a proper Lyapunov energy function $v(X)$ that describes the n^{th} VSG within a microgrid.
2- Determine the lower limit $v_{min}(X)$ of the energy mismatch the microgrid can gain to enter the unstable region (i.e., go beyond the area of attraction).
3- Determine t_{cr} using a numerical integration method.

From a mathematical point of view, finding a Lyapunov energy function can be done by linearly summing the energy of each sub-system (individual VSGs in a microgrid). However, finding a representative energy function of inter-connected n number of VGSs is not direct and it will need to be redone every time something changes in the microgrid topology (e.g., changing loads or VSGs locations).

Fortunately, many methods are available which offer a systematic way of constructing suitable Lyapunov energy functions such as Zupov's and Popov's methods [57]. They may even supply a direct estimate of the area of attraction as is the case in Zupov's method for a single power source connected to an infinite bus (large electric grid). The method adopted in this study is based on Popov's multivariable criterion, which is suitable for a microgrid with n connected VSGs. A brief illustration of Popov's method, and its extension to multivariable version, is provided next.

3. 3. Systematic construction of Lyapunov function using Popov's method

3. 3. 1. Popov's method for single VSG

Lyapunov theory gives sufficient conditions for local and global stability. It doesn't, however, provide a systematic approach to construct a suitable energy function (Lyapunov function $v(X)$), or estimate the region of attraction around the equilibrium point. It is particularly difficult in systems without restrictions on their nonlinearities. When it can be restrained, Popov's method offers a systematic approach to construct the Lyapunov function for a system with its nonlinearity found in the first and third quadrants of 2-dimensional Cartesian coordinates. This method can be extended for multi-input multi-output systems, which makes it suitable for microgrids with n VSGs.

There are two conditions a system must satisfy before applying Popov's method. First, the system can be deconstructed and represented as two sub-systems in feedback architecture, as shown in Fig. 3.4. The linear part is to be placed in the forward path while the nonlinearity is placed in the feedback. Secondly, such a nonlinearity must be limited to the first and third quadrants, which is referred to as the quadrant condition.

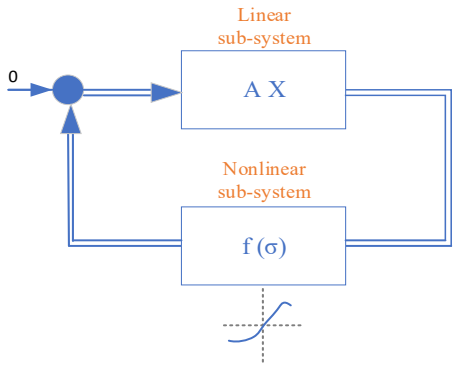

Fig. 3. 4. System block diagram with affined nonlinearity limited to the first and third quadrants

The notion behind Popov's criteria and its conditions can be explained considering the passivity theorem applied to power systems. Suppose that a one-port circuit has an input $v(t)$ that excites an output current $i(t)$, like the one shown in Fig. 3.5 (a). If the product of the input and output is always non-negative i.e., $v(t)\ i(t) \geq 0$ for all $v(t)$ and $i(t)$ and all times $t > 0$, the circuit is called passive. This means that the circuit has only passive components, ideally resistors which do not generate power, only consume it. The relation between the input and output can be written as $v(t) \geq G\ i(t)$, where G is the constant which represents circuit impedance. The plot between input and output $v - i$ in this relation is a line with a slope G which is limited to the first and third quadrants, as shown in Fig. 3.5 (b). The quadrant condition shown in Fig. 3.5 (b) is generalized in Fig. 3.5. (c). An example of a non-passive system characteristic is shown in Fig. 3.5 (d).

This explains the necessity of the quadrant condition in Popov's criteria. That is, if a system is passive (by complying to the quadrant condition) and it gains a certain amount of energy $v(X)$, it can only dissipate this energy without always generating any ($\dot{v}(t) < 0$). Thus, the system is asymptotically stable [49], [58]. The generalized definition for multi-port systems is for inputs vector V and output vector I, the system is passive if $I^T V = \Sigma v_i(t)\ i_i(t) \geq\ 0$ for all $t > 0$.

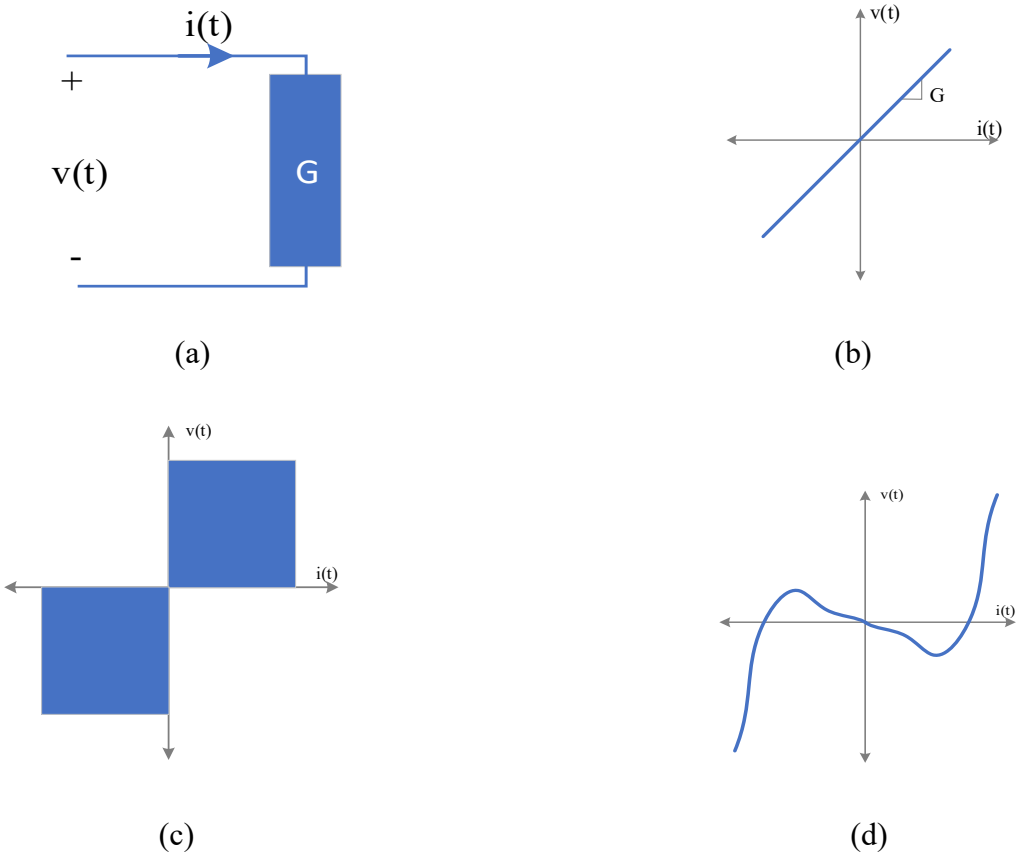

Fig. 3. 5. (a) one-port circuit; (b) characteristic curve of passive one-port circuit (resistor); (c) generalized quadrant condition; (d) example of non-passive system that doesn't comply to quadrant condition.

For a system that satisfies the afore mentioned conditions, Popov's criteria gives a stability definition like Nyquist's criteria in the frequency domain, and it is described as follows:

For a system with a transfer function defined in the complex domain $G(j\omega)$,

$$G(j\omega) = x(\omega) + j\, y(\omega) \tag{3.1}$$

Where, $j = \sqrt{-1}$ and ω is the angular frequency.

Then, there exist real numbers q and k such that:

$$\frac{1}{k} + Re\{(1 + j\omega q)G(j\omega)\} > 0 \tag{3.2}$$

Then

$$\frac{1}{k} + Re\{(1 + j\omega q) \quad (x(\omega) + j\, y(\omega))\} > 0 \tag{3.3}$$

$$\frac{1}{k} + x(\omega) - \omega q\, y(\omega) > 0 \tag{3.4}$$

The inequality can be rearranged as follows:

$$x(\omega) > \omega q\, y(\omega) - \frac{1}{k} \tag{3.5}$$

This means, to apply Popov's criteria for the system $G(j\omega)$, there must exist a line with a slope q which passes through the point $\left(-\frac{1}{k}, 0\right)$, known as Popov's line, as shown in Fig. 3.6. This line forms the upper left bound of the system response i.e., the curve $x(\omega) - j\,\omega y(\omega)$ lies completely beneath it, which ensures satisfaction of the quadrant condition (at $k = \infty$). This is analogous to the Nyquist criteria in a linear system, where the point -1 is expanded to be a circle (or a ball in multi-dimension) and Popov's line is its tangent.

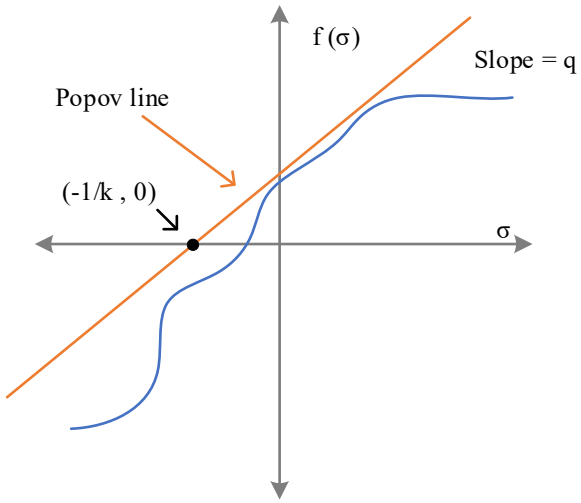

Fig. 3. 6. Typical Popov's line bounding nonlinear system

A VSG model also satisfies the first condition as its nonlinearity is decomposed and added to the linear part, which can be seen as follows:

$$\dot{X} = AX + B\gamma$$

$$\gamma = -f(\sigma) \tag{3.6}$$

$$\sigma = CX$$

Where AX is the linear part, and $B\gamma$ is the nonlinear part.

The nonlinearity in the VSG model comes from the sinusoidal relation between the output power and power angle and is formulated by the swing equation. It satisfies the quadrant condition, as shown in Fig. 3.7.

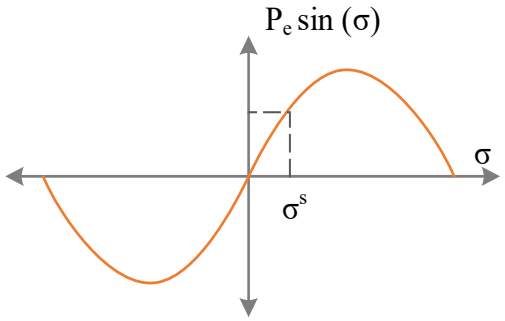

Fig. 3. 7. Swing equation of VSG satisfies the quadrant condition of Popov's criterion

Thus, the generic construction of Lyapunov's function for a single VSG can be based on the Kalman-Yakubovich-Popov lemma [59] as follows:

$$v(X) = X^T PX + q\int_0^{\sigma} f(\sigma)\, d\sigma \tag{3.7}$$

For a single VSG, the state space model is as follows:

$$\dot{X} = AX + Bf(\sigma)$$

$$\sigma = CX \tag{3.8}$$

Where,

$$A = \begin{bmatrix} 0 & 1 \\ 0 & \frac{-D}{M} \end{bmatrix}, B = \begin{bmatrix} 0 \\ -\frac{1}{M} \end{bmatrix}, C = \begin{bmatrix} 1 \\ 0 \end{bmatrix}$$

$f(\sigma) = P_e(\sin(\sigma + \sigma^s) - \sin(\sigma^s))$

The transfer function of the linear sub-system is obtained by dividing the output matrix by the input matrix at the stable operating point, as follows:

$$G(s) = C^T(SI - A)^{-1}B \tag{3.9}$$

$$G(s) = \frac{1}{s\left(s + \frac{D}{M}\right)} \tag{3.10}$$

The nonlinear sub-system in plotted in Fig. 3.7 where the nonlinearity is confined to the first and third quadrants of $\sigma \rightarrow f(\sigma)$ axis, as per Popov's criteria. By applying Popov's inequality at $k = \infty$, Popov's line will pass through (0,0), as shown in Fig. 3.8.

Hence, the inequality becomes:

$$Re\left\{ (1 + j\omega q) \quad \frac{1}{s\left(s + \frac{D}{M}\right)} \right\} \geq 0 \tag{3.11}$$

Then,

$$\frac{q\frac{D}{M} - 1}{\frac{D^2}{M^2} + \omega^2} \geq 0 \tag{3.12}$$

And

$$q\frac{D}{M} \geq 1 \tag{3.13}$$

Thus, q can be defined from the inequality as $q = \frac{M}{D}n$, where $n \geq 1$.

Lyapunov's function is constructed as follows:

$$v(X) = \frac{1}{2} M \left(\frac{D}{M} x_1 + x_2\right)^2 + q \int_0^{\sigma} f(\sigma)\, d\sigma \tag{3.14}$$

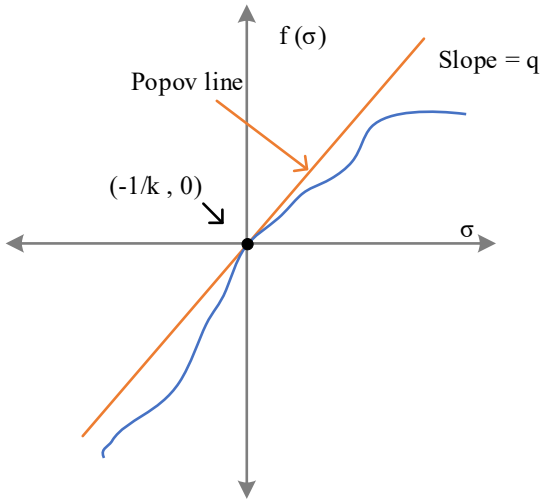

Fig. 3. 8. Typical Popov's line bounding nonlinear system at $k = \infty$

Based on this function, the area of asymptotic stability can be defined, which determines the maximum energy a single VSG can experience due to a load transient or fault without going out of stability. This is also under the assumption that no line switching has occurred. This also is used to determine the maximum clearing time t_{cr} of a VSG with respect to its parameters due to the occurrence of faults, which is introduced in a later section.

3. 3. 2. Popov's method for a multi-VSG MG

Popov's criterion is extended for multi-input multi-output systems by Moore-Anderson theorem [45], which allows the preceding methodology to be applicable to a microgrid with multiple VSGs. The system matrices A, B, and C are configured by blocks that represents one of the VSGs, while the model construction is reserved. The structure of n VSGs' simplified model (by ignoring for now modified model derived in chapter 2) is based on [41], [43], and can be written for four VSGs ($n = 4$) as follows:

$$\dot{X} = AX + Bf(\sigma)$$

$$\sigma = CX \tag{3.15}$$

Where:

$x = [\omega_1, \omega_2, \omega_3, \omega_4, \sigma_1, \sigma_2, \sigma_3]^T$; $\sigma = [\sigma_1, \sigma_2, \sigma_3, \sigma_4, \sigma_5, \sigma_6]^T$;

$\sigma_k =$ $\delta_{mn} - \delta_{mn}^s$ for $m = 1, 2, 3, \ldots$ and $n = m - 1$

$f(\sigma) = [f_1(\sigma_1), f_2(\sigma_2), f_3(\sigma_3), f_4(\sigma_4), f_5(\sigma_5), f_6(\sigma_6)]^T$

And

$$A = \begin{bmatrix} \frac{D_1}{M_1} & 0 & 0 & 0 & 0 & 0 & 0 \\ 0 & \frac{D_2}{M_2} & 0 & 0 & 0 & 0 & 0 \\ 0 & 0 & \frac{D_3}{M_3} & 0 & 0 & 0 & 0 \\ 0 & 0 & 0 & \frac{D_4}{M_4} & 0 & 0 & 0 \\ 1 & 0 & 0 & -1 & 0 & 0 & 0 \\ 0 & 1 & 0 & -1 & 0 & 0 & 0 \\ 0 & 0 & 1 & -1 & 0 & 0 & 0 \end{bmatrix}$$

$$B = - \begin{bmatrix} \frac{1}{M_1} & 0 & 0 & \frac{1}{M_1} & \frac{1}{M_1} & 0 \\ 0 & \frac{1}{M_1} & 0 & \frac{-1}{M_2} & 0 & \frac{-1}{M_2} \\ 0 & 0 & \frac{1}{M_3} & 0 & \frac{-1}{M_3} & \frac{-1}{M_3} \\ \frac{-1}{M_4} & \frac{-1}{M_4} & \frac{-1}{M_4} & 0 & 0 & 0 \\ 0 & 0 & 0 & 0 & 0 & 0 \\ 0 & 0 & 0 & 0 & 0 & 0 \\ 0 & 0 & 0 & 0 & 0 & 0 \end{bmatrix}$$

$$C = \begin{bmatrix} 0 & 0 & 0 & 0 & 0 & 0 & 0 \\ 0 & 0 & 0 & 0 & 0 & 0 & 0 \\ 0 & 0 & 0 & 0 & 0 & 0 & 0 \\ 0 & 0 & 0 & 1 & -1 & 0 & 0 \\ 0 & 0 & 0 & 1 & 0 & 0 & -1 \\ 0 & 0 & 0 & 0 & 0 & 1 & -1 \end{bmatrix}$$

$$f(\sigma) = \begin{bmatrix} |E_1||E_4|\, B_{14}\, (\sin(\sigma_1 + \delta_{14}^s) - \sin \delta_{14}^s) \\ |E_2||E_4|\, B_{24}\, (\sin(\sigma_2 + \delta_{24}^s) - \sin \delta_{24}^s) \\ |E_3||E_4|\, B_{34}\, (\sin(\sigma_3 + \delta_{34}^s) - \sin \delta_{34}^s) \\ |E_1||E_2|\, B_{12}\, (\sin(\sigma_4 + \delta_{12}^s) - \sin \delta_{12}^s) \\ |E_1||E_3|\, B_{13}\, (\sin(\sigma_5 + \delta_{13}^s) - \sin \delta_{13}^s) \\ |E_2||E_3|\, B_{23}\, (\sin(\sigma_6 + \delta_{23}^s) - \sin \delta_{23}^s) \end{bmatrix}$$

Popov's inequality is essentially the same by considering the coefficient q in Popov's line slope $\frac{1}{q}$ (at $k = \infty$) as a diagonal matrix $Q = qI$ (I is the identity matrix) and $n = 1$, as follows:

$$Re\{(1 + j\omega Q)\, G_n(j\omega)\} > 0 \tag{3.16}$$

Where, $G_n(j\omega)$ is the transfer function of n VSG.

The inequality is satisfied at $q_i \geq \frac{M_i}{D_i}$ for the i^{th} VSG as concluded in single VSG case, and the elements of the diagonal matrix Q are $q_i \geq \frac{M_i}{D_i}$, $i = 1, 2, \dots, n$.

There are many ways to construct a Lyapunov function in a microgrid with n VSGs based on: a) the preceding inequality and b) the freedom of choosing different q's among other parameters. That is, if:

1) The inequality is satisfied,
2) The resultant function is positive definite,
3) And Popov's line properly bounds the nonlinearity in the system.

The selection of q_i in this work is based on Pai and Murthy [60] for a large-scale power system as follows:

$$q = \sum_{i=1}^{n} q_i = \sum_{i=1}^{n} \frac{M_i}{D_i} \tag{3.17}$$

Thus, Lyapunov function is regarded as follows:

$$v(X) = \frac{1}{2} \sum_{i=1}^{n} \sum_{\substack{j=1 \\ j \neq i}}^{n} \frac{M_j}{D_j} M_i \omega_i^2 + \frac{1}{2D_T} \sum_{i=1}^{n} M_i^2 \omega_i^2$$

$$+\frac{1}{2D_T}\sum_{i=1}^{n-1}\sum_{j=i+1}^{n} D_i D_j\left(\delta_i-\delta_i^s+\delta_j^s-\delta_j+\frac{M_i}{D_i}\omega_i-\frac{M_j}{D_j}\omega_j\right)^2 \tag{3.18}$$

$$+\sum_{i=1}^{n}\frac{M_i}{D_i}\sum_{i=1}^{m}\int_0^{\sigma} f_i(\sigma_i)\,d\sigma_i$$

3. 4. Estimation of region of asymptotic stability (region of attraction)

Every VSG in a stable microgrid supplies its power share at a fixed power angle δ_i, and fixed frequency with respect to a reference VSG. The rate of change of frequency (RoCoF) of each individual VSG and in the microgrid frequency in total under such conditions is zero. Then, every VSG resides at its own stable equilibrium (fixed) operating point.

Upon a large transient, disturbance, or fault mismatch in the virtual energy within each VSG causes change in their power angle and non-zero rate of change in frequency. The trajectory that describes the behavior of each VSG travels away from the stable equilibrium point to another point, until the disturbance is cleared. The VSGs ability to return to their equilibrium points is mandated by certain energy threshold $v(X)$. The area around the stable point which the trajectory can branch out without loosing the ability to come back to that point is the area of attraction or area of asymptotic stability of the VSG(s). The aim here is to find the lower upper bound of such area, which defines the maximum energy and time the trajectory of each VSG can have without entering the unstable areas around it.

Although qualitative estimation of such an area is possible by seeing the vector field of a single VSG microgrid. An analytical approach is desirable to enable clear and precise judgement. More importantly, microgrid formed by multiple VSGs (with n VSGs) is an interconnected and coupled system, which is harder to visualize and to extract its qualitative properties. Hence, analytical approach (despite how conservative it is) is more suitable.

3. 4. 1. Single VSG microgrid

In a single VSG microgrid, the grid becomes unstable if the disturbed VSG reaches one of its unstable equilibrium points ($\pi - 2\delta_i^s,\ 0$), or ($\pi + 2\delta_i^s,\ 0$). This condition sets the lower upper limit of its area of attraction. The amount of energy the VSG needs to gain/lose to reach such a boundary can be calculated based on the afore mentioned Lyapunov function for single VSG $v(X^u)$ evaluated at these unstable points. The point that gives the lower value of the Lyapunov function $v_{min}(X)$ forms the boundary of the area of attraction and used to calculate system's critical time t_{cr} [41].

$$v_{min}(X) = \frac{1}{2}\, M \left(\frac{D}{M}\, x_1 + x_2\right)^2 + q \int_0^{\sigma} f(\sigma)\, d\sigma \tag{3.19}$$

It is worth mentioning that the quadratic term of the Lyapunov function when evaluated at the unstable equilibrium points ($x_1 = \sigma = \pi \pm 2\delta_i^s$ and $x_2 = 0$) is much smaller than the integral term and can be neglected.

Hence,

$$v_{min}(X) = q \int_0^{\sigma=\pi\pm 2\delta_i^s} f(\sigma)\, d\sigma \tag{3.20}$$

Once $v_{min}(X)$ is obtained, the nonlinear model of a single VSG microgrid can be numerically integrated with the corresponding unstable point as its initial value, and then solved for t_{cr}.

The introduced method is used to find the stability margin of a microgrid configured by single VSG. The single line diagram of the microgrid is shown in Fig. 3. 9 which shows a single VSG connected to a load Ld_1 and to utility grid v_g. The utility grid is represented by a slack bus that has a fixed voltage $v_g = E = 1\angle 0°\ p.u.$, power angle and frequency ω_g. Thus, it is taken as the microgrid's power angle $\delta_g = 0°$ and frequency references $\omega_g = 1$. It is also assumed that the effect on the utility's voltage, and frequency is minimal and can be neglected in this scenario. The rest of the parameters are listed in Table 3. 1.

Before proceeding with the stability analysis, the key properties of the introduced methodology can be further demonstrated. The VSG is modeled using equation (3.6) and it is simplified by considering an undamped condition i.e., the damping factor is set to zero. This helps wrapping up the area of attraction more tightly as seen here. The relationship between its power angle $x_1 = \delta\ rad$ and deviation in frequency $x_2 = \omega\ rad/s$ is described by its vector field, as shown in Fig. 3.10. All trajectories initiated within proximity of the stable point (labelled by a green dot) do not approach this steady state point exponentially but take a very slow decay towards it. This is translated into a very slow decaying oscillation in VSG power angle and frequency what matches the behaviour expectancy in such a case (undamped system).

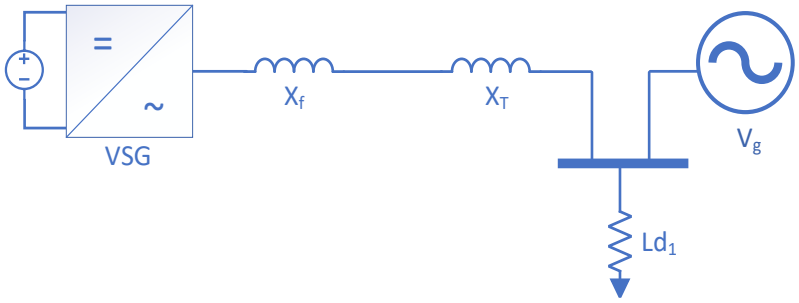

Fig. 3. 9. Simplified single line diagram of single VSG microgrid

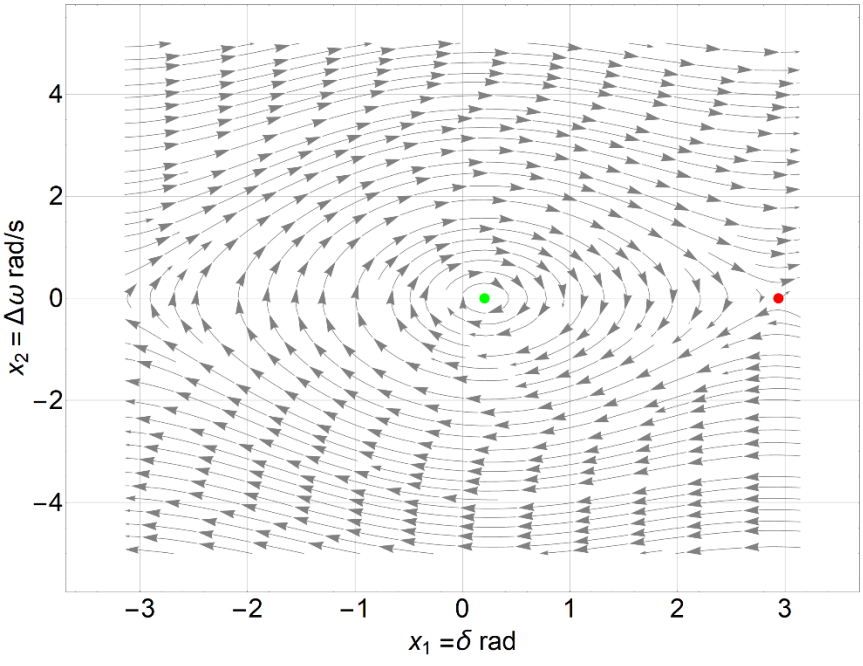

Fig. 3.10. Vector field of undamped single VSG.

It can also be seen that not all trajectories will approach the steady-state point despite their initial point. Rather, there exists a finite region around the equilibrium point (indicated by the green dot in the figure) if the trajectory starts within such a region, it will always fall back to that point (area of attraction). Otherwise, it will approach another unstable point. Such areas can be intuitively observed in the upper and lower third regions of Fig. 3.10.

The boundary of the area of attraction surrounds the stable equilibrium point and is constructed using the introduced method. First, Lyapunov function $v(X)$ is constructed using equation (3.19) for the undamped VSG model. Second, it is evaluated at the two unstable points next to the desired stable one $v(X^{u1})$ and $v\ (X^{u2})$ and the results were as follows:

$$v_1(\pi + \delta^{u1}) = 5.8295 \qquad \text{and} \qquad v_2(\pi - \delta^{u2}) = 6.1951$$

The contour corresponding to v_1 and v_2 is plotted using equation (3.21) and (3.22) over the vector field of the VSG in Fig. 3.11. The area of attraction defined by v_1 is plotted in red contour while the one defined by v_2 is plotted in blue contour. The red contour accurately defines the stable area around the stable equilibrium point while the blue contour is more conservative especially close to the unstable point. In the introduced method, the conservative case is considered to ensure safe stable operation. Also, as will be seen later, the conservative value is better approximate the area of attraction within the range of operation in a sense that it cuts off some stable regions as opposed to the non-conservative estimation v_2 that would include them in addition to some unstable regions. This matches the introduced method where the conservative estimation is corresponding to the minimum value of $v_{min} = v_1 = 5.8295$ (the blue contour).

$$v_1 = \frac{1}{2}\, M \left(\frac{D}{M}\, x_1 + x_2\right)^2 + q \int_0^{\sigma} f(\sigma)\, d\sigma \;\; - - - \rightarrow \;\; v_1 = 5.8295 \tag{3.21}$$

$$v_2 = \frac{1}{2}\, M \left(\frac{D}{M}\, x_1 + x_2\right)^2 + q \int_0^{\sigma} f(\sigma)\, d\sigma \;\; - - - \rightarrow \;\; v_2 = 6.1951 \tag{3.22}$$

Note that, the damping coefficient D is set to very small value $0.001\ p.u.$ to prevent dividing by zero in $q = M/D$.

In other words, Lyapunov function describes VSG exciting energy levels and can be visualized as a hyper-plane in 3D which is shown in Fig. 3.12. Every contour is an intersection between it and another plane that represents a certain energy level (e.g., v_1 or v_2). The projection of the curve that is the result of the intersection of these planes on the vector field plot encircles part of the system dynamics. The aim is to find a plane (i.e., energy level) that only defines a stable region around the stable equilibrium point.

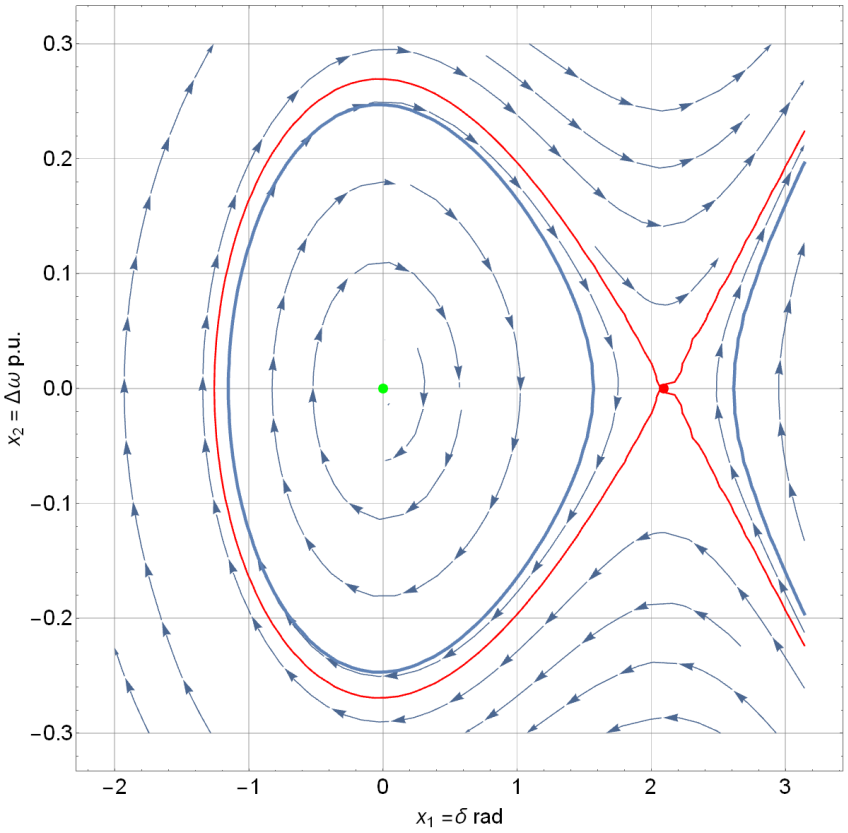

Fig. 3.11. Area of attraction of single VSG microgrid at zero damping; v_1 in blue contour and v_2 in red contour.

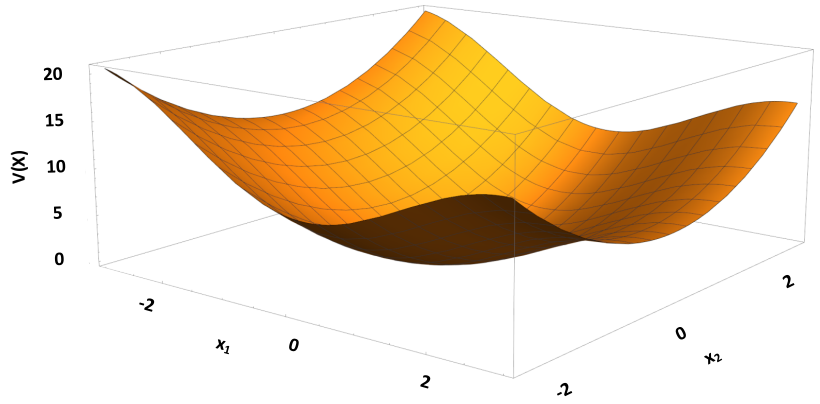

Fig. 3.12. $v(X)$ of single VSG microgrid

The general case is considered next. The stability of a damped VSG in a single VSG microgrid (Fig. 3.9) is studied considering the following scenario. The dynamics of the damped VSG is shown in Fig. 3.13 which has $1\ p.u.$ damping coefficient. Its stable equilibrium operating point is identified by the green dot while its unstable one is shown as a red dot. A three phase to ground fault is applied at its output as shown in Fig. 3.14. The VSG controller is disconnected from it for a certain period t. The aim is to find the largest period it can be disconnected before being unable to restore synchronism with the utility grid and return to the same equilibrium point.

To facilitate the study, the following assumptions are considered.

- System configuration before the fault is the same after the fault is cleared. Hence, Fig. 3.13 describes system behavior in pre-fault and post-fault conditions.
- System virtual mechanical input changes very slowly and can be considered constant.

Table 3.1. Single VSG microgrid parameters

Parameter	**Value**
Virtual input power P_m	$0.5\ p.u.$
Power electrical power P_e	$0.5\ p.u.$
Power angle at steady state δ	$0.203\ rad$
Grid power angle δ_g	$0\ rad$
Line impedance x_g	$0.43\ p.u.$
Grid line voltage v_g	$1\ p.u.$
Active power droop coefficient K_p	0.03
Reactive power droop coefficient K_q	0.03
Damping constant D	$1\ p.u.$
Inertial Constant M normalized	$2\ s$
Simulation step time	10 us

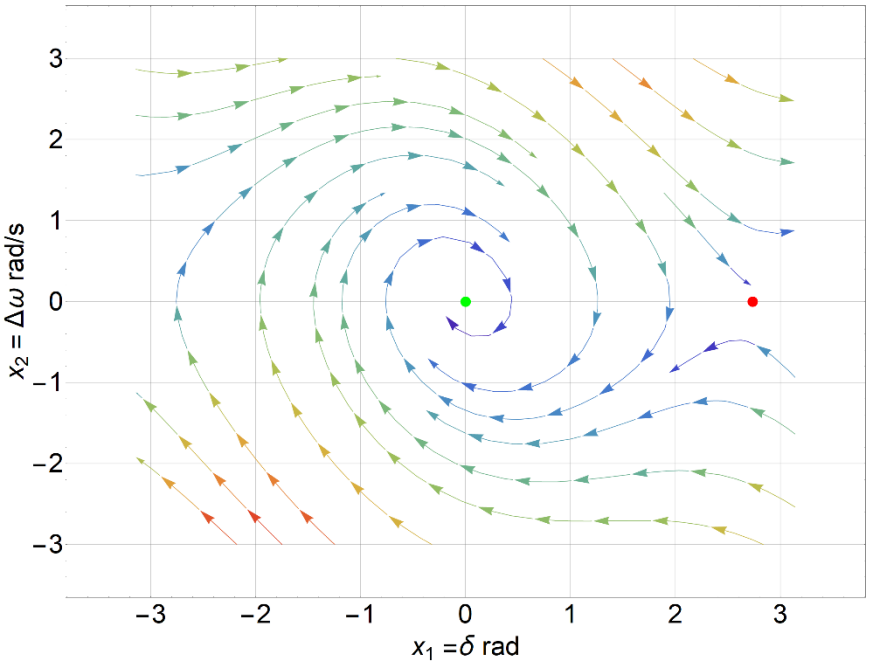

Fig. 3. 13. The dynamics of the damped VSG with 1 $p.u.$ damping

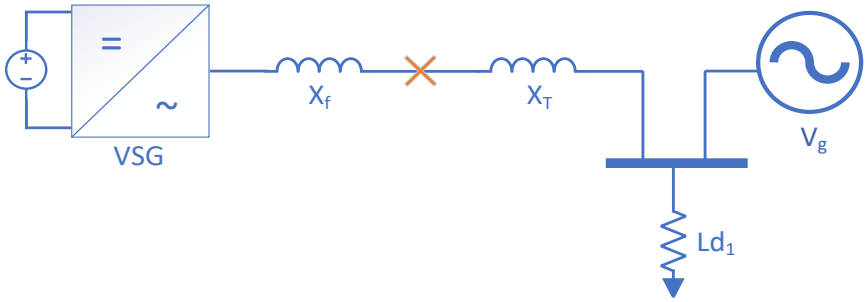

Fig. 3. 14. Faulted system

Based on the parameters in Table 3.1, a compact VSG model in pre- and post-fault conditions can be written as follows:

$$\dot{x_1} = x_2$$

$$\dot{x_2} = -\frac{1}{2}(x_1 + 0.5 - P_e \sin(x_1 - \delta^s)) \tag{3.23}$$

And its model during the afore mentioned fault is as follows:

$$\dot{x_1} = x_2$$

$$\dot{x_2} = -\frac{1}{2}(x_1 + 0.5) \tag{3.24}$$

As the upper bound limit of its Lyapunov function $v_{min}(X)$ calculated in equation (3.19) is redone here to consider the damping coefficient D. Same formula and procedure described earlier is used here. At the two neighborhood unstable equilibrium points $(\pi + \delta^{u1})$ and $(-\pi + \delta^{u2})$, the values of $v_1(X^{u1})$ and $v_2(X^{u2})$ are as follows:

$v_1(\pi + \delta^{u1}) = 7.6266$ and $v_2(-\pi + \delta^{u2}) = 12.5525$

The two contours are plotted as earlier, but for non-zero damping which are shown in Fig. 3. 15. It can be seen that, both estimations do not define exactly the area of attraction around the desired equilibrium point. However, by following the introduced method, the conservative value v_1 (in blue contour) is chosen to be the VSG upper bound of its area of attraction $v_{min} = v_1$ as $v_1 < v_2$. By observing the plots in Fig. 3. 15, one can see that all integral solutions (arrows) found inside the area defined by energy level v_1 go exponentially towards the stable equilibrium point (within the range of operation $(-\pi\ to\ \pi)$. On the other hand, not all the ones inside the area defined by v_2 (the red contour) follow the same behavior as can be observed within its upper section.

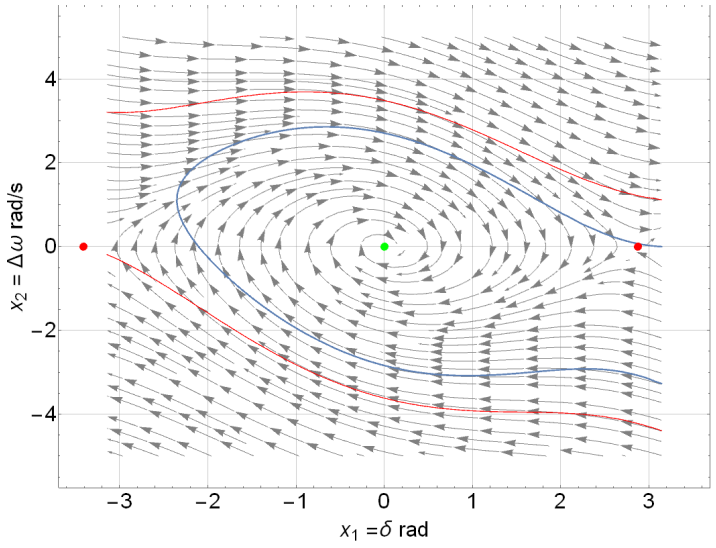

Fig. 3. 15. Area of attraction of single VSG microgrid at zero damping v_1 in blue and v_2 in red.

The last step is it to integrate the faulted model (equation (3.24)) and substitute in $v(X)$ at every time interval Δt. When $v(X)$ approaches $v_{min}(x)$ the VSG reaches its stable boundaries and will go unstable for the upcoming time intervals. The time at which $v(X) = v_{min}(x)$ is the maximum it can pass before the VSG losses its ability to reconnect again to the microgrid t_{cr}.

More precisely, the faulted trajectory reaches the point ($x_1 = 2.65\, rad,\ x_2 = 0.44\, rad/s$) at $t = 6.85\, s$ as shown in the faulted trajectory in Fig. 3. 16. At such a point, VSG's Lyapunov function $v(X)$ is equal to its lower upper limit $v_{min}(X)$ calculated before. Its power angle x_1 and frequency deviation x_2 are depicted in Fig. 3.17 (a) and (b) respectively, which matches the analytical values.

After the fault is cleared, VSG restores its dynamics (depicted in Fig. 3.13) and starts to approach its pre-fault equilibrium point, as shown in Fig. 3.18 in the black curve. The Fig. 3.19 shows VSG power angle and frequency dynamics starting from the faulted position and ending at the stable equilibrium point. Therefore, the time $t = 6.85\, s$ is the VSG clearing time t_{cr}.

A last remark, if the VSG is not connected before $t = t_{cr}$, it will not go back to its initial point equilibrium point and a resynchronization procedure is needed. This case is shown in Fig. 3.20 which represents trajectory crossing the area of attraction.

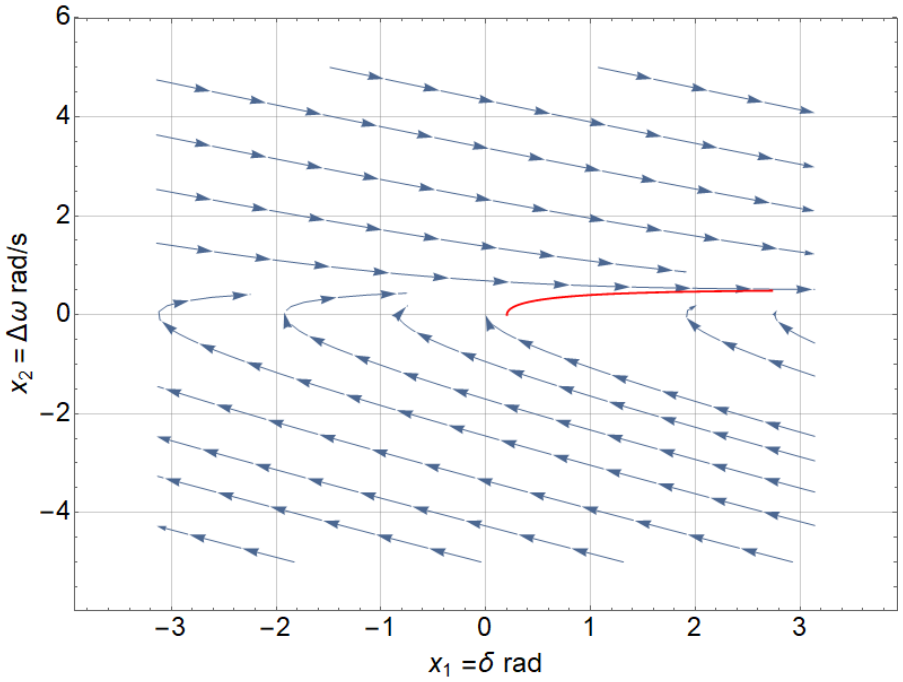

Fig. 3. 16. Vector filed of faulted VSG in single VSG microgrid

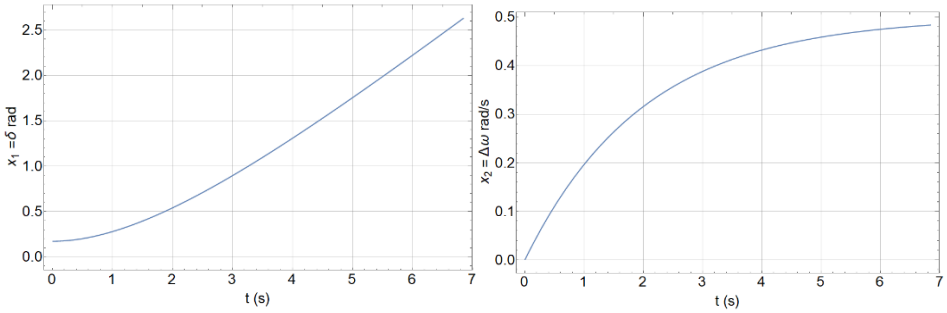

(a) (b)

Fig. 3. 17. Faulted system power angle and frequency (a) power angle x_1 of the faulted VSG; (b) frequency deviation x_2 of the faulted VSG.

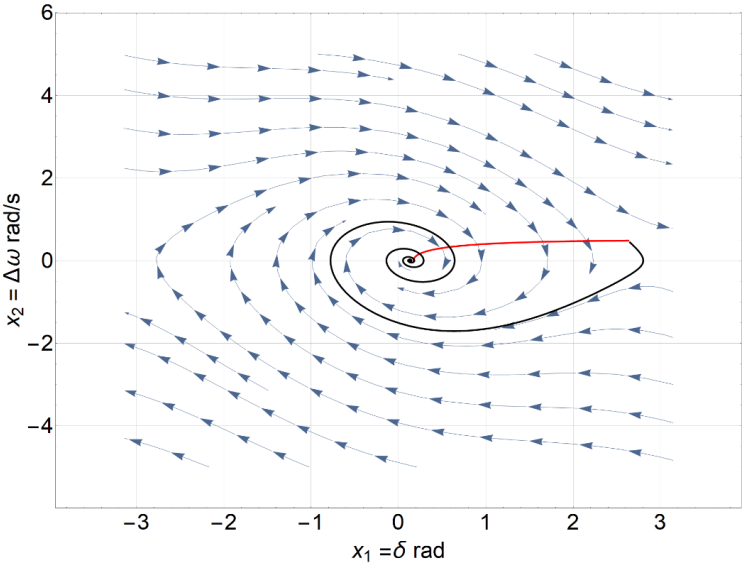

Fig. 3. 18. Vector filed of post-fault VSG in single VSG microgrid

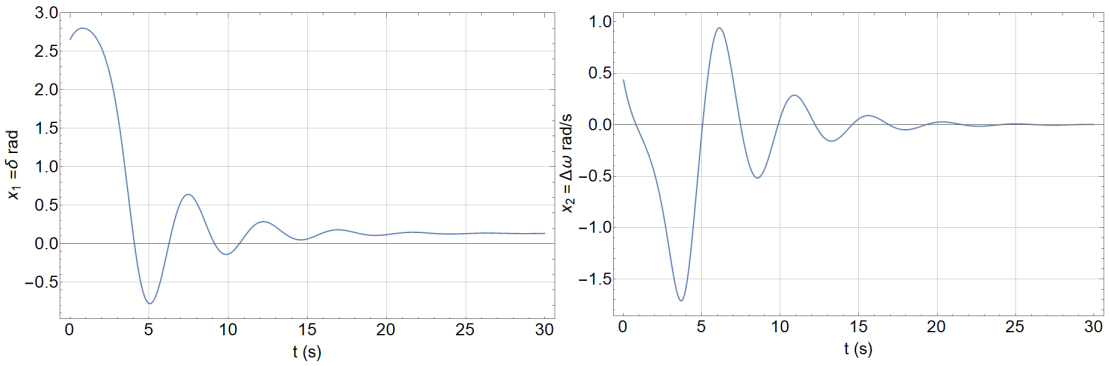

(a) (b)

Fig. 3. 19. (a) power angle x_1 of the post-faulted VSG; (b) frequency deviation x_2 of the post-fault VSG.

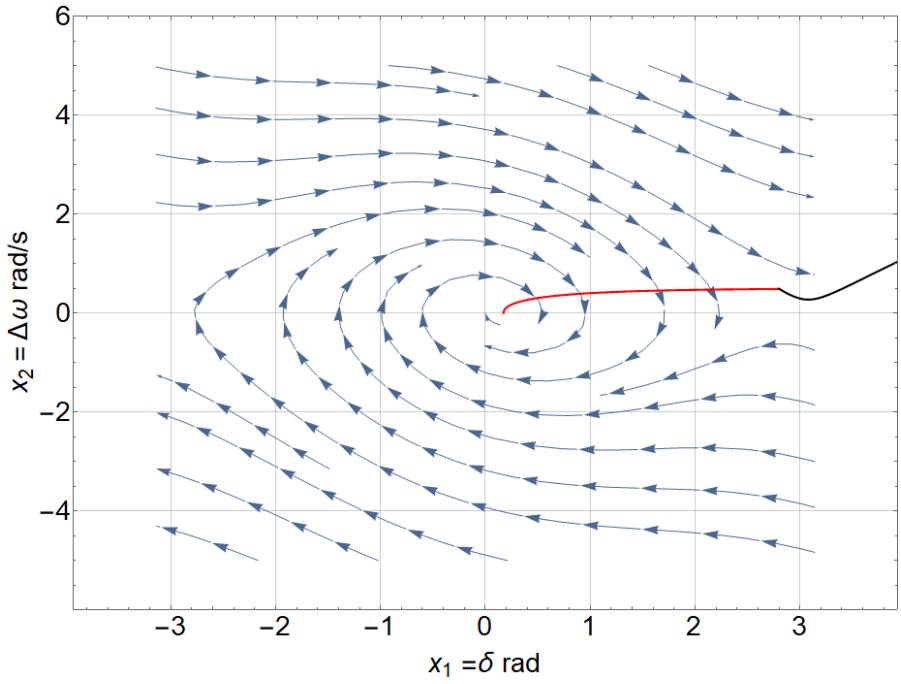

Fig. 3. 20. VSG trajectory at reconnection at $t > t_{cr}$

In summary, the introduced method provides a systematic direct construction of Lyapunov function for VGS in a microgrid, and an estimate of its area of attraction. The conservation in the estimation is within an acceptable range for microgrid application where the complexity of the system is lower when compared with a conventional electric grid. Furthermore, microgrids are typically spread over a limited geographic area with short transmission lines, which reduces the effect of the location of the disturbance on the estimated area of attraction. The effect of the location of the disturbance is more pronounced in large-scale power system, which necessitate some adjustments in evaluation methods and points [60].

3. 4. 2. Multiple VSGs microgrid

Construction of Lyapunov function for microgrid consisting of n-VSGs is done systematically using Popov multivariable method. It can be used to evaluate the microgrid total transient energy at any operating point. However, evaluating the region of attraction

is a challenging task as it is not confined in a two-dimensional plane as in a single VSG microgrid, which was bounded by two unstable points.

Instead, such a region is found between hyper-planes in n-dimensions. Each hyper-plane is formed by one of the independent unstable equilibrium points of each machine. An example of such a representation is shown in Fig. 3. 21 for a 4-VSG microgrid where the 4th VSG is the reference. This poses a minimization problem that aims at minimizing such a region defined by $v(X)$ and ideally makes it tangential to each hyper-plane [60].

A correct solution to such a problem involves topological theories and convex optimization which are beyond the scope of this study. Sufficient solution for microgrid application is possible through proper approximation based on its physical properties. That is, a microgrid becomes unstable if one VSG at a time loses synchronism, or all of them lose synchronism by reaching their unstable equilibrium points.

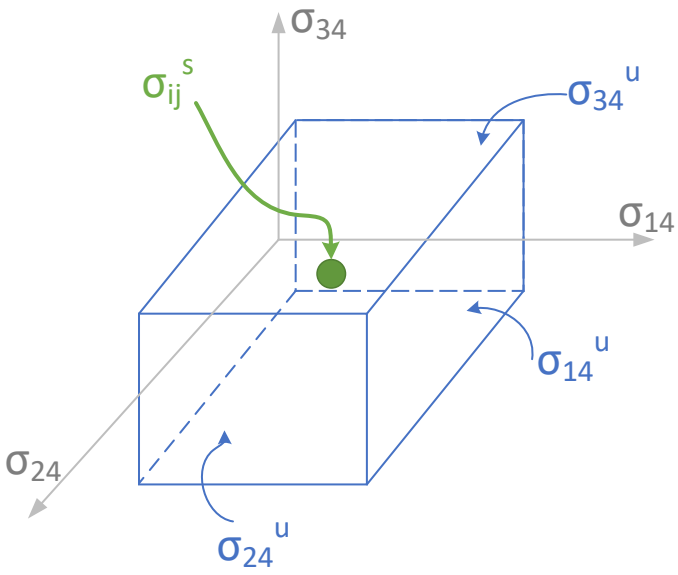

Fig. 3. 21. Hyper-planes represent the unstable equilibrium points in 4-VSG microgrid; Green point is the stable desired operating point in the middle

Therefore, the multivariable Lyapunov function is evaluated under these unstable conditions, and its minimum value sets the upper bound of the region of stability. These points can be summarized as follows [1]:

a) At the unstable points of each VSG alone $(0, \ldots, \pi \pm 2\delta_{in}^{s}, \ldots, 0)$ where, $(i = 1, 2, 3 \ldots n-1)$ is the i^{th} VSG and n is the reference n^{th} VSG.
b) At the unstable points where VSGs become unstable $(\pi \pm 2\delta_{1n}^{s}, \pi \pm 2\delta_{2n}^{s}, \pi \pm 2\delta_{3n}^{s} \ldots, \pi \pm 2\delta_{n-1\to n}^{s})$ where, $(i = 1, 2, 3 \ldots n-1)$ is the i^{th} VSG and n is the reference n^{th} VSG.

3. 4. 3. Case study of multiple VSG microgrid

A case study is carried on using modified 9-bus power system, which is also known as WSCC 3 machine system. It is originally formed by 3 SG machines connected to bus 1, 2, and 3. They are connected to the rest of the rest of the network by 3 two-winding transformers which connect bus 1 to bus-4, bus-2 to bus-7, and bus three to bus-9. The transmission network is modeled using 6 constant impedance transmission lines. The loads are connected to bus-5, 6 and 8 and are modeled as PV loads. Bus-1 is the swing bus of the system. The single line diagram of the network is shown in Fig.3.22 and its parameters are listed in Table 3.2 to 3.5 on base power 100 MV. Here, the network is modified by replacing the SGs by VSGs with output impedance equal to the transient impedance of the original SGs. Their parameters are listed in Table 3.5 on base power of 100 MVA. The load flow calculation results are shown in Fig. 3.25., and the network single line diagram is shown in Fig. 3.24. The rest of the system is remained unchanged.

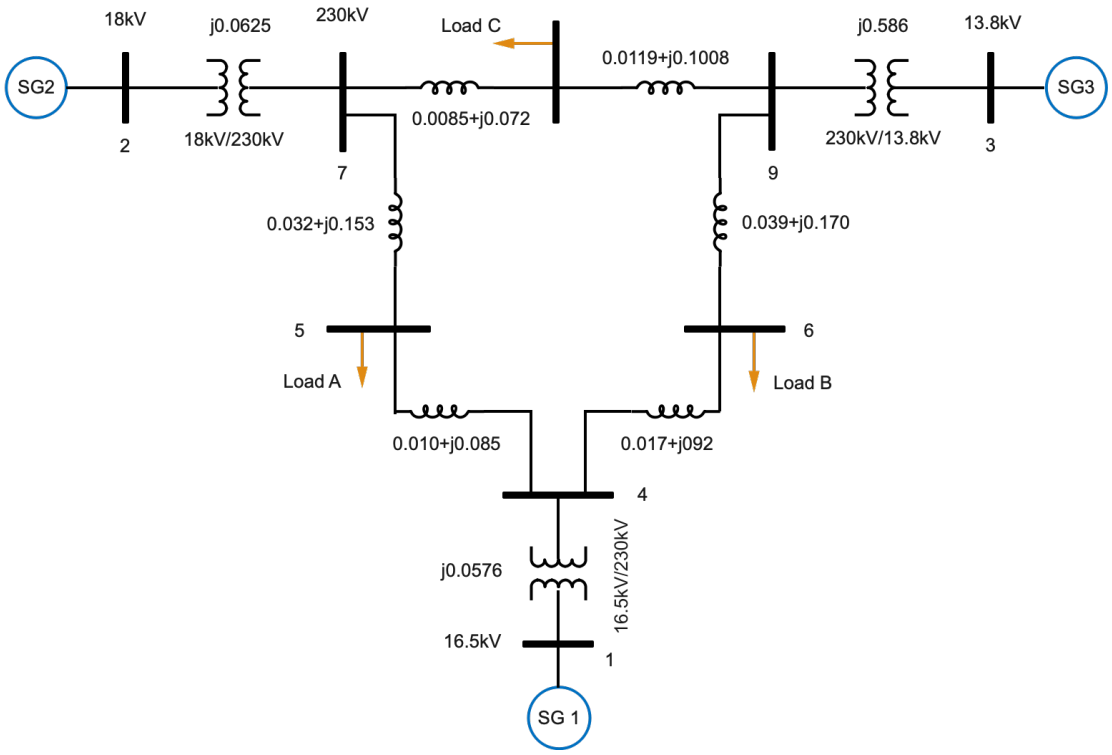

Fig. 3.22. 9-Bus IEEE system (WSCC)

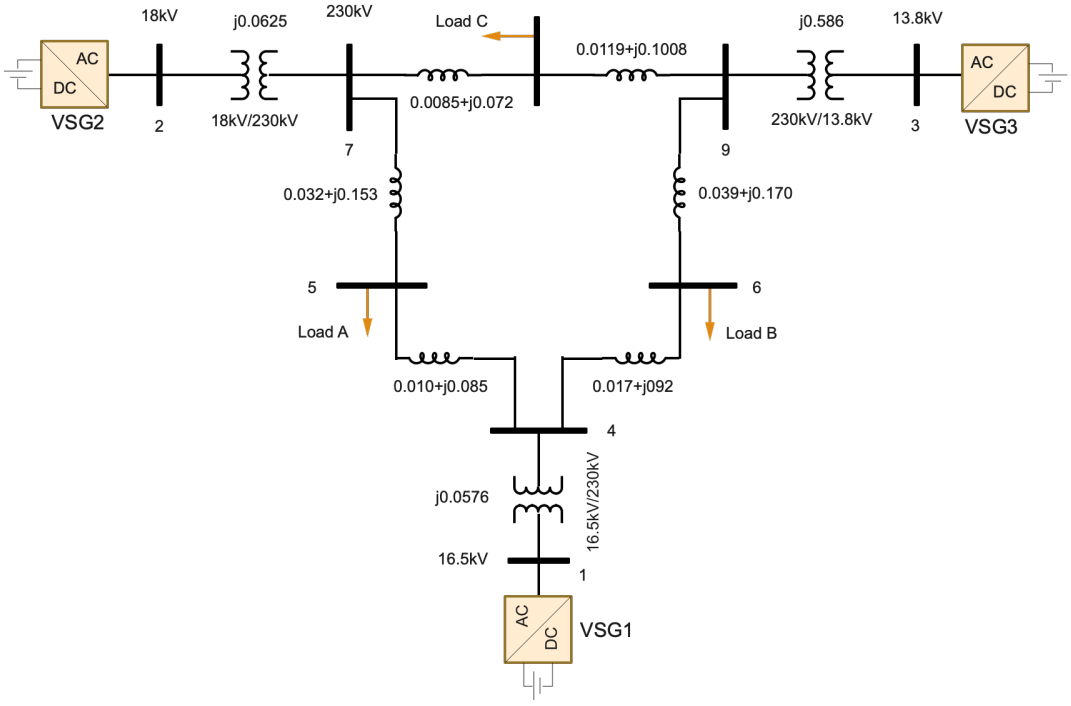

Fig. 3.24. Modified 9-Bus IEEE system (WSCC)

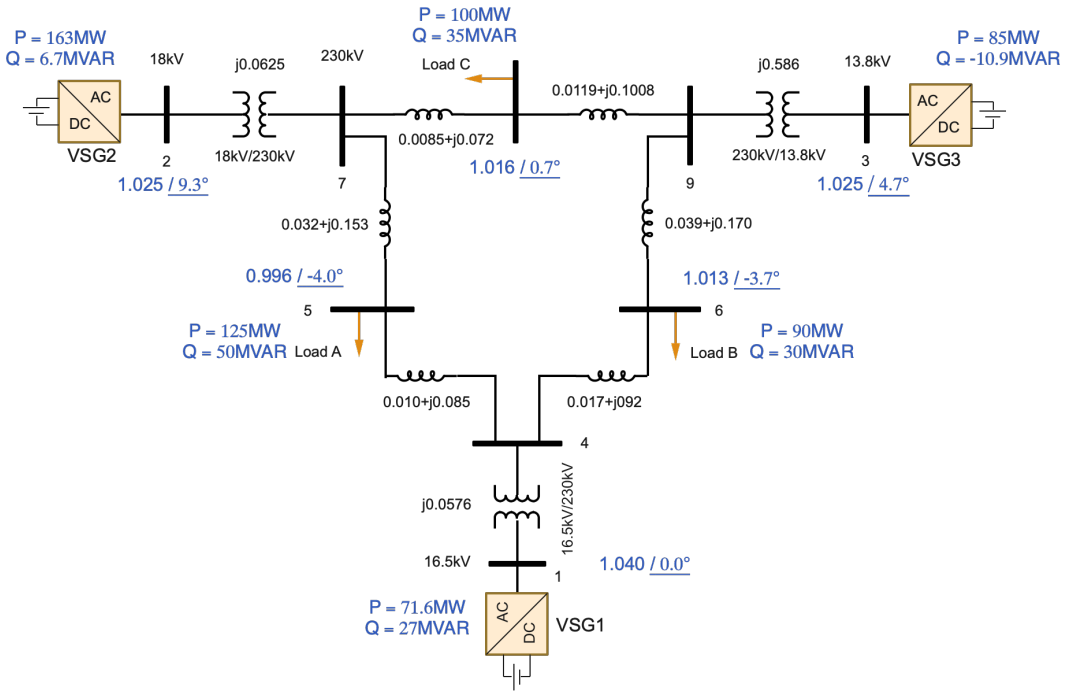

Fig. 3.25. Load flow of the modified 9-Bus IEEE system (WSCC)

Table. 3.2. Transformers parameters

	T1	T2	T3
Nominal primary voltage (kV) RMS L-L	24	18	15.5
Nominal secondary voltage (kV) RMS L-L	230	230	230
R1 p.u.	1.00E-10	1.00E-10	1.00E-10
L1 p.u.	2.88E-02	3.13E-02	2.93E-02
R2 p.u.	1.00E-10	1.00E-10	1.00E-10
L2 p.u.	2.88E-02	3.13E-02	2.93E-02
Rm p.u.	5.00E+03	5.00E+03	5.00E+03
Lm p.u.	5.00E+03	5.00E+03	5.00E+03

Table. 3.3. Transmission limes parameters

Line		R (p.u./m)	X (p.u./m)	B (p.u./m)
From Bus	To Bus			
4	5	0.0100	0.0680	0.1760
4	6	0.0170	0.0920	0.1580
5	7	0.0320	0.1610	0.3060
6	9	0.0390	0.1738	0.3580
7	8	0.0085	0.0576	0.1490
8	9	0.0119	0.1008	0.2090

Table. 3.4. Load parameters

Bus	P (p.u.)	Q (p.u.)
5	1.25	0.50
6	0.90	0.30
8	1.00	0.35

Table. 3.5. VSG parameters

VSG	1	2	3
Rated (MVA)	247.5	192.0	128.0
Output Voltage (kV)	16.5	18.0	13.8
Base Power (MVA)	100	100	100
Output Impedance	0.1460	0.8958	1.3125
Stored Energy (MW's)	2364	640	301
Inertia Coefficient H (s)	23.64	6.4	3.01

The network model is formulated as follows:

$$\frac{2H}{\omega_R}\frac{d\omega}{dt} = D_i\omega_i = P_{mi} - \left[E_i^2 G_{ii} + \sum_{\substack{j=1 \\ j\neq i}}^{n} E_i E_j\, Y_{ij}\, Cos\left(\theta_{ij} - \delta_i + \delta_j\right)\right] \qquad (3.25)$$

$$\frac{d\delta_i}{dt} = \omega_i - \omega_R \qquad i = 1, 2, 3, \ldots, n$$

$$P_{mi0} = \left[E_i^2 G_{ii0} + \sum_{\substack{j=1 \\ j\neq i}}^{n} E_i E_j\, Y_{ij0}\, Cos\left(\theta_{ij0} - \delta_{i0} + \delta_j\right)\right] \qquad (3.26)$$

where,

$$E_1\angle\delta_{10} = 1.0566\ \angle 2.27°$$

$$E_2\angle\delta_{20} = 1.0502\ \angle 19.73°$$

$$E_3\angle\delta_{30} = 1.0170\ \angle 13.18°$$

Table. 3.6. Reduced admittance matrix Y_{ij}

Condition	Node	1	2	3
Pre-fault	1	$0.846 - \mathrm{i}2.988$	$0.287 + \mathrm{i}1.513$	$0.210 + \mathrm{i}1.226$
	2	$0.287 + \mathrm{i}1.513$	$0.420 - \mathrm{i}2.724$	$0.213 + \mathrm{i}1.088$
	3	$0.210 + \mathrm{i}1.226$	$0.213 + \mathrm{i}1.088$	$0.277 - \mathrm{i}2.368$
Fault	1	$0.657 - \mathrm{i}3.816$	$0.000 + \mathrm{i}0.000$	$0.070 + \mathrm{i}0.631$
	2	$0.000 + \mathrm{i}0.000$	$0.000 - \mathrm{i}5.486$	$0.000 + \mathrm{i}0.000$
	3	$0.07 + \mathrm{i}0.631$	$0.000 + \mathrm{i}0.000$	$0.174 - \mathrm{i}2.796$

Lyapunov function is regarded as follows:

$$v(X) = \frac{1}{2}\sum_{i=1}^{n}\sum_{\substack{j=1 \\ j\neq i}}^{n}\frac{M_j}{D_j}M_i\omega_i^2 + \frac{1}{2D_T}\sum_{i=1}^{n}M_i^2\omega_i^2$$

$$+ \frac{1}{2D_T}\sum_{i=1}^{n-1}\sum_{j=i+1}^{n}D_iD_j\left(\delta_i - \delta_i^s + \delta_j^s - \delta_j + \frac{M_i}{D_i}\omega_i - \frac{M_j}{D_j}\omega_j\right)^2 \qquad (3.27)$$

$$+\sum_{i=1}^{n}\frac{M_i}{D_i}\sum_{i=1}^{m}\int_0^{\sigma}f_i(\sigma_i)\,d\sigma_i$$

Lyapunov function is calculated based on the criteria provided in section 3.4.2. to produce the critical energy levels. Each one of them is enough to cause one or more of the VSG to go output of synchronism. As discussed, the minimum energy level 8.06545 p.u. will be considered in determining the network t_{cr}, which is corresponding to energy level required to cause the second VSG2 to go out of stability.

A 3-phase to ground fault is applied at the transmission line 5-7 close to bus-7. The reduced admittance matrix is listed in Table 3.6. The relative power angles of VSG2 $\delta_2(t)$ and VSG3 $\delta_3(t)$with respect to VSG1$\delta_1(t)$ are shown in Fig. 3.27 (a) and the frequency deviations $\omega_1(t)$, $\omega_2(t)$, and $\omega_3(t)$ in Fig. 327 (b). These power angles along with the frequency deviation are fed into the Lyapunov energy function $v(x)$. It has been found that the system reaches its determined critical energy level after $0.28s$. If the fault is removed, the system exhibits damped oscillation and goes back to its steady state stable equilibrium point as shown in Fig. 3.28 (a) and (b). The amount of energy the system gains and gradually releases during the transient is tracked using Lyapunov function and shown in Fig. 3.28 (c). It shows that the system eventually dissipates all its transient energy and eventually restores the balance between its input power and output power. In other words, the system goes back to its initial stable equilibrium point.

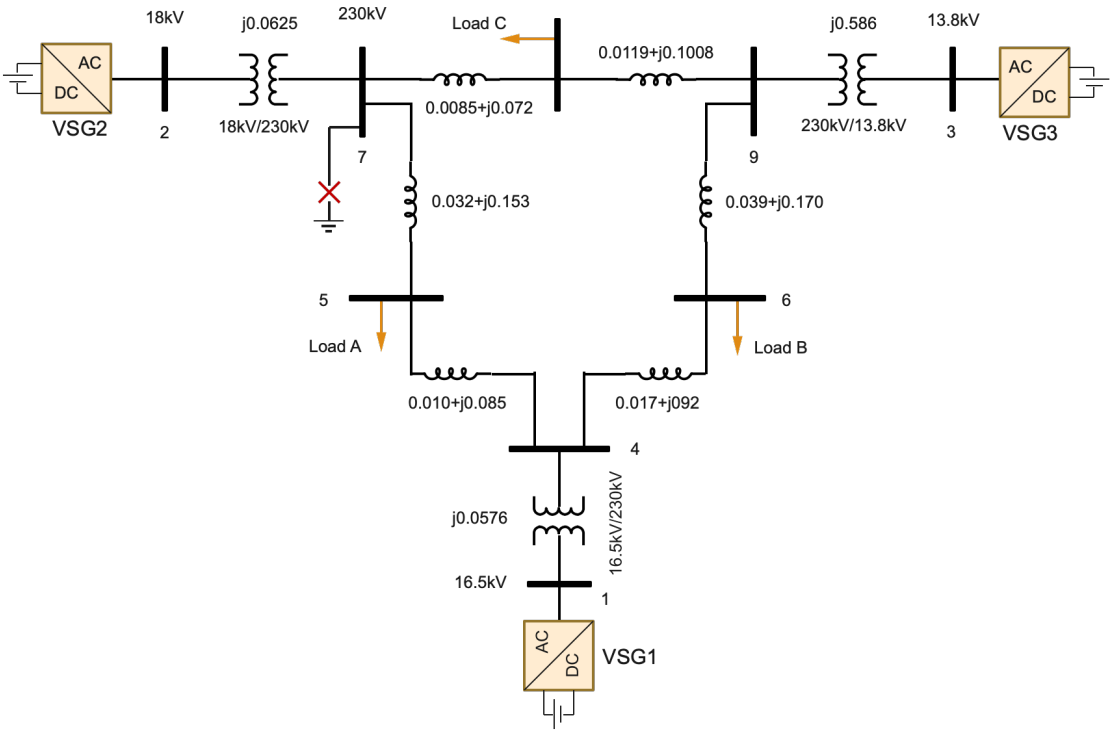

Fig. 3.26. Fault applied at bus 7 in modified 9-Bus IEEE system (WSCC)

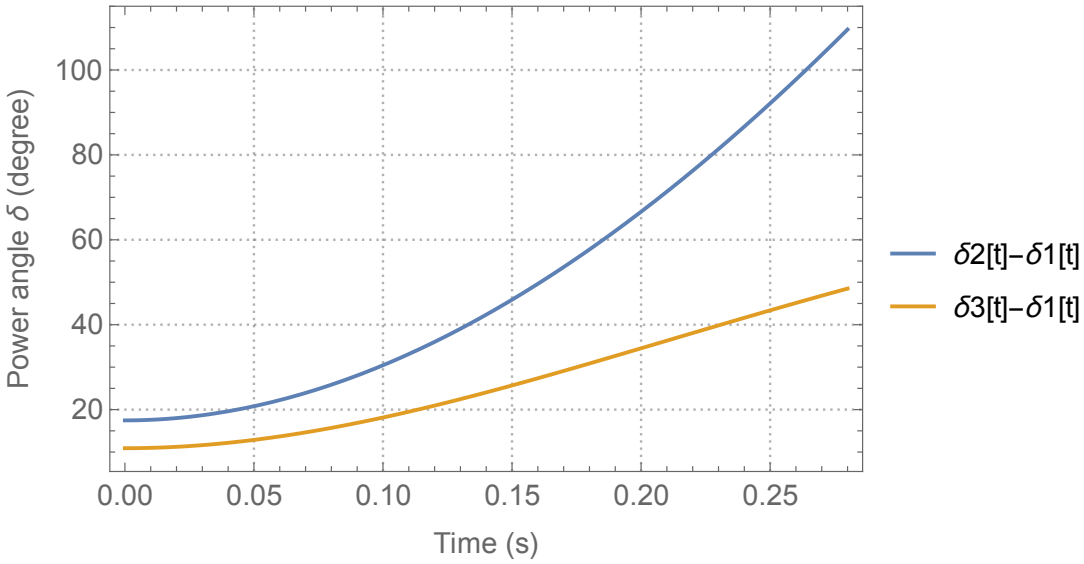

(a)

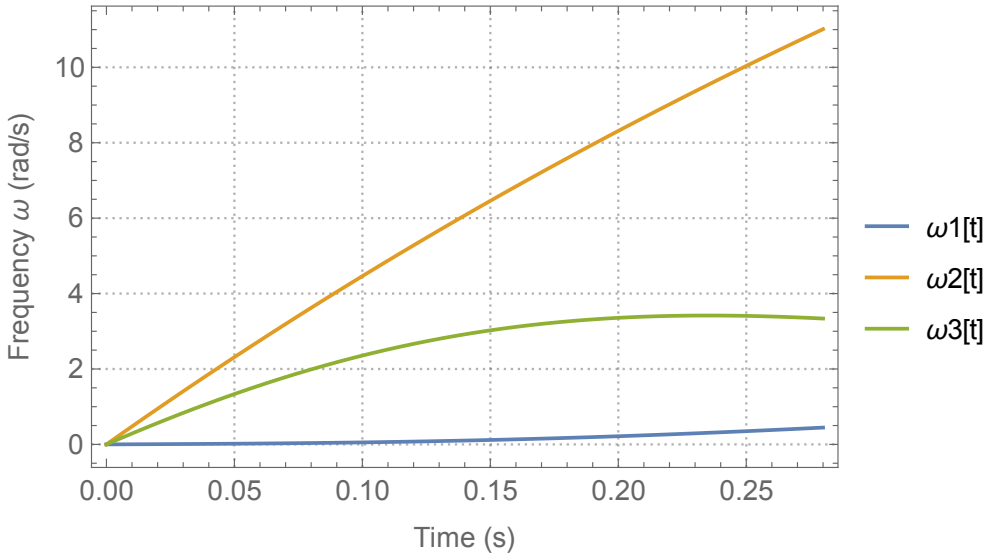

(b)

Fig. 3.27. Faulted system at bus-7; (a) VSG's power angle relative to VSG1; (b) VSG's frequency deviation.

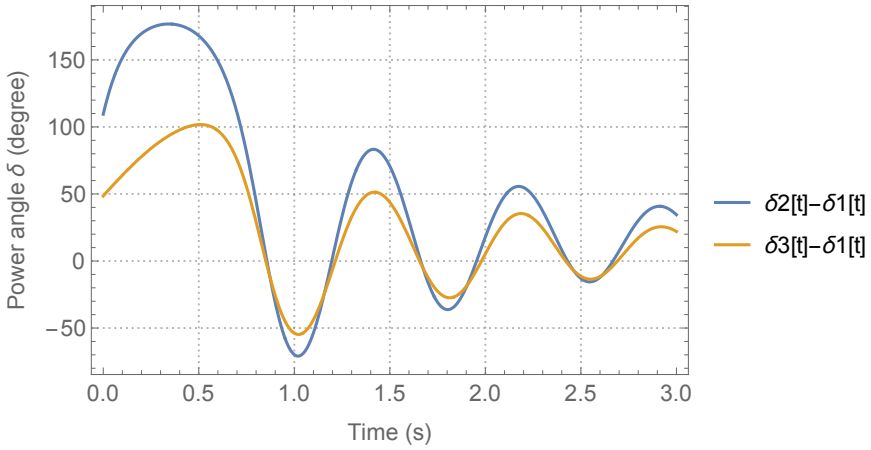

(a)

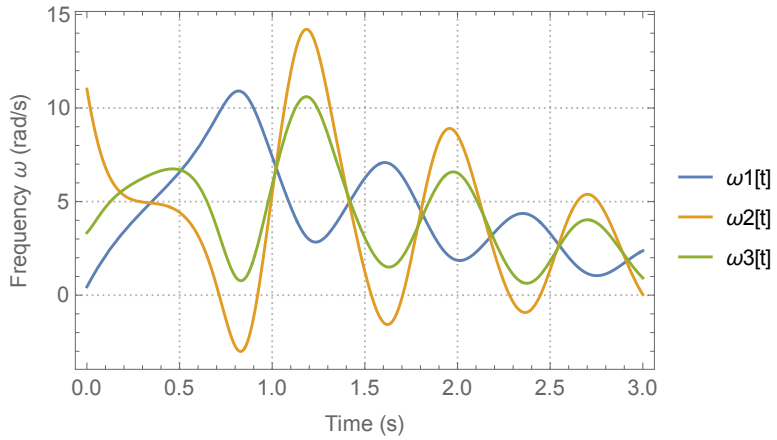

(b)

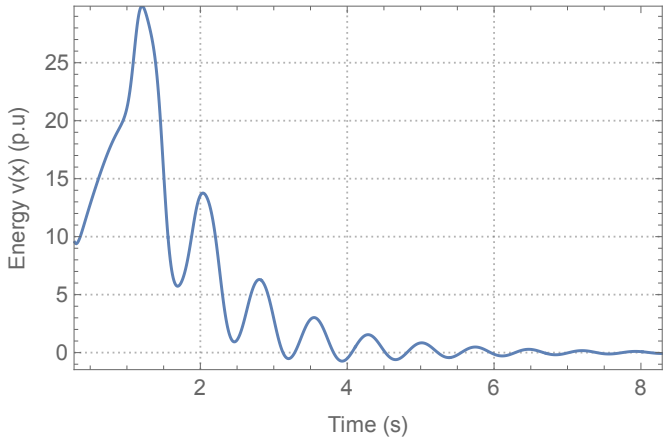

(c)

Fig. 3.28. Post fault, fault is cleared at $t_{cr} = 0.28s$ (system is stable); (a) VSG's power angle relative to VSG1; (b) VSG's frequency deviation; (c) Network energy represented by Lyapunov function.

On the other hand, when the fault is present for more than $0.28s$ for example $0.29s$ the energy the system gains during the fault exceeds the predetermined energy level $v(x)$ and exhibits oscillatory behaviour with increasing amplitude. In other words, All VSGs lose synchromism and system become unstable, as shown in Fig. 3.29 (a) and (b). The amount of energy the increasing system gains during the transient is tracked using Lyapunov function and shown in Fig. 3.29 (c).

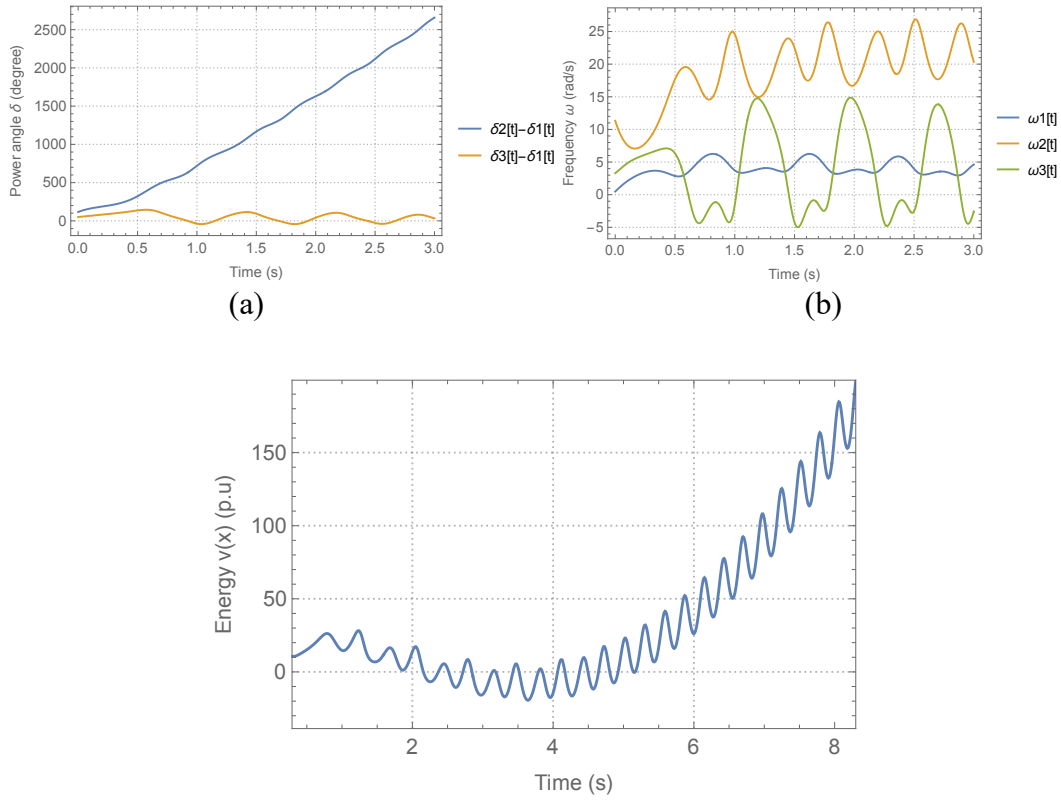

(a) (b)

(c)

Fig. 3.29. Post fault, fault is cleared at $t_{cr} = 0.29s$ (system unstable); (a) VSG's power angle relative to VSG1; (b) VSG's frequency deviation; (c) Network energy represented by Lyapunov function.

4. Trajectory Reversing Based Stability Analysis

4. 1. Introduction

It is a straightforward procedure to determine the fixed points of any given nonlinear system to determine its stability using, for example, Lyapunov indirect method. The challenge comes in answering the question regarding the range of dynamics a system can exhibit starting around its stable point before spiraling out and becoming unstable. Such point(s) are known as points of asymptotic stability and such a region around them is known as the region of asymptotic stability or region of attaction (ROA). Many techniques have been introduced in the literature that rely on finding a proper Lyapunov function. Although it is a simple concept in abstract, it is often hard to achieve and lacks the appeal of a systematic construction in engineering applications [49] [48].

One of the approaches to such a problem is based on the Zupov's function. It provides the necessary and sufficient conditions for a given region around a fixed stable point, by formulating partial differential equations in each Lyapunov function. Although the resultant function perfectly defines ROA, most of the times a closed-form solution does not exist. A work around this is to use an approximation method to generate an adequate subset of the original ROA. Such approximating techniques are presented in [49]. A series expansion technique-based approximation is presented in [61], [62] and a numerical approximation is presented in [63]. Moreover, an approximate solution of the Zupov's function using the Lie series is introduced in [64], [8], [9], and a Lagrange-Charpit based approximation is available in [65].

Another approach to estimate ROA is based on La Salle's theory [66]. It gives some conditions to the time derivative of the Lyapunov function for certain regions to be included in the estimated ROA. However, it is found to give a more limited estimation as compared with Zupov's method. Generally, these methods can be split into two main categories:

1. The first one is applied to well defined nonlinear systems. Initially, the Lyapunov function is constructed for low-order systems using any of the classical procedures e.g., quadratic or Lure's LF's, Igwerson, variable gradient, Krasovskii, which satisfy La Salle's theory. Then, an optimization algorithm is applied to maximize the ROA subset

as much as possible [67]. In [68], for example, a quadratic Lyapunov function maximizing the subset ROA with respect to its coefficient is implemented. First, it uses a numerical algorithm to define a norm Lyapunov function and then enlarges it. A similar approach is introduced in [69]. It is based on a frequency criteria and topological considerations to predict the existence of limit cycles. It is worth mentioning that these types of methods are well established and used in power system stability analysis [60].

2. The second category of methods is based on frequency domain Popov's criterion which generally considers Lyapunov function and holds for nonlinear systems that comply with the sector conditions (first and third quadrants) based on Aizerman's definition. This concept is extended to higher dimension nonlinear systems in [41] (as in a multi-machine power system). These methods, especially the latter two, are specifically developed for power system stability studies where it is easy to prove its compliance to passivity theorem and sector conditions.

This work proposes the utilization of a convex hull-based trajectory reversing method to estimate and enlarge the ROA of a grid connected VSG. That is, a family of trajectories initiated close to the VSG equilibrium point is generated and evaluated at successive time steps. After each evaluation, the resultant points are passed to the convex hull algorithm that finds the minimum region that contains all these points. Such a region is a subset of the VSG's ROA. Repeating these steps leads to enlarging the VSG's estimated ROA. Nonetheless, finding an exact estimation of the VSG's ROA requires significantly high number of trajectories (with their initial points) and high number of time steps which will have negative impact on the algorithm computational time. This work proposes a new technique to define the set of initial points needed by the algorithm. The proposed technique provides an easily tuneable method that balances the computational time with the number of initial points and their corresponding trajectories. It ensures a uniform distribution of the initial points over the ROA regardless of how many points are needed. Hence, the number of initial points can be reduced without compromising the process. The proposed technique is more beneficial in a system with higher dimension's i.e., with n number of VSGs, where finding uniformly distributed initial points around the equilibrium point of each machine is a challenge.

4. 2. Trajectory reversing method

For a nonlinear system:

$$\dot{X} = F(x) \tag{4.1}$$

where,

$x = x(t) \in \mathbb{R}^n$ and $F(x)$ satisfies the existence and uniqueness conditions for all solutions $x(t, t_o)$ which have initial conditions $x(0) = x_o$, and its origin is such that:

$$F(0) = 0 \tag{4.2}$$

and it is an asymptotically stable isolated fixed point (equilibrium point).

Nonetheless, such a system can have other fixed points such that:

$$F(x) = 0 \tag{4.3}$$

The region of asymptotic stability ROA around the fixed point at the origin is defined as the set Ω of all initial condition points x_o which are functions of the time t and initial time $t_o$such that

$$\Omega = \lim_{t \to \infty} x(t, t_o) = 0 \tag{4.4}$$

It is worth mentioning that Ω is an invariant set with $d\Omega$ as is its boundary. That is, if the system started with initial conditions (e.g., $\Delta\omega_o$ and θ_o) it must follow the corresponding trajectory and end up at the origin. The backward integration of such a system is equivalent to:

$$\dot{X} = -F(x) \tag{4.5}$$

The magnitudes of the derivatives are equivalent to the original system, but in the opposite direction. This can be observed in system's phase portrait where the arrows direction is reversed. Hence, the origin $F(0) = 0$ becomes unstable and has repulsive trajectories. After sufficient time t, such trajectories will form the boundary set $d\Omega_{\mathrm{ROA}}$ which is less than or equivalent to the original boundaries $d\Omega$.

This technique is more efficient in low order systems. It can provide almost an exact ROA in second order systems. It has been reported in [70] that such a technique is not

computationally efficient in third and higher order systems. Therefore, convex hull algorithm is introduced in [56] to extend it to higher dimensions.

4. 3. Estimation of ROA using Convex Hull Algorithm

4. 3. 1. Background

Reverse trajectory states that it is possible to estimate a system's ROA from enough initial points. Nonetheless, the work first introduced in [70] admits that it is a rather complex process to extend this work beyond 3D e.g., more than one VSG. Here, an algorithm to obtain an estimation and enlargement of the converter's ROA based on convex hull is discussed. It relies on determining whether a given set of points lie within a given convex hull [70], [56].

The objective of finding the convex hull is to define the smallest convex set (region) such that contains all points in $s = \{x_1, x_2, x_3, \dots x_n\}$ in $\mathbb{R}^n$ [71]. Such a convex set is described by a finite number of inequalities and equations. In the 2-D plane, it can be represented by line segments that are defined by their equations while their perspective length is defined by inequalities. In cases of higher dimensions, convex hull is defined by hyperplanes and inequalities.

The convex hull is constructed using Mathematica's embedded function *ConvexHullMesh* for theoretical calculations, and a similar Matlab function *quick hull* exists in the simulation.

The algorithm introduced in [56] is utilized here to serve this purpose. It uses the Matlab function *inhull* to perform this check-up. Mathematica's *RegionMember* function also provides a robust and easy way to do the same task. These functions first, select random points x_i on each simplex e.g., hyperplanes that define the convex hull. Then, a testing point x_t is located inside the convex hull, if and only if, the inner product of it is inward facing normal n_i and the distance between the testing point and the randomly selected points is positive.

For,

$$Q_i = x_t - x_i \tag{4.6}$$

And $i = 1, 2, 3, \ldots$

The point x_t is inside the convex hull if and only if,

$$n_i \,.\, Q_i \; > \; 0 \tag{4.7}$$

for every i^{th} point on convex hull hyperplane.

Furthermore, the algorithm also requires that all the vertices of the constructed convex hull form a single cluster around the origin. In other words, it means it is density reachable [72] for any arbitrary distance ε.

In some applications, a subset of the convex hull is sufficient to describe the ROA of interest. For example, in a power system where periodic repeated stable points are existing, only the ROA bounded by the power angle of each machine / VSG from -2π to 2π is acceptable. Further constrains can be imposed based on the desired characteristics inside the ROA. The Matlab function *intersectionhull* [12] can be used to slice the convex hull to satisfy the constraints on the enlarged ROA.

4. 3. 2. Convex representation of ROA using the trajectory reversing method

Estimation of the enlarged region of asymptotic stability (ROA) in a power system can be done as follows:

1. The VSG / machine's stable equilibrium points are determined. This is done by dropping the derivative terms and equating the grid model (swing equation) to zero and calculating δ_{i0}^s and ω_{i0}^s. In a single VSG connected to an infinite bus network, δ_{i0}^s and ω_{i0}^s become δ_0^s and ω_0^s. Due to the periodic nature of the grid model and prior knowledge of the application and operation requirement, only positive power angle δ_{i0}^s may be considered.

2. Select a discrete number of initial points n sufficiently distanced from the given equilibrium point (δ_0^s , ω_0^s) such that:

$$X_o = \{x_1, x_2, x_3, \ldots . x_n\} \tag{4.8}$$

where,

$x_n = \left(\delta_{o_n}, \omega_{o_n}\right)$ and $n \in \mathbb{N}$ is the number of the initial points.

These points must be located inside of the initial conservative estimation of the ROA. In other words, it must be within the asymptotic region as discussed in the previous section. A systematic and robust method to select the proper initial points is proposed in the next section. This process must be repeated for each equilibrium point of each VSG / machine.

3. Starting from each initial point $x_n = (\delta_{o_n}, \omega_{o_n})$, the model is numerically integrated in reversed time starting from $t = [0, t_o]$. The integration is repeated, and the time-period is increased with every repetition, such that $t = [0,\ t_o + k\Delta t]$. The resultant integrations are evaluated at $t = k\Delta t$ and the following set formed:

$$X_{k\Delta t} = \left\{x_{1_{k\Delta t}}, x_{2_{k\Delta t}}, x_{3_{k\Delta t}}, \ldots . x_{n_{k\Delta t}}\right\} \tag{4.9}$$

The values of n and Δt should be selected to balance the estimation accuracy and computation time. In a power system, it is sufficient to set $\Delta t = 1/f$ where f is the grid nominal frequency in Hertz (typically 60 Hz). Selection of n is discussed in detail in the following section.

4. The convex hull is constructed for the evaluated set $X_{k\Delta t}$ for every $k \in \mathbb{N}$ using Matlab *convhull* function (or Mathematica).

5. Step (3) is repeated. The resultant points in the set $X_{k\Delta t}$ are checked to determine their location inside / outside the convex hull constructed in step (4) using Matlab's *inhull* function / Mathematica's *RegionMember* function. Convex hull represents the enlarged ROA if all the points in $X_{k\Delta t}$ lie within the constructed convex hull. Otherwise, step (4) is repeated, and a new convex hull is constructed using the new $X_{k\Delta t}$.

Steps (3) and (4) are repeated as many times as needed to achieve a precise estimation of the ROA. The algorithm is summarized in the flow chart shown in Fig. 4.1. The general idea

is to define initial points, integrate the model in reverse time, use the end points of each integral curve, construct a convex hull, and then repeat the integration for a longer time. If all the end points of the curves in longer time are within the convex hull, the enlarged ROA is found. Otherwise, the new end points are used to construct a new convex hull, and the steps are repeated.

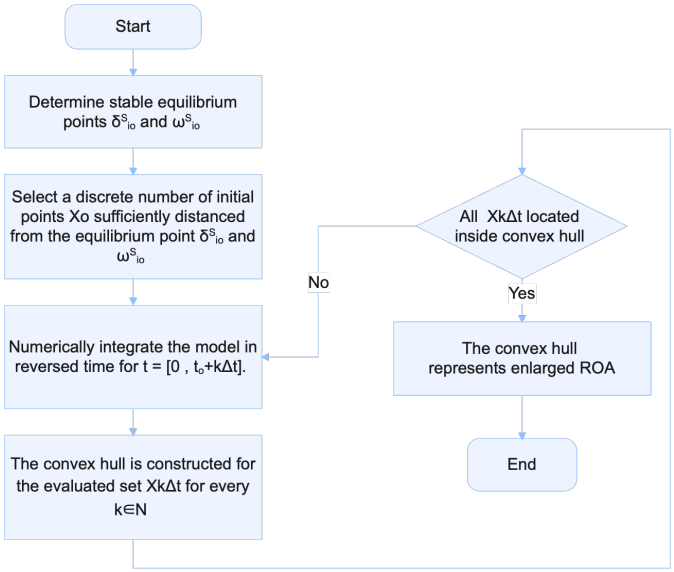

Fig. 4.1. Algorithm's flow chart

4. 3. 3. Solving initial condition problem

Single VSG system

The algorithm introduced in [56] is effective in enlarging the estimated ROA of a given system. However, it did not define how these initial points are chosen. This can be problematic in power electronics and power system applications, where an arbitrary selection of initial points can result in inadequate estimation of the ROA. A small perturbation around the stable equilibrium point is possible in a two-dimensional system e.g., VSG converter connected to a utility grid. Nonetheless, in power electronics and power system applications, if these points aren't uniformly distributed around the stable equilibrium point and concentrated in one side more than the other, a poor estimation of the ROA will occur, and an enlargement of the ROA will not be possible. Moreover, it is not as

clear in complex higher dimension systems e.g., with 9 VSG converters connected into a microgrid.

Here, a direct systematic method is proposed for choosing such initial points. This method ensures the following:

- Direct systematic way to select the initial points used in the backward integration to generate the reversed trajectories.
- Uniform distribution of these points around the stable equilibrium point(s). Hence, enables enlargement of the estimated ROA.
- Enables a trade-off between better enlargement of the estimated ROA and the computation time required. Fewer points (hence, trajectories) can be considered without loss of the uniform distribution to reduce the required computational time.

For a grid-connected VSG converter (i.e., two-dimension system), with stable equilibrium point $x^s = (\delta^s, \omega^s)$. The proposed method for choosing the initial points ($\delta_{o,i}$, $\omega_{o,k}$) defines them according to the following equation:

$$\delta_{o,k} = \delta^s + \varepsilon_\delta \, Cos\left(\frac{2\,k\,\pi}{n}\right) \tag{4.10}$$

$$\omega_{o,k} = \omega^s + \varepsilon_\omega \, Sin\left(\frac{2\,k\,\pi}{n}\right) \tag{4.11}$$

where,

$(\delta_{o,i}, \omega_{o,k})$ is the kth initial point,

(δ^s, ω^s) is the stable equilibrium point,

$k = 1, 2, \ldots n$

and n is the number of initial points. It can be selected to be between 10 to 20 points. It can be higher for more accurate results or lower for computational efficiency.

ε_δ and $\varepsilon_\omega = \varepsilon$ is the small perturbation around the stable equilibrium point. It can be selected arbitrarily small, e.g., 0.001. Its maximum value is limited by the length of the vector that starts from this equilibrium point to the nearest unstable equilibrium point. In a grid connected VSG converter $\varepsilon_{\delta_{max}} < \delta^u - \delta^s$ and $\varepsilon_{\omega_{max}} < \omega^u - \omega^s$.

Fig.4.2 (a) and (b) show the cases where 10 and 20 initial points are chosen around the equilibrium point $\delta^s = 0.848$. ε_ω is set to 50 and ε_δ is set to 1 to generate an exaggerated plot of these initial points to help better demonstrate the idea.

The trajectory reversing process can be followed now using these initial points, where the VSG model is backwardly numerically integrated (in reverse time) starting from the proposed initial points. The resultant reverse trajectories are shown in Fig. 4.3.

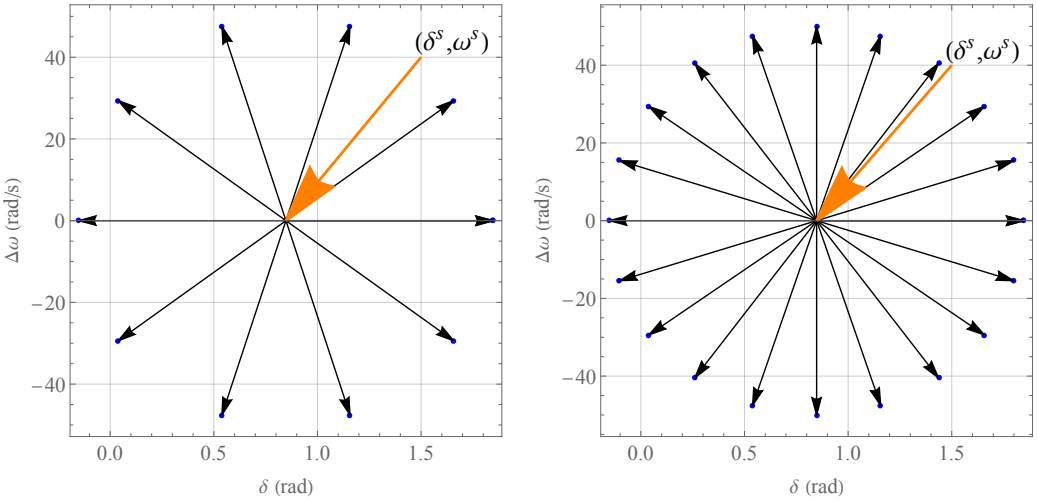

(a) (b)

Fig. 4.2. Initial points distribution (a) 10 points (b) 20 points.

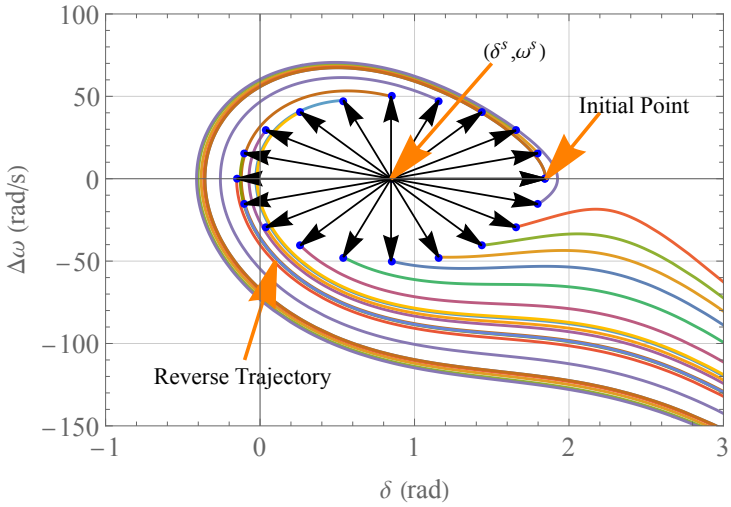

Fig. 4.3. Family of trajectories initiated from the proposed initial points.

Multi-VSG system

In MG, where many VSG converters are connected at different locations, choosing trajectory reversing initial points becomes a cumbersome process. The notion of doing a small perturbation ε around the stable equilibrium points covers partially the state space of the MG dynamics in the form of plane or hyper-plane. For example, the dimension of the state space of an MG with only 4 VSG converters is 8, which makes assigning uniformly distributed initial points a challenging task, unlike the case of 2-dimensional or 3-dimensional space. Furthermore, as this study and stability investigation targets the area of power electronics and power system applications and aims at systematically enlarging the ROA to better calculate MG critical clearing time for different types of faults. It is important to be able to change systematically the number of initial points to balance the results accuracy versus the computational time without sacrificing the uniformity of the distribution of the initial points. The proposed method comes to address these challenges, by assigning the initial points on a surface of a multi-dimensional sphere centered around each equilibrium point. The equations and process are first introduced for a generic 3-dimensional system to provide visual intuition. Later the generalized equations and process are introduced.

For 3-dimensional system with state variable x_1, x_2, and x_3 and equilibrium point at the origin. The 3D unit sphere shown in Fig. 4.4 can be constructed around the origin using the polar parametrization as follows:

$$x_1 = Sin\ (\theta)Sin(\phi)$$

$$x_2 = Cos\ (\theta)Sin(\phi)$$

$$x_3 = Cos(\phi) \tag{4.12}$$

Where, θ and ϕ are two arbitrary angles in $[0\ , 2\pi]$.

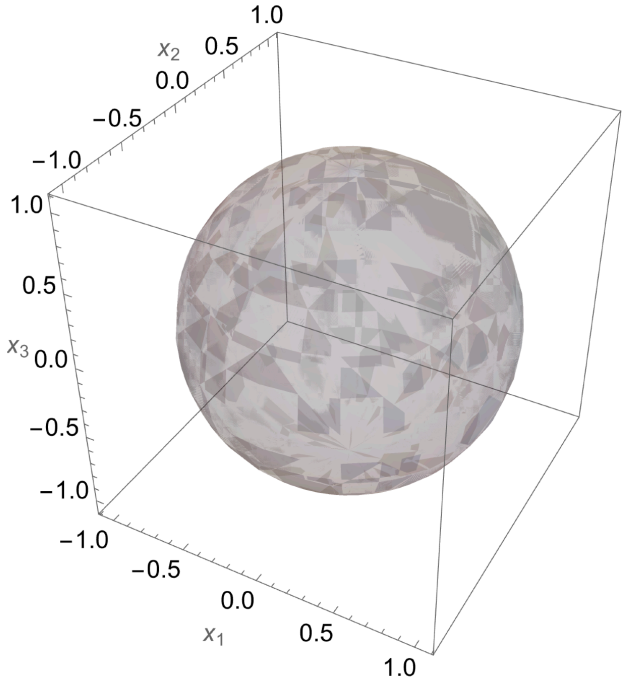

Fig. 4.4. 3D unit sphere

The set Ω_o that contains the initial points equally distributed on its surface can be defined as follows:

$$x_1 = Sin\ \left(\frac{2\ \pi\ k_1}{n}\right) Sin\left(\phi \frac{2\ \pi\ k_2}{n}\right)$$

$$x_2 = Cos\left(\frac{2\,\pi\,k_1}{n}\right) Sin\left(\frac{2\,\pi\,k_2}{n}\right)$$

$$x_3 = Cos\left(\frac{2\,\pi\,k_2}{n}\right) \tag{4.13}$$

Where,

$k_1 and\ k_2 = 0, 1, 2, \ldots n$ and n is a variable that controls the desired number of initial points. Fig. 4.5 shows an example of the resultant points on the sphere.

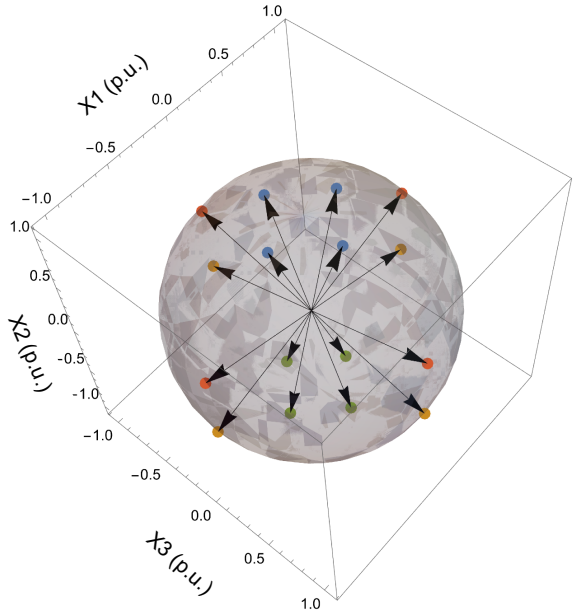

Fig. 4.5. Example of uniformly distributed points on a 3D unit sphere

It is worth mentioning that higher degree of uniformity in the point distribution is achieved when n is set to be an even number. Fig. 4.6. (a) and (b) shows an example of the resultant points on the unit sphere for $n = 5$ and $n = 6$, respectively. Moreover, it is considering a good practice to check the generated points to remove any duplication which can be a result of the oscillatory nature of the trigonometry equations. The number of generated points from equation 4.13 equals to n^2. However, when the duplicated points are removed the final number of points become much lower. Fig. 4.7. shows a comparison between the original number of generate points (n^2) and their number without duplications. The approximate number of reduced points (unique points) can be expressed as follows:

$$Number\ of\ points\ =\ 0.5n^2 - n + 2 \tag{4.14}$$

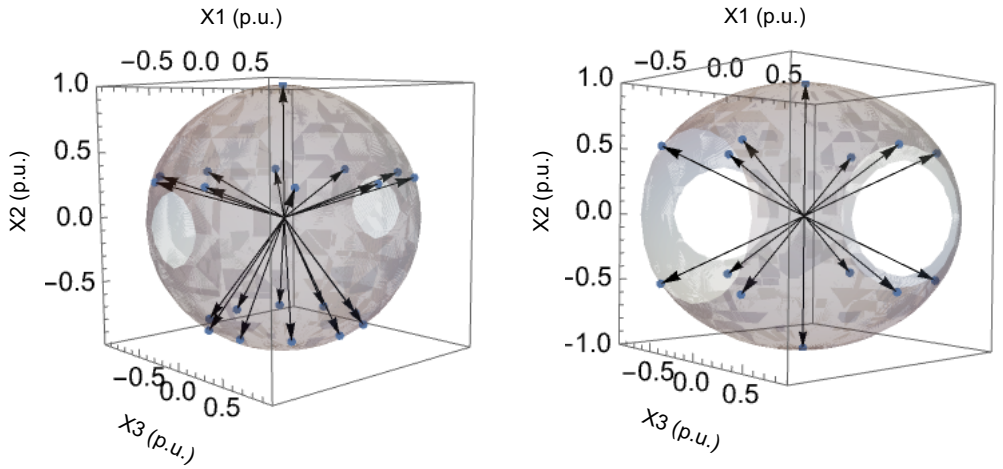

(a) (b)

Fig. 4.6. Example of the resultant points on the unit sphere; (a) $n = 5$; (b) $n = 6$

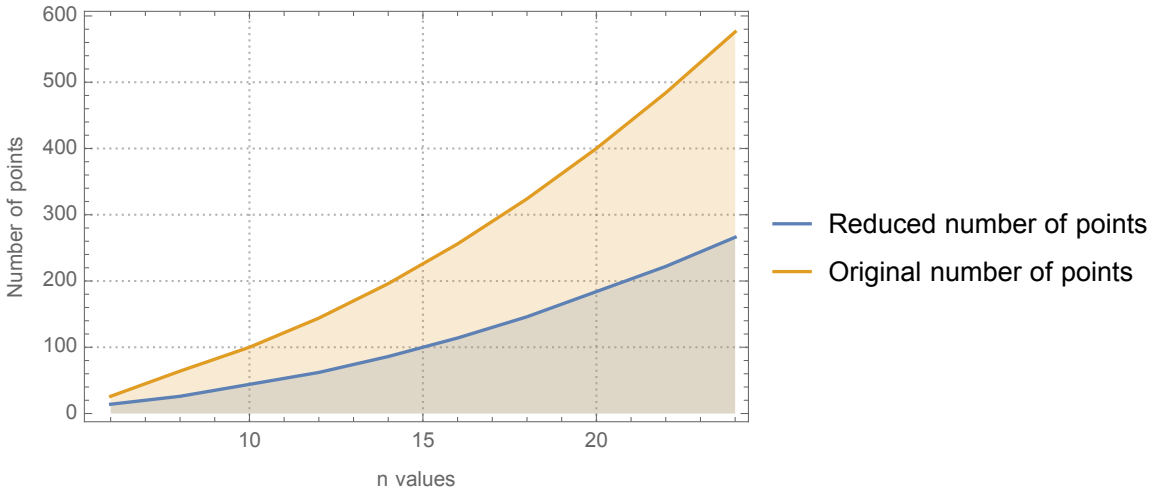

Fig. 4.7. Plot of the original number of generate points (n^2) and the reduced one.

The generalization of the above approach for MG with n-VSG is formulated in equation 4.15 as follows:

Assuming the origin is the system stable equilibrium point, then,

$$\delta_{1,o,k} = \varepsilon \cos\left(\frac{2\,\pi\,k_1}{n}\right)$$

$$\omega_{1,o,k} = \varepsilon \sin\left(\frac{2\,\pi\,k_1}{n}\right) \cos\left(\frac{2\,\pi\,k_2}{n}\right)$$

$$\delta_{2,o,k} = \varepsilon \sin\left(\frac{2\,\pi\,k_1}{n}\right) \sin\left(\frac{2\,\pi\,k_2}{n}\right) \cos\left(\frac{2\,\pi\,k_3}{n}\right)$$

…..

$$\delta_{N,o,k} = \varepsilon \sin\left(\frac{2\,\pi\,k_1}{n}\right) \sin\left(\frac{2\,\pi\,k_2}{n}\right) \cos\left(\frac{2\,\pi\,k_3}{n}\right) \ldots \sin\left(\frac{2\,\pi\,k_{N-2}}{n}\right) \cos\left(\frac{2\,\pi\,k_{N-1}}{n}\right)$$

$$\omega_{N,o,k} = \varepsilon \sin\left(\frac{2\,\pi\,k_1}{n}\right) \sin\left(\frac{2\,\pi\,k_2}{n}\right) \cos\left(\frac{2\,\pi\,k_3}{n}\right) \ldots \sin\left(\frac{2\,\pi\,k_{N-2}}{n}\right) \sin\left(\frac{2\,\pi\,k_{N-1}}{n}\right) \quad (4.15)$$

where,

($\delta_{i,o,k}$, $\omega_{i,o,k}$, …., $\delta_{N,o,k}$, $\omega_{N,o,k}$) is the kth initial point of the N VSG in the MG, and ε is the small perturbation around the stable equilibrium point (the origin).

k_1 to k_N are arbitrary even numbers $= 2, 4, 6, 8, \ldots, n$, while n is a variable that controls the desired number of initial points.

4. 3. 4. Case study

The following is a case study of a grid connected VSG. Consider the network shown in Fig. 4.8. A VSG is connected to an infinite bus by a step-up transformer and double circuit transmission line. System parameters are listed in Table 4.1.

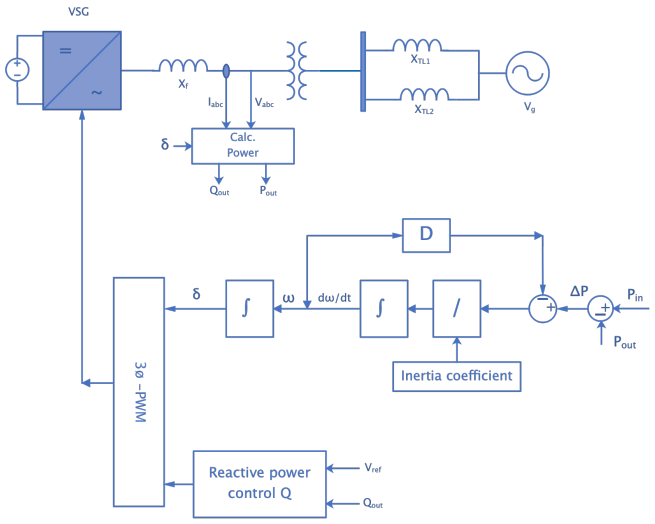

Fig. 4.8. Block diagram of VSG connected to infinite bus.

Table 4.1. VSG parameters

Parameter	Value
Virtual input reference power P_m	0.8 p. u.
Base power S	100 MVA
Grid line voltage v_g	13.8 kV
Power angle at steady state δ	0.4070rad
Grid power angle δ_g	0 rad
Total Line impedance	j0.5 p. u.
Infinite bus voltage v_g	1 p. u.
VSG voltage v_g	1.05 p. u.
Damping constant D	0.1
Inertial Constant M	5 s
Simulation step time	10 us

The system model can be formulated as follows:

$$\dot{\delta} = \omega$$

$$\dot{\omega} = \frac{1}{M}(0.8 - 2.10\sin(\delta + \delta^s) - \mathrm{D}\,\omega) \tag{4.16}$$

Its stable equilibrium point is:

$$x^s = (\delta^s, \omega^s) = (0.4070, 0) \tag{4.17}$$

The trajectory reversing initial points are calculated according to the proposed method, as follows:

$$(\delta_{o,k}\ , \omega_{o,k})$$

For, $n = 100\ \ k = 1, 2, 3, \ldots\ n\ \ \ \varepsilon_\delta = 2\ rad\ \ \ \varepsilon_\omega = 5\ rad\ /s$

Then, the members of the set of the initial points Ω_o is defined as follows:

$$\delta_{o,k} = 0.4070 + 2\ Cos\left(\frac{2\ k\ \pi}{100}\right) \tag{4.18}$$

$$\omega_{o,k} = 0 + 4\ Sin\left(\frac{2\ k\ \pi}{100}\right) \tag{4.19}$$

For $k = 1,2,3, \ldots n$

These points are plotted in Fig. 4.9.

The solution points of the backward integration using the numerical integration algorithm e.g., Runge-Kutta at time steps Δt is shown in Fig. 10. These initial points are sufficient to cover and enlarge the estimated ROA. Finally, the convex hull algorithm can be used to compile a mathematical expression of the enlarged ROA using the solution points generated, as shown in Fig. 4.11 and Fig. 4.12.

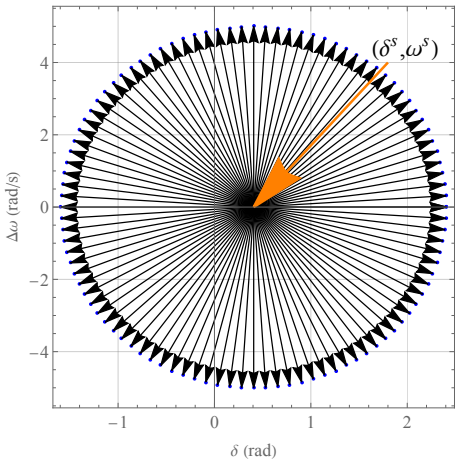

Fig. 4.9. Initial points of the VSG generated by the proposed method.

Convex hull algorithm is applied as explained to the resultant points at each successive time step Δt. The process is halted once the points are no longer outside the convex hull or it is outside the range of interest, i.e., it is corresponding to $\Delta\omega > 50\,rad/s$ which is not acceptable practically. The resultant enlarged ROA is shown in Fig. 4.10 and Fig. 4.11.

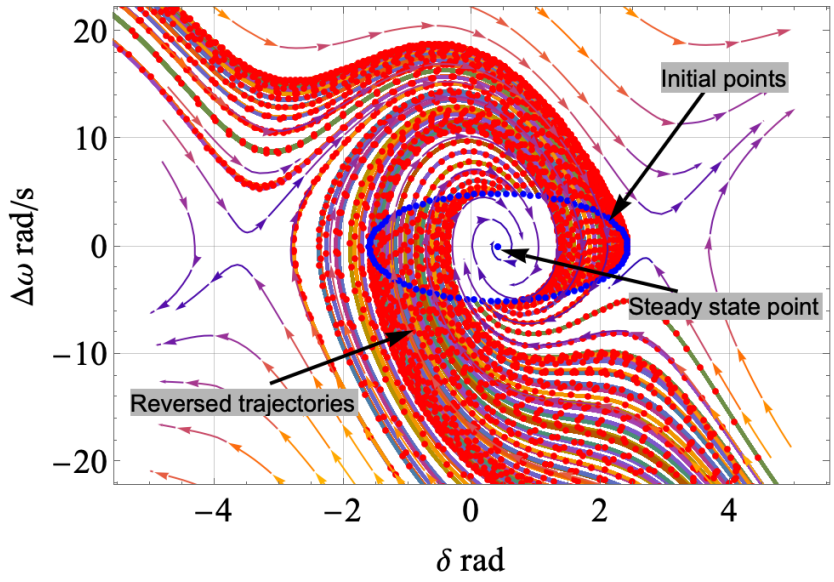

Fig. 4.10. VSG reverse trajectories at each successive time step Δt.

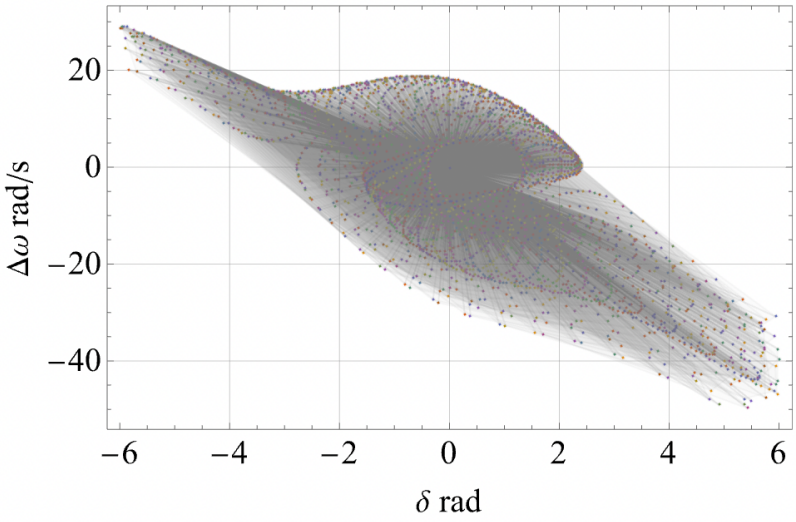

Fig. 4.11. Convex hull set that contains the reversed trajectoies.

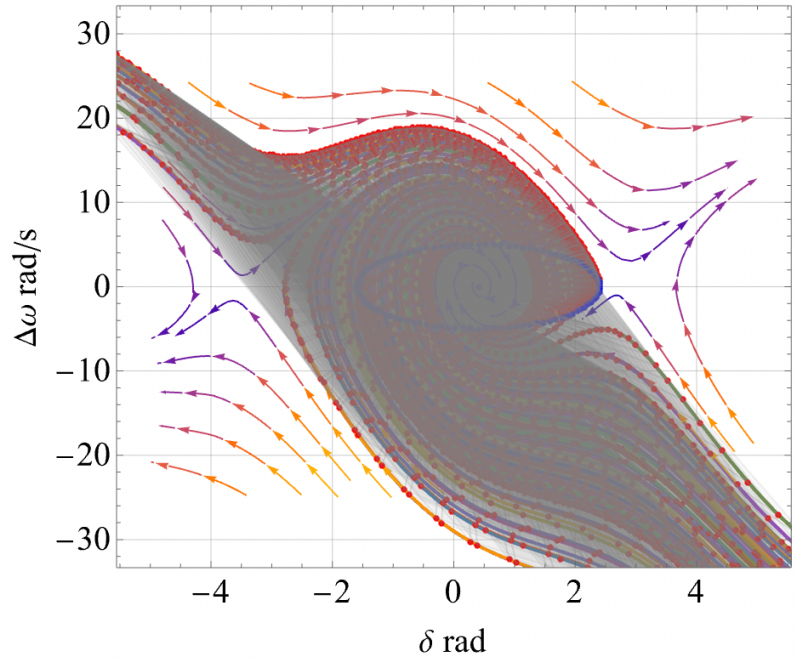

Fig. 4.12. Reversed trajectories and convex hull plotted against system vector field.

Now, the convex hull set can be used to determine the critical clearing t_{cr}. The core idea is to check the VSG $\delta - \omega$ trajectory at successive time steps $\sum_{k=1}^{n} k\Delta t$ with respect to the convex hull set using the *inhull* function. The VSG is expected to come back to its pre-fault

stable equilibrium point $x^s = (\delta^s, \omega^s) = (0.4070, 0)$ if its trajectory is contained within the convex hull set. Otherwise, the converter will become unstable post-fault and resynchronization process to the infinite bus must be initiated. The maximum time $n\Delta t$ a given fault trajectory takes to reach one edge of the convex hull set (enlarged ROA) is the VSG's critical clearing time.

For the system shown in Fig. 4.8, an open circuit fault is applied in the VSG output. The faulted system model is formulated as follows:

$$\dot{\delta} = \omega$$

$$\dot{\omega} = \frac{1}{M}(0.8 - \mathrm{D}\ \omega) \tag{4.20}$$

The faulted system model is first numerically integrated and evaluated at different successive time steps Δt. At each time step, the evaluated trajectory location is checked using the $inhull$ function. The resultant trajectory is shown in Fig. 4.13. The algorithm predicts that the faulted trajectory will reach the edge of the enlarged ROA after $t = 0.43s$ which sets system critical clearing time t_{cr}. If VSG is not reconnected to the infinite bus for $t > t_{cr}$, the VSG will not be able to get back to its pre-fault operating point and the system will become unstable.

The network is simulated using Matlab / Simulink environment using the parameters listed in Table 4.1. An open circuit fault is applied at the VSG output at simulation time $t = 4$. When the fault lasts 0.43 s and is then cleared, the VSG went back to its original steady state operating point, i.e. power angle $\delta_o = 0.4070°$ and $\omega = 0\ rad/s$ as shown by the blue curves in Fig. 4.14 (a) and (b) respectively. The corresponding output power is also shown in Fig. 4.14 (c). The VSG $\delta - \omega$ trajectory is also shown in Fig. 4.14 (d) which shows the system going back to its pre-fault equilibrium point and matches the algorithm predictions.

Moreover, the VSG was not able to return to its pre-fault equilibrium point when the fault is cleared after 0.44s which is longer than the predicted t_{cr} by 0.01s. After the fault is

cleared, the VSG power angle and frequency deviated from their pre-fault value as shown in by the orange curves in Fig. 4.14 (a) and (b). The VSG instability can also be observed in the continuous oscillation in its output power depicted in Fig. 4.14 (c). Finally, the VSG $\delta - \omega$ trajectory shows the system heading towards instability after the fault is cleared. This proves the validity of the algorithm in accurately predicting the network critical clearing time without relying on finding a specific Lyapunov function that must satisfy certain conditions e.g., passivity theorem and Popov's criterion. This can be challenging considering the increasing complexity of the nowadays power system networks and their components.

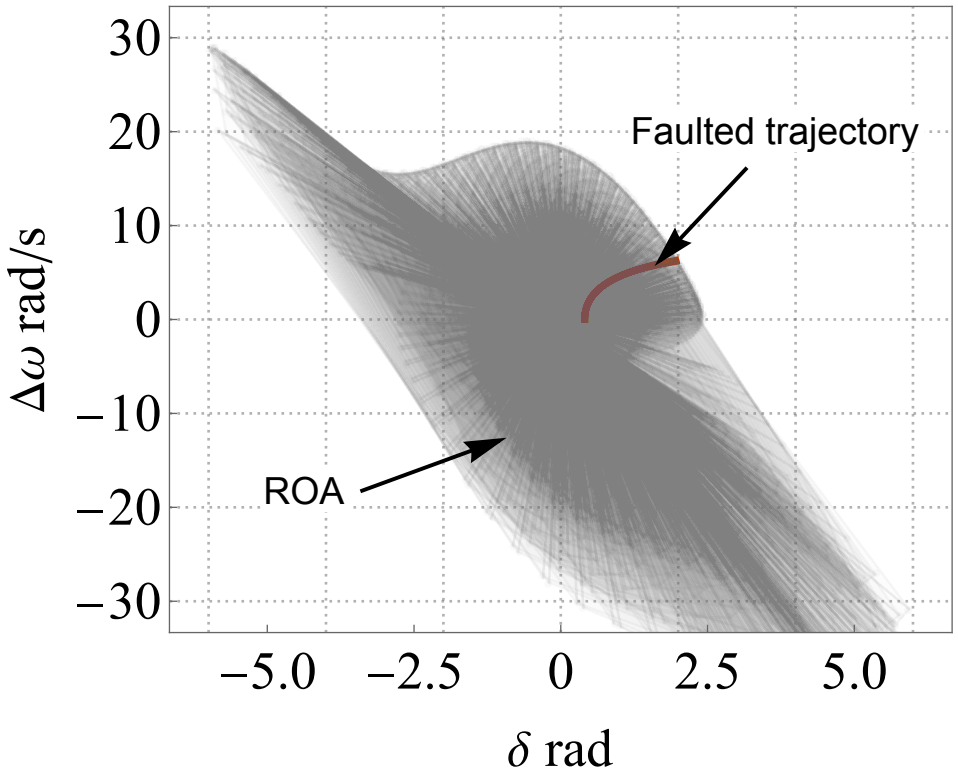

Fig. 4.13. Faulted trajectory (in red) against ROA estimated by convex hull-based algorithm.

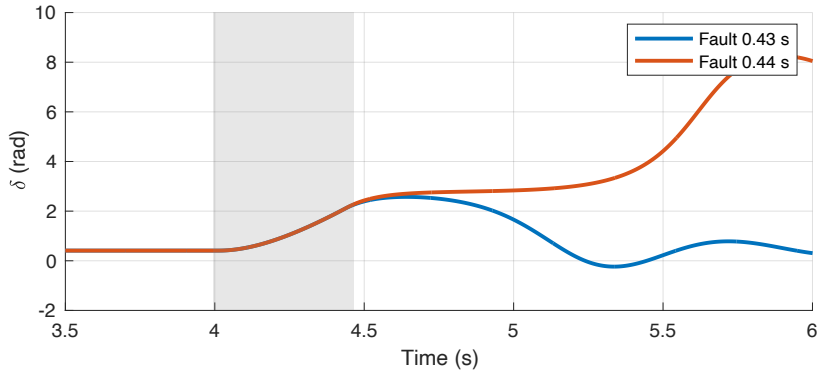
Fault 0.43 s
Fault 0.44 s
δ (rad)
Time (s)

(a)

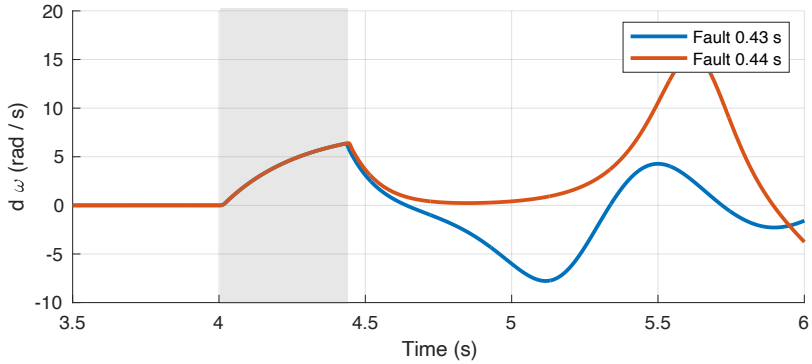
Fault 0.43 s
Fault 0.44 s
d ω (rad / s)
Time (s)

(b)

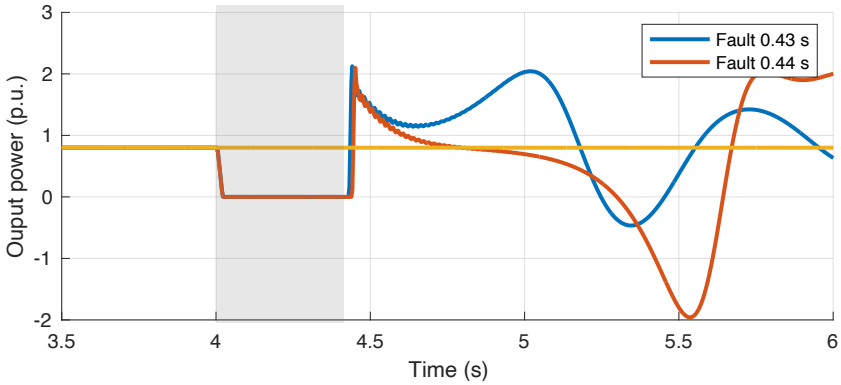
Fault 0.43 s
Fault 0.44 s
Ouput power (p.u.)
Time (s)

(c)

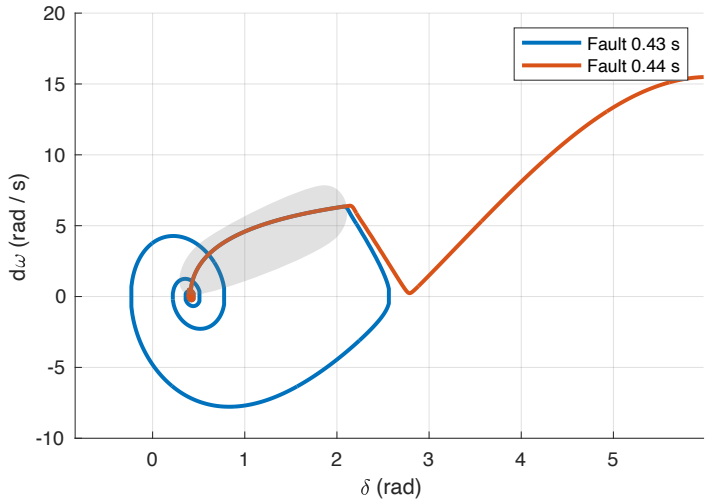

(d)

Fig. 4.14. Simulation results of the open circuit fault applied at VSG output at $t = 4\ s$; blue, fault cleared after 0.43 (stable); red, fault cleared after 0.44 (a) power angle; (b) frequency deviation; (c) VSG output power; (d) $\delta - \omega$ trajectory; fault period is shaded gray.

4. 3. 5. Proposed systematic and computationally efficient modification.

For the system shown in Fig 4.15 and the parameters listed in Table. 4.2, deriving from the definition of stability stated in chapter 1, the boundary of stability is the infimum of the unstable region. Hence, instead of starting from arbitrary small region close to the stable equilibrium point. The proposed modified algorithm starts from an arbitrary small region close to the unstable equilibrium point. However, this will result in a family of trajectories where most of them are branching in the unstable region and only a selective few contain the stable region. To overcome this, only the trajectories that are originated from points on the stable vectors are selected. The procedure of doing so is explained step-by-step shortly. This ensures that only the trajectories that bound the stable region are selected and they represent its supremum set. A convex hull can then be used to generate such a set which can be used to check system stability and calculate its critical clearing time. The major advantage of the proposed modification is significantly reducing the number of trajectories needed to stablish and enlarge the region of asymptotic stability, while producing

essentially the exact same result. This saves on the required computations and increases the speed by a large margin. For example, for the system shown in Fig.4.15 and Table 4.2 only two trajectories are needed to make a precise estimation of the ROA as opposed to minimum of 8 trajectories in original algorithms introduced in [56].

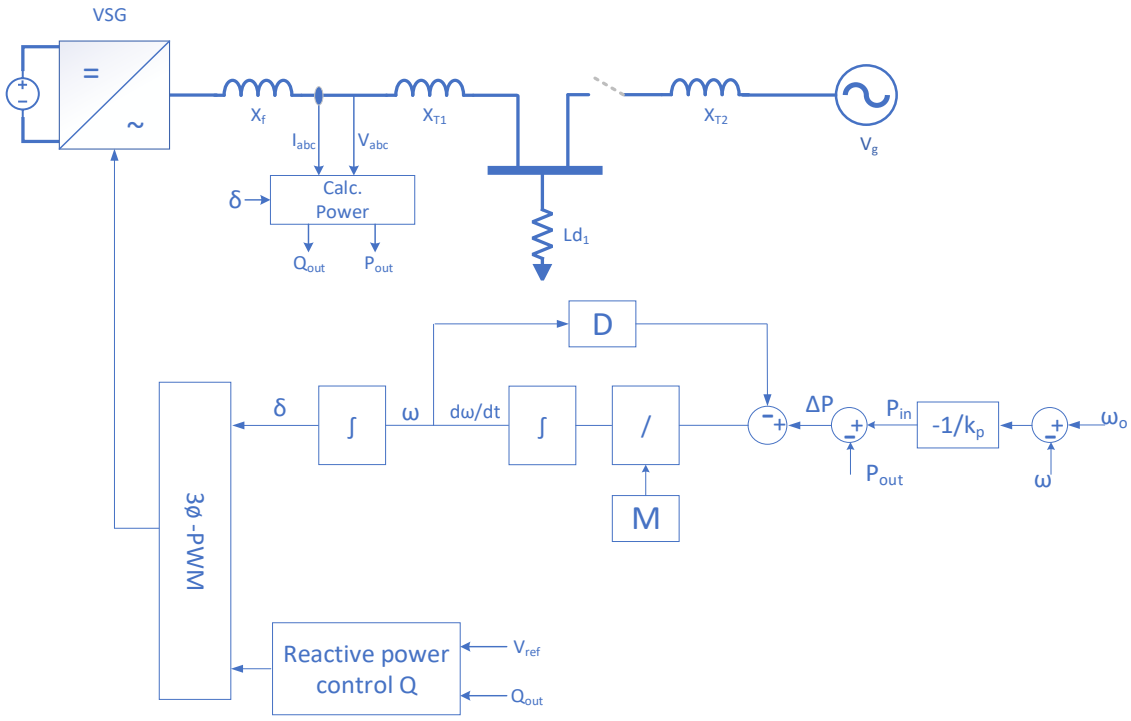

Fig. 4.15. The block diagram of the control loop with virtual inertia in islanding mode.

Table 4.2. Single VSG microgrid parameters

Parameter	Value
Virtual input reference power P_m	0.8 p. u.
Base power S	100 MVA
Grid line voltage v_g	13.8 kV
Power angle at steady state δ	0.4070rad
Grid power angle δ_g	0 rad
Total Line impedance	j0.5 p. u.
Infinite bus voltage v_g	1 p. u.
VSG voltage v_g	1.05 p. u.
Damping constant D	0.1
Inertial Constant M	5 s

The proposed modified algorithm first starts by calculating the VSG fixed points. This is done by equating its state space model in equation with zero as follows:

For grid connected VSG converter:

$$\dot{\delta} = \omega$$

$$\dot{\omega} = \frac{1}{M}\left(P_m - P_e Sin(\delta) - D\omega\right) \tag{4.21}$$

The fixed equilibrium points are calculated as follow:

$$0 = \omega$$

$$0 = \frac{1}{M}\left(P_m - P_e Sin(\delta) - D\omega\right) \tag{4.22}$$

Then,

$$\omega = 0$$

$$\delta = Sin^{-1}(\frac{P_m}{P_e}) \tag{4.23}$$

Because of the periodic solution of the equation (5.3), only the following three fixed points are considered:

$$a = \left(Sin^{-1}\left(\frac{P_m}{P_e}\right), 0\right), \qquad b = \left(Sin^{-1}\left(\frac{P_m}{P_e}\right) + \pi, 0\right), \qquad c = \left(Sin^{-1}\left(\frac{P_m}{P_e}\right) - \pi, 0\right)$$

Out of which, only the following is of importance to the grid connected system where only the positive power is considered:

$$a = \left(Sin^{-1}\left(\frac{P_m}{P_e}\right), 0\right)$$

Point (a) is the stable fixed point. Conventional algorithms start the trajectory reversing process from this point and branching out. The algorithm proposed in [56] uses sufficiently large number of points around this and uses convex haul to build n-dimensional matrix that contains the end points of all of these trajectories.

In the proposed modified algorithm, only two points around each one of the unstable fixed points i.e., points (b) and (c) are needed. Although points (b) and (c) are unstable fixed points of the grid connected converter, they are still classified as saddle points even in higher dimensions systems. In a two-dimensional system such as a grid connected converter, each saddle point has one stable eigenvector and unstable one, as shown in Fig. 4.16. In reverse time, the stable one become unstable and vice versa. Hence, if a trajectory starts on the unstable eigenvector (in reverse time) it will create a separating line that precisely divide the vector field of the system dynamics into stable and unstable regions. In fact, two trajectories are needed to cover the positive and negative directions of the unstable vector in reverse time starting from each staddle point, namely points (b) and (c).

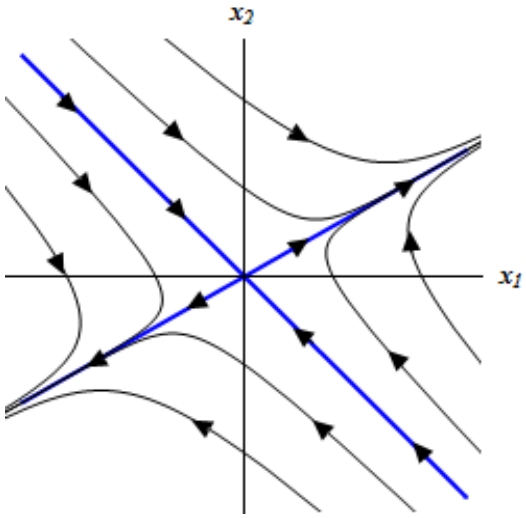

Fig. 4.16. Saddle equilibrium point

The procedure is explained for one of the saddle points which can be repeated for other one(s).

First, the grid connected VSG model is linearized around the unstable fixed point e.g., point (b). This is done by taking the Jacobian as follows:

$$A = \begin{bmatrix} \frac{\partial f_1(\delta,\omega)}{\partial \delta} & \frac{\partial f_1(\delta,\omega)}{\partial \omega} \\ \frac{\partial f_2(\delta,\omega)}{\partial \delta} & \frac{\partial f_2(\delta,\omega)}{\partial \omega} \end{bmatrix}, \qquad at\ (\delta,\omega) = \left(Sin^{-1}\left(\frac{P_m}{P_e}\right) + \pi, 0\right) \tag{4.24}$$

The eigenvalues of matrix A are $\Lambda = [\lambda_1, \lambda_2]$ and the corresponding eigenvectors are $V = [v_1, v_2]$. The solution of the linearized system is as follows:

$$\begin{bmatrix} \delta(t) \\ \omega(t) \end{bmatrix} = \begin{bmatrix} v_{11} \\ v_{12} \end{bmatrix} e^{\lambda_1 t} + \begin{bmatrix} v_{21} \\ v_{22} \end{bmatrix} e^{\lambda_2 t} + \begin{bmatrix} c_1 \\ c_2 \end{bmatrix} \tag{4.25}$$

For the negative direction:

$$\begin{bmatrix} \delta(t) \\ \omega(t) \end{bmatrix} = -\begin{bmatrix} v_{11} \\ v_{12} \end{bmatrix} e^{\lambda_1 t} - \begin{bmatrix} v_{21} \\ v_{22} \end{bmatrix} e^{\lambda_2 t} + \begin{bmatrix} c_1 \\ c_2 \end{bmatrix} \tag{4.26}$$

Here we assume that λ_1 and the corresponding $v_1$are the stable eigenvalue and stable eigenvector respectively in forward time.

By setting the unstable eigenvector in forward time to zero, the resultant is a system of equations that describes the stable one at time reverse is as follows:

$$\begin{bmatrix}\delta(t)\\ \omega(t)\end{bmatrix} = \pm \begin{bmatrix}v_{11}\\ v_{12}\end{bmatrix} e^{-\lambda_1 t} + \begin{bmatrix}c_1\\ c_2\end{bmatrix} \tag{4.26}$$

The constant vector $C = [c_1 , c_2]$ can by calculated by substituting for the staddle point (b) at $t = 0$. While the negative sign is set enable to allow for reverse time calculations.

The parametric plot of these equations represents the solution vector in both negative and positive direction at $t = [0, t_1]$. Hence, two points can be calculated around the fixed saddle point (b) at arbitrary small time $t = t_\varepsilon$ which are located on the stable eigenvector in forward time. These two points $\left(\delta(t_{\varepsilon+}), \omega(t_{\varepsilon+})\right)$ and $\left(\delta(t_{\varepsilon-}), \omega(t_{\varepsilon-})\right)$ will be the starting points of the two reversed trajectories that will be used to estimate the system's ROA. It is worth to mention that the same idea is applicable in systems with higher dimensions by calculating the planes instead of the trajectory lines.

The next step is to compute the points set that is used by convex hull algorithm to build an estimation of the system's ROA. This is done by numerically integrating the system model descripted in equation (4.16) twice at fixed time step Δt starting from each one of the points calculated in the previous steps $\left(\delta(t_{\varepsilon+}), \omega(t_{\varepsilon+})\right)$ and $\left(\delta(t_{\varepsilon-}), \omega(t_{\varepsilon-})\right)$. The resultant is a highly accurate estimation of the system's ROA, thanks to the location of these points on the two trajectories that are located on the borderline between the stable and unstable region of the system's phase plane.

Numerical example

For the system shown in Fig. and its parameters in Table 4.2:

Step one: Calculating system fixed points.

This is done by setting the derivatives to zero.

Hence,

$$\omega = 0$$

$$\delta = Sin^{-1}\left(\frac{P_m}{P_e}\right) = Sin^{-1}\left(\frac{0.8}{2.1}\right) \tag{4.27}$$

The resultant stable fixed points are indicated in Fig. 4.17 where point (a) is $(0.4070\ ,0)$, the unstable saddle points (b) and (c) are $(2.7345\ ,0)$ and $(-3.5486\ ,0)$, respectively.

In the next step, only the unstable points are considered. The procedure is explained for point (b) which can be easily repeated for point (c).

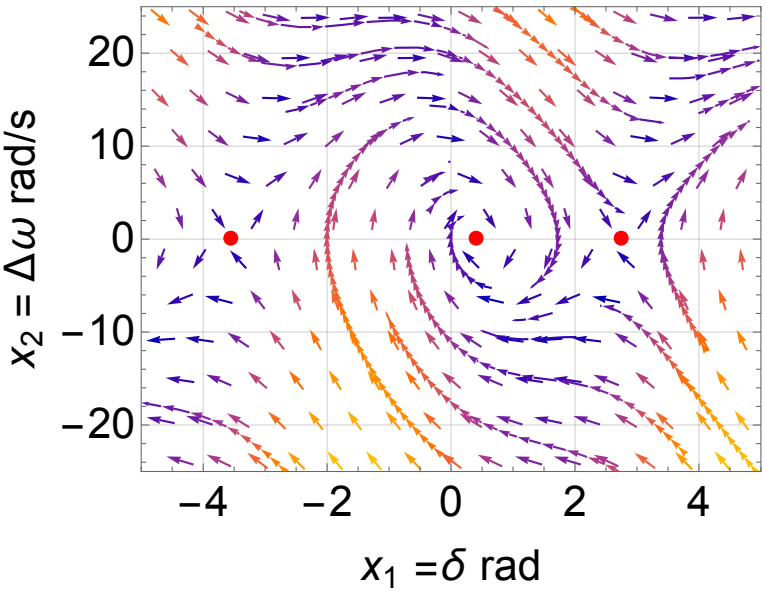

Fig. 4.17. System's fixed points

Step two: Linearizing system model.

This is done by calculating the system Jacobian as follows:

$$\begin{bmatrix}\dot{\delta}\\ \dot{\omega}\end{bmatrix} = \begin{bmatrix}\frac{\partial f_1(\delta,\omega)}{\partial\delta} & \frac{\partial f_1(\delta,\omega)}{\partial\omega}\\ \frac{\partial f_2(\delta,\omega)}{\partial\delta} & \frac{\partial f_2(\delta,\omega)}{\partial\omega}\end{bmatrix}\begin{bmatrix}\delta(t)\\ \omega(t)\end{bmatrix} \tag{4.28}$$

A is the linearized matrix at the unstable point (b)

$$A = \begin{bmatrix} \frac{\partial f_1(\delta,\omega)}{\partial \delta} & \frac{\partial f_1(\delta,\omega)}{\partial \omega} \\ \frac{\partial f_2(\delta,\omega)}{\partial \delta} & \frac{\partial f_2(\delta,\omega)}{\partial \omega} \end{bmatrix}, \quad at\ (\delta,\omega) = (2.7345\ , 0) \tag{4.29}$$

Then,

$$A = \begin{bmatrix} 0 & 1 \\ -P_e \frac{Cos(\delta)}{M} & \frac{-D}{M} \end{bmatrix}, \quad at\ (\delta,\omega) = (2.7345\ , 0) \tag{4.30}$$

$$A = \begin{bmatrix} 0 & 1 \\ 69.95 & -3.77 \end{bmatrix} \tag{4.31}$$

The linearized model is as follows:

$$\begin{bmatrix} \dot{\delta} \\ \dot{\omega} \end{bmatrix} = \begin{bmatrix} 0 & 1 \\ 69.95 & -3.77 \end{bmatrix} \begin{bmatrix} \delta(t) \\ \omega(t) \end{bmatrix} \tag{4.32}$$

Step three: Calculating initial points of reversed trajectories.

This step starts by determining the eigenvalues of the system $\Lambda = [\lambda_1\ , \lambda_2]$ and their corresponding eigenvectors $V = [v_1\ , v_2]$.

For the matrix A:

$$\Lambda = [\lambda_1\ , \lambda_2] = [-10.46\ , 6.67] \tag{4.33}$$

And

$$V = [v_1, v_2] = \begin{bmatrix} -0.095 & 0.99 \\ 0.15 & 0.99 \end{bmatrix} \tag{4.34}$$

λ_1 and v_1 are the stable eigenvalue and eigenvectors of matrix A in forward time. Hence, they will be the ones used to calculate the initial points of the reverse trajectories.

The solution of the linearized differential equation is as follows:

$$\begin{bmatrix}\delta(t)\\ \omega(t)\end{bmatrix} = \begin{bmatrix}1.067\\ -11.16\end{bmatrix} e^{-(-10.46)t} + \begin{bmatrix}1.67\\ 11.16\end{bmatrix} e^{-(6.67)t} \tag{4.35}$$

By eliminating the unstable vector in forward time and solve for the constants, the equation of the positive and negative vectors of interest becomes:

$$\begin{bmatrix}\delta(t)\\ \omega(t)\end{bmatrix} = \pm\begin{bmatrix}1.067\\ -11.16\end{bmatrix} e^{-(-10.45)t} + \begin{bmatrix}1.67\\ 11.16\end{bmatrix} \tag{4.36}$$

Two points can be calculated one on both positive and negative direction of the solution vector at arbitrary small time $t_\varepsilon = 0.01s$, and are indicated in Fig. 4.18. Those points are the two initial points from which the reverse trajectories start, as shown in Fig. 4.19:

$$x_{o1} = \left(\delta(t_{\varepsilon+}), \omega(t_{\varepsilon+})\right) = (2.54\,, 2.1)$$

$$x_{o2} = \left(\delta(t_{\varepsilon-}), \omega(t_{\varepsilon-})\right) = (2.99\,, -2.59) \tag{4.37}$$

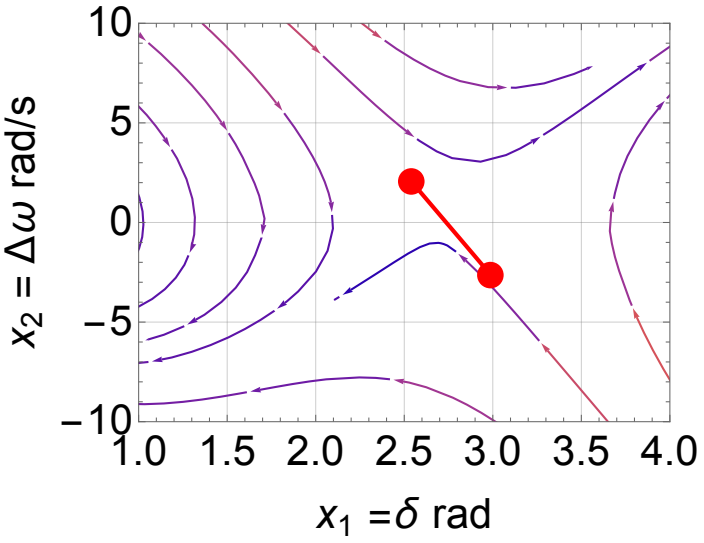

Fig. 4.18. trajectories' initial points on the unstable vector in reverse time.

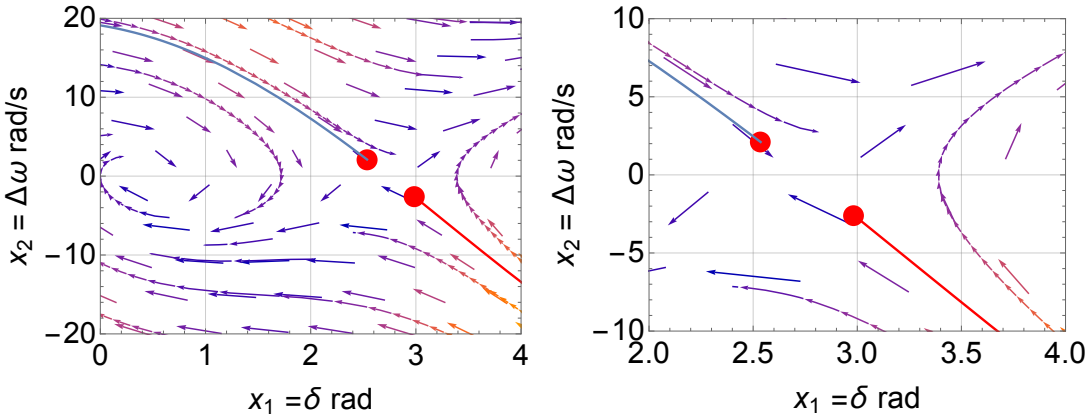

(a) (b)

Fig. 4.19. reversed trajectories; (a) is the reversed trajectories started at the unstable fixed points; (b) is a zoom in view of the initial points of the trajectories.

Step four: Using reverse trajectories to generate a set of points on the border line of the ROA.

This step starts by backward numerical integration of the VSG model in equation (4.38). This is done be multiplying it by negative one such that:

For the VSG model

$$\dot{\delta} = \omega$$

$$\dot{\omega} = \frac{1}{M}\left(P_m - P_e Sin(\delta) - D\omega\right) \tag{4.38}$$

The backward model is:

$$\dot{\delta} = -\omega$$

$$\dot{\omega} = -\left[\frac{1}{M}\left(P_m - P_e Sin(\delta) - D\omega\right)\right] \tag{4.39}$$

Hence, reversed vector field and reversed trajectories can be obtained by integrating the equations in 4.39, which is known as backward integration.

The backward integration is performed twice, each time using one of the initial points calculated in step three at fixed time intervals Δt. The resultant trajectories are depicted in Fig. 4.20.

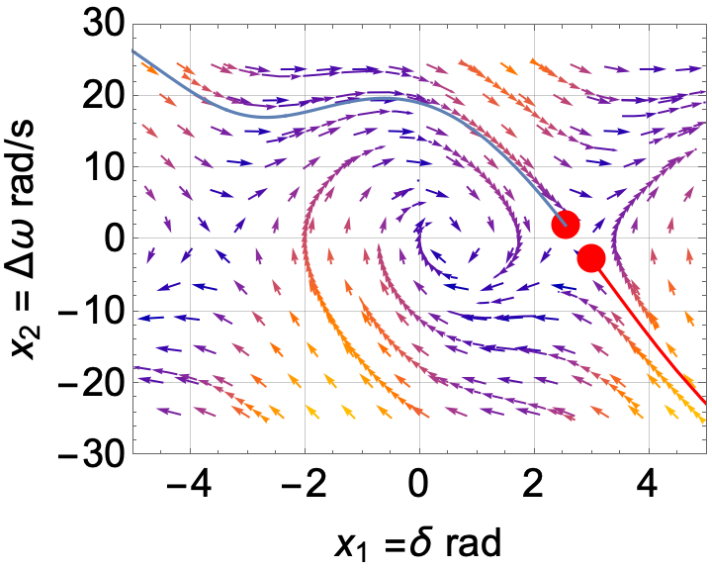

Fig. 4.20. Reversed trajectories using backward integration using the proposed method.

These time intervals can be as small as possible to guarantee smooth solution without increasing computation time beyond reasonable limit. The result is a set of points Ω that are located on the border line between the stable and unstable regions. They are the supremum set of the ROA of the grid connected VSG. The set Ω is shown in Fig. 4.21 and is defined as follows:

$$\Omega = \{x: x \in X(\delta, \omega, x_{o1}, t) | X(\delta, \omega, x_{o2}, t)\} \tag{4.40}$$

Where $X(\delta, \omega, x_{o1}, t)$ and $X(\delta, \omega, x_{o1}, t)$ are solution trajectories using backward integration starting from the two initial points x_{o1} and x_{o2} calculated in step two.

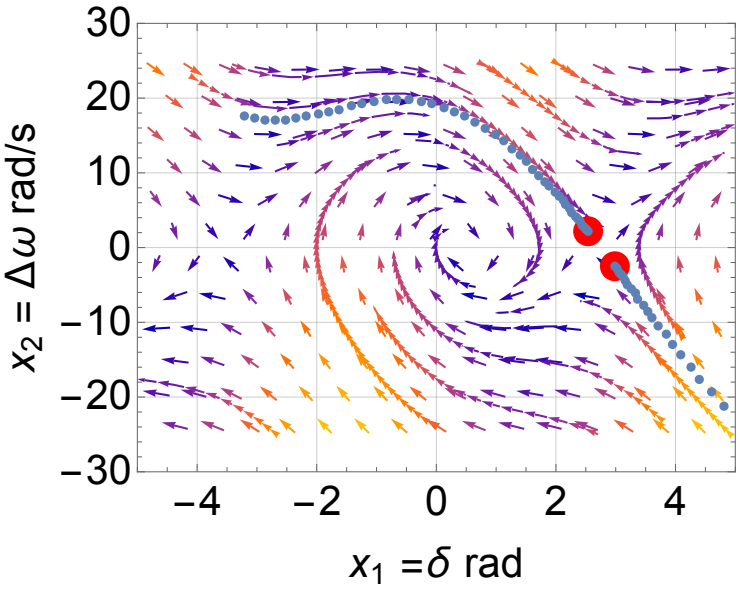

Fig. 4.21. The result is a set of point Ω that are located on the border line between the stable and unstable region.

Step five: Using Convex hull to build ROA expression.

Steps one to four are repeated for the other saddle point (point (c)). Then, a convex hull algorithm can be used to create a mathematical representation of the smallest region that includes all other points in the set Ω by a set of equations and inequalities. Hence, effectively produces a mathematical representation of the VSG ROA. The Quick Hull Algorithm [72] in Matlab can be used to compute the convex hull of the set Ω efficiently. The resultant convex hull is plotted against system vector filed in Fig. 4.22.

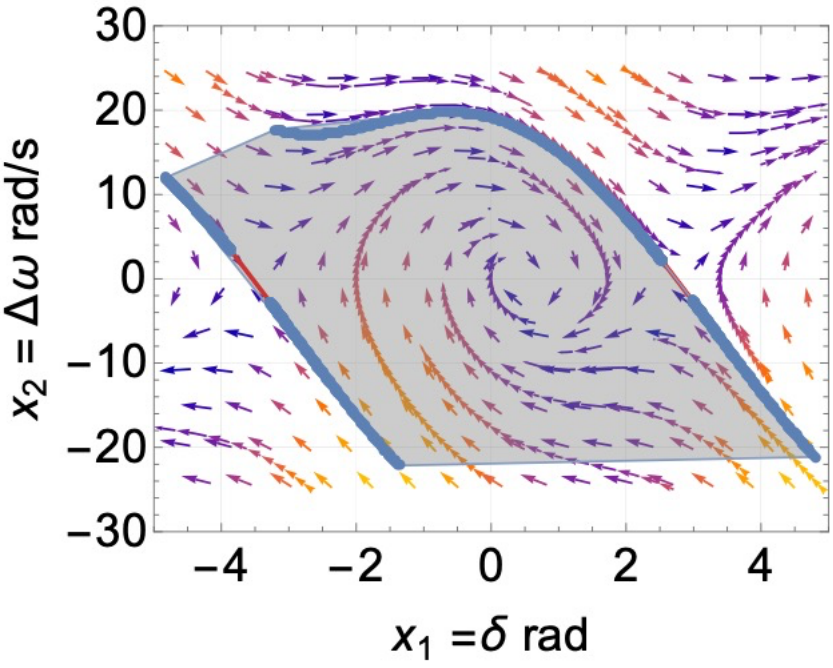

Fig. 4.22. Resultant convex hull.

Step six: Using In-hull algorithm to build ROA expression.

Once the convex hull set is created. The model of the faulted system i.e., grid connected VSG is numerically integrated using fixed time steps Δt. At each time step, In-hull algorithm [72] is used to check whether the solution trajectory still inside the convex hull set or not. If the trajectory of the faulted system is still contained inside of the convex hull set, the system will return to stability once the fault is removed, and no resynchronization is required. Once it is detected output of this region, the system becomes unstable and the accumulation of time steps it took to reach this state is the system critical clearing time $t_{cr} = \Sigma\, \Delta t$.

5. Proposed Enhanced Virtual Inertia Controller (EVIC)

5. 1. Introduction

The stability of a conventional power system is largely considered around the fundamental characteristics of a synchronous generator (SG). By analysing its output voltage, power and frequency, a distinction can be made between, for instance, various levels of load transients or faults. Similarly, a VGS is introduced to observe such relations and characteristics while enabling the integration of a variety of renewable energy sources and energy storage systems [35].

From power – frequency point of view, SG and VSG responses to various kinds of disturbances are proportional to their inertia coefficients based on their swing equations. That is, if the inertia coefficient is relatively low, the rate of change of frequency (RoCoF) within a given microgrid is higher. On the positive side, it results in a faster response and shorter settling time. Nonetheless, it leads to high frequency and power oscillation as well as a reduction in stability margins. A higher inertia coefficient results in a sluggish response with affects the power sharing among different SGs and hurts the stability as well. It, however, reduces the power and frequency oscillations to a minimum [6].

Fortunately, unlike SGs, the VSGs' inertia is not fixed once it is manufactured and only has an upper limit defined by its energy storage components such as the dc-link capacitor, ultra capacitors, batteries, super inductors … etc. This gives flexibility to the controller to adjust the inertia coefficient in real-time to improve system response and is only bounded by its upper limit. This method of control was first introduced in [24] and is referred to as alternative inertia, variable inertia, or synthetic inertia and its generic block diagram is shown in Fig. 5.2.

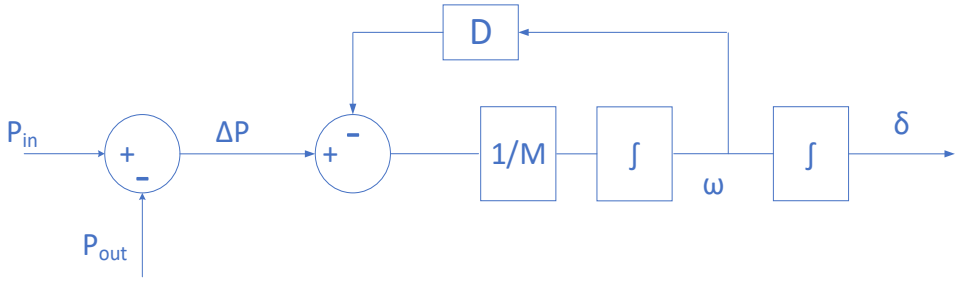

Fig. 5.1. Generic block diagram of virtual inertia controller.

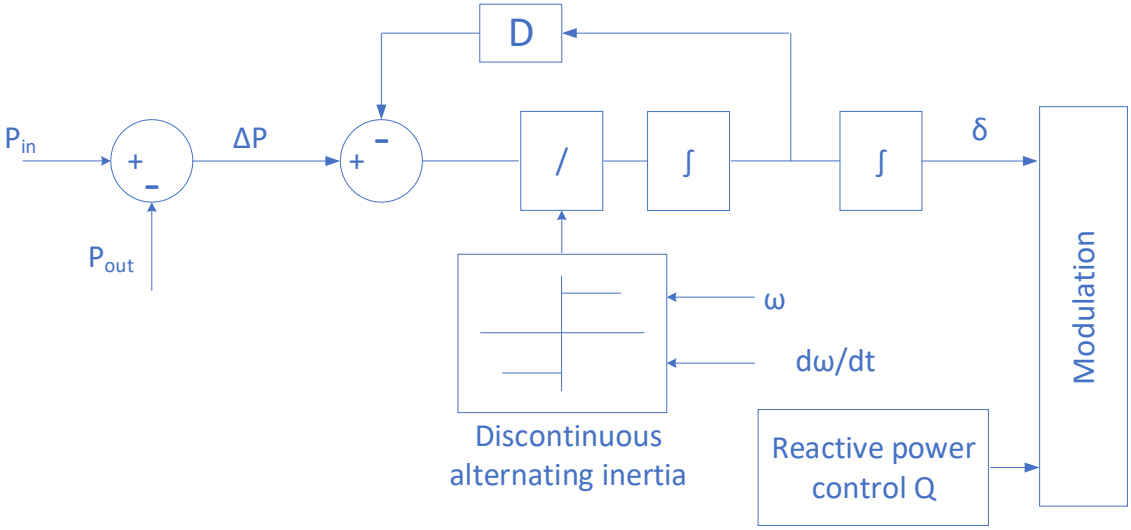

Fig. 5.2. Block diagram of discontinuous alternating virtual inertia controller.

5. 2. Concept of alternating inertia

The value of the virtual inertia in each VSG is varied based on the rate of change of its power angle $d\delta/dt$ and its acceleration $d^2\delta/dt^2$. That is, if they are going in the same direction, i.e., if they have the same signs, the VSG is going in the right direction and its inertia is switched to a higher value to prevent oscillation. On the other hand, if their signs are different, then the VSG is going in the wrong direction (away from steady-state point) and hence, the inertia is switched to a lower value to shorten such overshoot / undershoot periods.

This concept is further explained as follows. Suppose a VSG in a single VSG microgrid operates at the steady state power angle δ^{s1} , as shown in Fig. 5.3. Suppose that the load power increases. The steady-state power angle moves from $\delta^{s1}$to δ^{s2} to satisfy the load demand. The transient from $\delta^{s1}$to δ^{s2} is oscillatory due to the existence of complex eigenvalues. On the power curve, this means that the operating point moves from point a to point b which results in a positive rate of change of frequency (RoCoF) $\frac{d^2\delta}{dt^2}$ or in other words acceleration, while rate of change in power angle is positive as well $\frac{d\delta}{dt}$. Once it passes point b towards point c, the rate of change in frequency (RoCoF) becomes negative while the rate of change in power angle is still positive, which means deceleration. On the other hand, the rate of change in power angle is still positive.

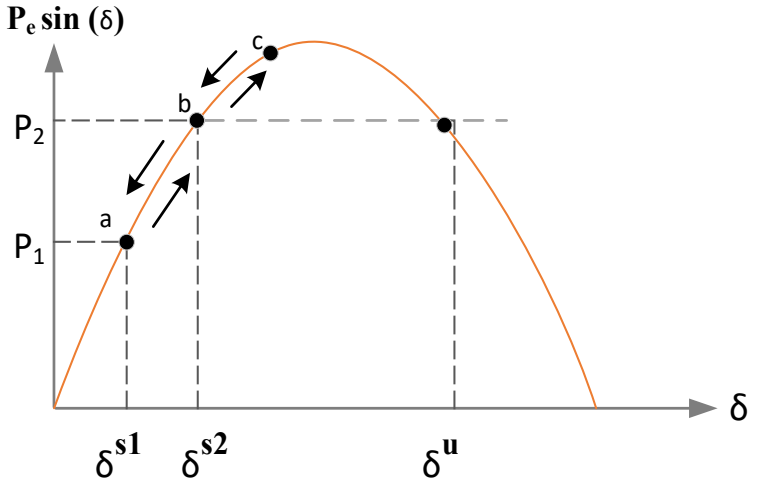

Fig. 5.3. VSG power-angle transient oscillation

Same behavior is repeated in the opposite direction. That is, the system accelerates once it starts to move back from point c to point b, and decelerates after crossing point b towards point a. This cycle is repeated until the VSG settles on the new operating point b of the new power angle δ^{s2}. Such an oscillation is reflected mainly in the output power as the input power here is virtual. It also greatly impacts on the stability of microgrids, specially the ones with multiple VSGs, as such oscillations can be amplified and result in loss of synchronism [2].

It can be seen from the typical swing equation (equation 5.1) for the preceding scenario, the acceleration direction is the desirable one, as it means that the inverter is moving towards the steady-state point. While in deceleration, it moves away from it. Therefore, it is desirable to shorten the deceleration periods and magnitudes as much as possible in favor of the acceleration ones.

$$M\frac{d^2\delta}{dt^2} + D\frac{d\delta}{dt} = \left(P_m - P_e\, Sin(\frac{d\delta}{dt})\right) \tag{5.1}$$

To achieve such an objective, the inertia coefficient M is altered as a function of the rate of change in frequency and power angle. That is, during acceleration periods, the inertia is set to its normal (maximum) value which gives time to the microgrid to detect the rate of change in frequency (RoCoF) and adjust its parameters (e.g., secondary, and tertiary control parameters, protection relays … etc). During the deceleration periods, the inertia M is set to a lower value which reduces the size and the time constant of the VSG. It is worth mentioning that this is only possible in VSG controlled inverters as their inertia is just a virtual quantity M with only an upper limit tied to a physical quantity M_{max}.

In the literature, the inertia coefficient M is alternated discontinuously between two values: M_{max} during acceleration and M_{min} during the deceleration. Equation (5.2) formulizes this technique as follows [24], [38], [73]–[75]:

$$M = \begin{cases} M_{max} & \frac{d\delta}{dt} * \frac{d^2\delta}{dt^2} > 0 \qquad (acceleration) \\ M_{min} & \frac{d\delta}{dt} * \frac{d^2\delta}{dt^2} < 0 \qquad (deceleration) \end{cases} \tag{5.2}$$

Although this technique has proven to be effective, it suffers from some drawbacks due to its discontinuous nature. The VSG inertia changes abruptly during a transition between the two levels no matter how small the disturbance is, which does not guarantee system stability. In other words, for small disturbances, such as a small load change, VSG inertia alternates between the highest and lowest values (defined in equation (5.2)) which is the exact same response in the case of large disturbances. Moreover, during steady-state operation, inertia chattering is noticed because of negligible variations in the frequency and power angle, or measurement noises. For example, 0.1% change in power angle and

frequency will result in 100% change in VSG inertia coefficient up to its maximum or minimum limits, as it only relies on the product of sign of change (positive / negative), even though such a variation comes only from measurement noise not actual load variation. This can lead to long term instability, especially when multiple VSGs that use this technique are interconnected.

From a stability point of view, it is difficult to study or prove the stability of a microgrid under alternative virtual inertia control, as measurement noise or very small load variations can result in a continuous variation of inertia coefficient value. Hence, the limits in the accuracy in defining the MG model and initial conditions. It is not possible using linear analysis tools such as Nyquist or root-locus, as they require linearization around one operating point i.e., one value of the inertia. Regardless, studying the system under the two values of inertia only shows the stability range between these two values without providing any qualitative or quantitative insights on system performance. More importantly, due to linearization, such linear analysis does not guarantee an exact stability estimate under large disturbances i.e., far from the linearized segment. Finally, such a study, assuming it is satisfactory, cannot be extended to a microgrid formed with multiple VSGs as there is no way to instantaneously correlate the inertia coefficient of each VSG with respect to the others or to the applied disturbance.

Although nonlinear analysis overcomes the limitations imposed by linearization, studying a system with switching behavior such as jumping discontinuously between two different states, requires a special treatment and theories which can not be easily generalized or extended. It is worth mentioning here that, Lyapunov and Lyapunov-like stability analysis tools are limited to smooth and continuously differentiable systems [49].

It can be seen from the preceding discussion that a new control technique is needed to overcome the drawback of conventional alternating inertia technique, without compromising its appreciated merits.

5. 3. Proposed enhanced virtual inertia controller (EVIC)

The proposed enhanced virtual inertia controller (EVIC) is based on an alternating inertia technique which is shown in Fig. 5.2 and formulated in equation (5.2). That is, the inertia coefficient alters between two levels in response to a grid transient. The key difference is that the proposed EVIC causes a smooth transition in inertia coefficient while an alternating inertia controller causes a discontinuous jump in it.

In the proposed controller, inertia equation (5.2) is replaced by the proposed equation (5.3) as follows:

$$M\ (\Delta P, \omega) = \mathrm{M_{nom}} + \frac{\Delta M}{2} \tanh(a\ \Delta P\ \omega) \tag{5.3}$$

Where,

M_{nom} is the inertia nominal value at the steady-state,

ΔM is the difference between the minimum and maximum allowable variation in M, i.e. $\Delta M = M_{max} - M_{min}$

a is the slope of inertia variation in the linear region,

ΔP is the difference between virtual input mechanical power and output electrical power of a VSG.

ω is VSG frequency variation which equals to the rate of variation of VSG power angle $d\delta/dt$ with respect to the reference frame.

An understanding of the properties of the hyperbolic function $\tanh(.)$ is needed to understand the origin and behavior of the proposed controller. Typical $\tanh(x)$ curves are plotted in Fig. 5.4. At small values of $|x|$, $\tanh(x)$ is almost a linear unity gain over the domain $|x| < 1$. Beyond that, $\tanh(x)$ acts as an ideal saturation function with a peak range of one $|\tanh(x)| = 1\ \forall |x| \geq 1$. It is obvious then that $\tanh(x)$ provides a smooth transition between its linear region and saturation, and conveniently between its upper and lower saturation limits. Moreover, the linear gain region can be adjusted with the coefficient a $[\tanh(a\ x)]$ to be sharper or more relaxed as shown in (5.4). Saturation levels can also

be scaled with the coefficient b [b $\tanh(a\,x)$]. Finally, a bias level c can be added to maintain the variation within the positive domain. Thus, based on these parameters, the function is rewritten as follows:

$$z\,(x) = c + \mathrm{b}\,\tanh(a\,x) \tag{5.4}$$

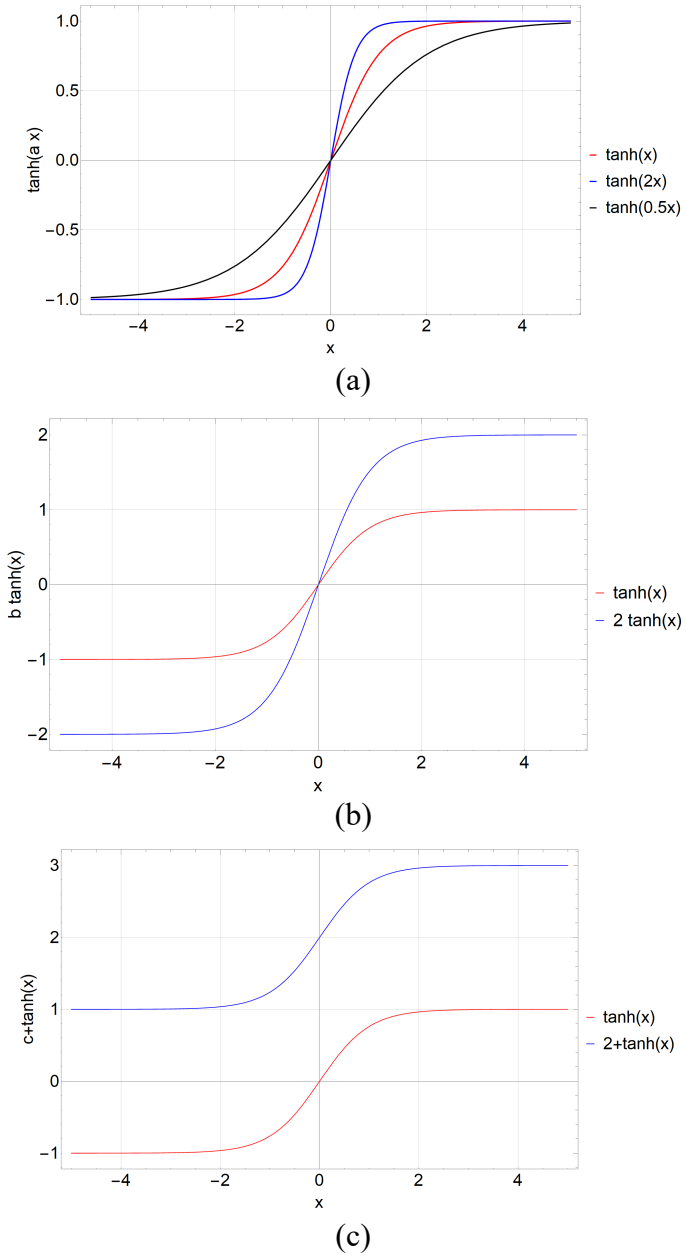

Fig. 5.4. Plot of different $tanh(x)$ based functions; (a) tanh (ax) at $a = 0.5, 1, and\ 2$ (b) b tanh(x) at $b =\ 1, and\ 2$ (c) $c +$ tanh(x) at $c = 0,\ and\ 2$

The proposed EVIC receives help from these properties in controlling the inertia coefficient in a VSG. In fact, equation (5.4) is identical to the controller equation (5.3). Where:

I) $z(x) = M\ (\Delta P, \omega)$, the bias level is inertia nominal value $c = \mathrm{M_{nom}}$.

II) The saturation levels are the minimum and maximum variations in inertia and are expressed as $b = \frac{\Delta M}{2} = (M_{max} - M_{min})/2$.

III) The slope of the inertia varies in the linear region a which is set based on the design preference.

IV) Finally, x is the product of the power mismatch and frequency deviation $x = \Delta P\ \omega$.

The proposed EVIC controller is shown in Fig. 5.5 and is explained as follows. In steady-state, both virtual input power and electrical output power are equal, hence, $\Delta P = 0\ p.u.$ Also, VSG is expected to follow its reference frequency with an appropriate constant power angle δ, hence $\omega = 0\ p.u.$ Therefore, EVIC equation (5.3) becomes (5.5) and converter's inertia equals to its nominal value $\mathrm{M_{nom}}$ as follows:

$$M\ (\Delta P, \omega) = \mathrm{M_{nom}} + \frac{\Delta M}{2}\tanh(0)$$

$$M\ (\Delta P, \omega) = \mathrm{M_{nom}} \tag{5.5}$$

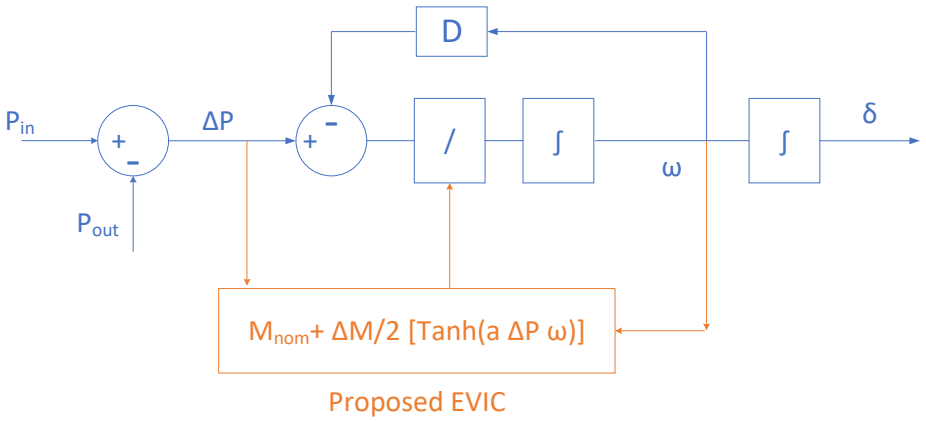

Fig. 5.5. Proposed controller EVIC block diagram

During a transient state, for example in the case of a load transient, a mismatch between the virtual mechanical input power and the output electrical power occurs which causes a positive (acceleration) or negative (deceleration) rate of change in the frequency (RoCoF) ($\frac{d^2\delta}{dt^2}$ α ΔP), and a deviation from the reference frequency ω. Therefore, the inputs of the hyperbola function $\tanh(\cdot)$ are no longer zero, and hence, the converter's inertia varies as well, based on equation (5.3). However, unlike alternating inertia controller, the variation in inertia does not pulsate between two saturation levels M_{max} and M_{min} despite the magnitude of the transient or disturbance.

The variation in inertia caused by the proposed EVIC is proportional to the magnitude of applied disturbance (e.g., load transient) and how far the VSG converter is from its equilibrium point (operating point at steady-state). That is, for a given slope a in equation (5.3), for a small load transient the product of ΔP and ω is small, and hence, the change in VSG inertia $M\ (\Delta P, \omega)$ is minimal and can be negligible $M\ (\Delta P, \omega) \cong \mathrm{M_{nom}}$. This is especially useful in a linear study and analysis, where the variation in the converter's states must be practically small. In other words, under linearization, the proposed EVIC can be treated essentially as a constant inertia without any practical mismatch between the actual implementation and linearized model. Such an assumption would not be true in a conventional alternating inertia controller. Moreover, for higher disturbance magnitudes, the proposed EVIC linearly changes converter's inertia by virtue of its linear region, as explained earlier and shown in Fig. 5.6.

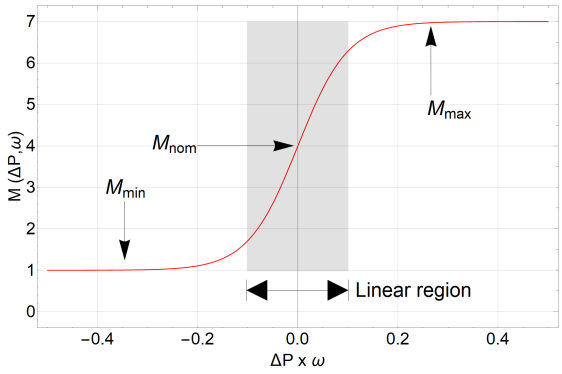

Fig. 5.6. Example of inertia variation using proposed EVIC nominal 4 $p.u.$, minimum 1 $p.u.$, and maximum 7 $p.u.$

During the disturbance, such as a load transient, VSG controller is slowly adjusted till its virtual mechanical input power matches its electrical output power. based on its droop gain k_p. This results in a gradual reduction in ΔP and ω. In response, EVIC gradually varies VSG inertia in the same manner towards its nominal value the closer the converter is to its steady-state.

Thus, the proposed EVIC guarantees adaptive behaviors as follows:

- For low disturbances (small ΔP and ω) the controller's gain is very small and can be negligible, which eases the linear treatment of VSG and the microgrid it is connected to.
- For higher disturbances, the controller's gain increases linearly with slope a which varies VSG inertia smoothly around its nominal value between a lower value and a high value (not the maximum and minimum), which quickly damps out the oscillation in power and frequency caused by the disturbance.
- For large disturbances (large signal transient), EVIC oscillates the inertia between its saturation values (M_{max} and M_{min}) causing the converter to quickly return to its steady-state operating point with minimum oscillation in its power and frequency. Moreover, as will be shown next, the closer the converter is to its steady-state operating point, the lower the magnitude of the oscillation in its inertia.

5. 4. Large signal dynamics of EVIC

A qualitative study of the performance and stability margin of the proposed controller is done using large-signal model (nonlinear model) of VSG connected to a microgrid, as shown in Fig. 5.7. As opposed to a small-signal model (linearized model), the large-signal model provides a complete description of converter's behavior under large disturbances which is the area of interest of the proposed controller. It also contains the small-signal dynamics (linear dynamic) within the vicinity of the equilibrium (steady-state) point. Thus,

by studying large-signal dynamics, a complete description of proposed controller dynamics is conveyed to prove its validity and adaptability.

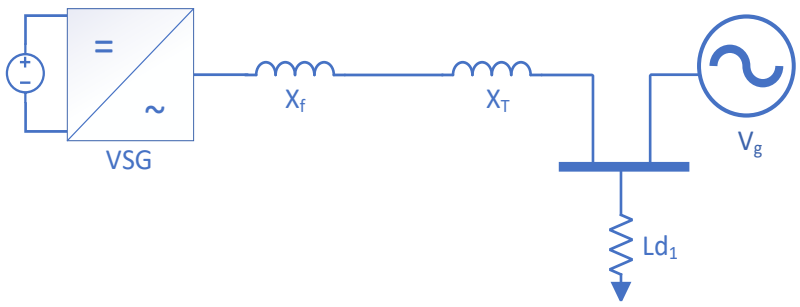

Fig. 5.7. VSG connected to microgrid.

The large-signal model (without EVIC) of a microgrid is shown in Fig 5.4:

$$\dot{\delta} = \omega$$

$$\dot{\omega} = \frac{1}{M}\left(P_m - P_e Sin(\delta) - D\omega\right) \tag{5.6}$$

Where,

δ is VSG's power angle in rad with respect to grid power angle,

ω is VSG's frequency deviation from grid power angle ω_g,

P_m is VSG's virtual mechanical input power,

P_e is VSG's rated electrical output power,

D is VSG's damping coefficient, and

M is VSG's inertia coefficient.

Based on equation (5.3), EVIC controlled VSG large-signal model is as follows:

$$\dot{\delta} = \omega$$

$$\dot{\omega} = \frac{1}{\mathrm{M_{nom}} + \frac{\Delta M}{2}\tanh(a\,\Delta P\,\omega)}\left(P_m - P_e Sin(\delta) - D\omega\right) \tag{5.7}$$

Large-signal dynamics of both models formulated in equations (5.6) and (5.7) are visualized by plotting their $\dot{\delta}$-$\dot{\omega}$ vector field in Fig. 5.8 using the parameters in Table 5.1. Several integral solutions are plotted starting from different initial points by following the succession vectors field in positive time ($t > 0$). Each curve in (5.8) shows how power angle and frequency of VSG change with respect to each other and move either towards the stable equilibrium point or away from it.

The black curves in Fig. 5.8 are corresponding to a VSG with conventional virtual inertia controller while orange ones are for it with the proposed EVIC. It is worth mentioning that conventional alternating inertia control, represented by equation (5.2), is not easy to represent due to its discontinuous nature. Hence, this shows the advantage of the proposed controller in terms of ease of applying all nonlinear analysis tools with no special treatment, compared with conventional alternating inertia.

Table 5.1. VSG parameters

Parameter	Value
Virtual input power P_m	$0.6\ p.u.$
Base power S	$3.125\ MVA$
Power angle at steady state δ	$0.203\ rad$
Grid power angle δ_g	$0\ rad$
Line impedance x_g	$0.43\ p.u.$
Grid line voltage v_g	$2.4\ kV$
Active power droop coefficient K_p	0.03
Reactive power droop coefficient K_q	0.03
Damping constant D	$1\ p.u.$
Inertial Constant $\mathrm{M_{nom}}$ normalized	$10\ s$
Inertial Constant $\mathrm{M_{min}}$ normalized	$5\ s$
Inertial Constant $\mathrm{M_{max}}$ normalized	$15\ s$
Simulation step time	10 us

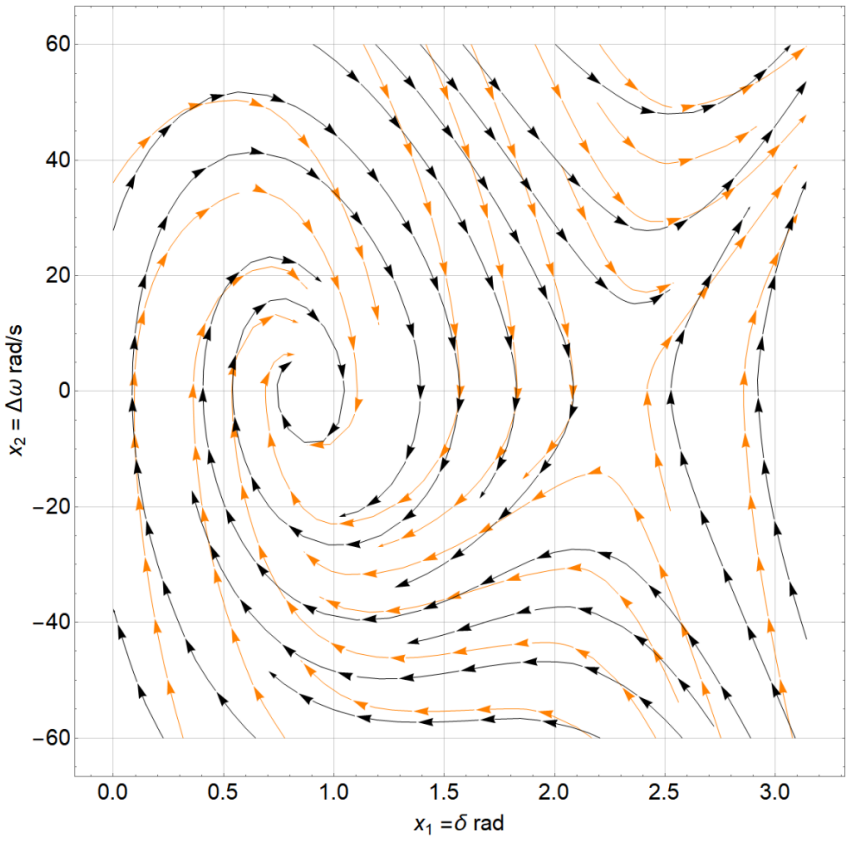

Fig. 5.8. Vector field and integral solution of VSG converter. Black curves are for conventional inertia controller, and the orange ones are for proposed EVIC.

To demonstrate the advantages of the proposed EVIC over a conventional inertia controller, the converter's behaviour starting from three different initial conditions is discussed. It is assumed that the VSG converter is subjected to a disturbance that causes it to move away from its equilibrium point to one of these initial conditions. Thus, the following discussion is related to the converter's recovery from each one of those initial conditions back to its equilibrium point.

1- In this case study, the converter starts from an initial point far away from its equilibrium point, but it is eventually led to it using both types of controllers. An example of such a case is the initial point ($\delta = 1\,rad,\ \omega = 50\,rad/s$). The converter's trajectories using the proposed EVIC (in red), and conventional inertia controller (in blue) are shown in Fig. 5.9.

Starting from the same point, the trajectory of a conventional inertia controller (blue in Fig. 5.9) takes a longer path to reach the VSG's equilibrium point, which means it has a longer settling time. Moreover, it has more spiral rotations before reaching the equilibrium point which is translated into more oscillations in the converter's frequency deviation and power angle, and thus, more power oscillations and increase in the losses. On the other hand, the proposed EVIC takes a much shorter path towards the equilibrium point with fewer spiral rotations and hence, much fewer oscillations. This proves the advantage of the proposed EVIC in bringing the converter very quickly to steady-state after being subjected to a large disturbance or load transient, with minimal oscillation and losses. This is due to its property of smoothly alternating its inertia, based on the profile shown in Fig. 5.6, between its saturation levels away from the equilibrium point and linearly when its closer to it.

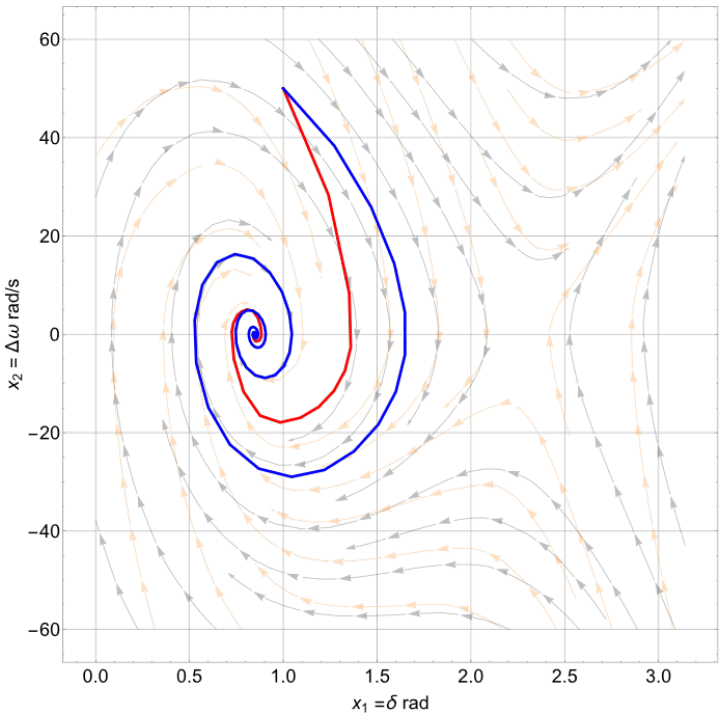

Fig. 5.9. VSG trajectories and dynamics in first case. Initial point is ($\delta = 1\ rad$, $\omega = 50\ rad/s$). Conventional inertia controller in blue and proposed EVIC in red.

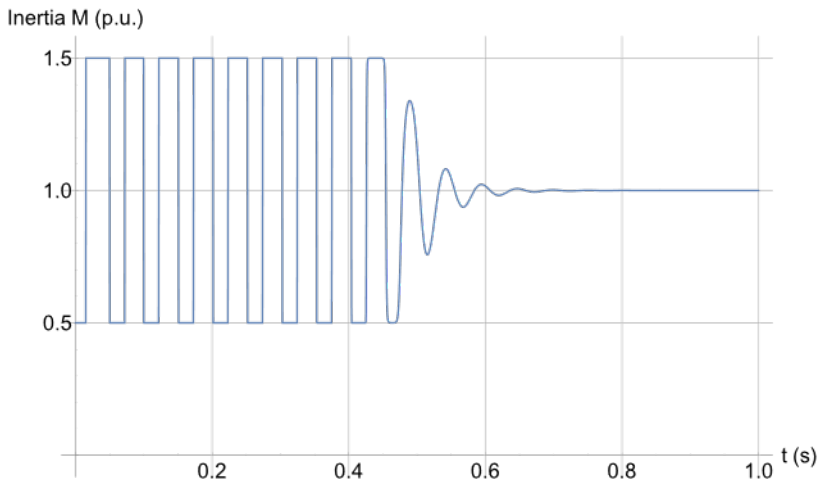

Fig. 5.10. Alternating inertia profile of proposed EVIC in first case

The resultant variation in inertia is shown in Fig. 5.10. for the same afore mentioned test conditions. It clearly shows the expected behavior of the proposed controller. As at the start, the VSG converter was far from its equilibrium point, thus, EVIC started with the minimum value of the inertia in Table 5.1 to quickly bring the converter back to its equilibrium point (acceleration). The closer the converter is to its equilibrium point (shown by its trajectory), the higher its inertia becomes (decelerations) till it reaches its maximum value stated in Table 5.1. if needed. This is done for a few cycles and depends on the severity of the applied disturbances. However, it is still much better than using a conventional inertia controller. At steady-state, the transient amplitude decayed to very low values close to the equilibrium point. Thus, the proposed controller changes the inertia to be almost equal to its nominal value or equal to it at steady-state. Another advantage is that, at any time instant, converter inertia is known and can be easily calculated and simulated. Unlike the conventional alternating inertia methods where there is uncertainty and ambiguity in its exact value due to constant variation of virtual inertia even at steady-state. Same qualitative results can be observed by choosing any initial point far away from the equilibrium point and following the system's vector field or the set of integral solutions shown in Fig. 5.9.

2- VSG converter starts from an initial point within the unstable region of conventional inertia controller ($\delta = 1.4\,rad$, $\omega = 60\,rad/s$). As expected, its trajectory in Fig.

5.11 (shown in blue) does not return to its designated equilibrium point. It follows the vector field and closest integral solutions and moves away from the stable region affected by the unstable eigen vector of the saddle point. In other words, the converter's power angle moves to the unstable quadrant of the swing equation curve. By contrast, the proposed EVIC can bring the trajectory back to the designated equilibrium point as shown in Fig. 5.8 (shown in red). EVIC inertia profile, shown in Fig. 5.12, is like the one discussed in the first case above.

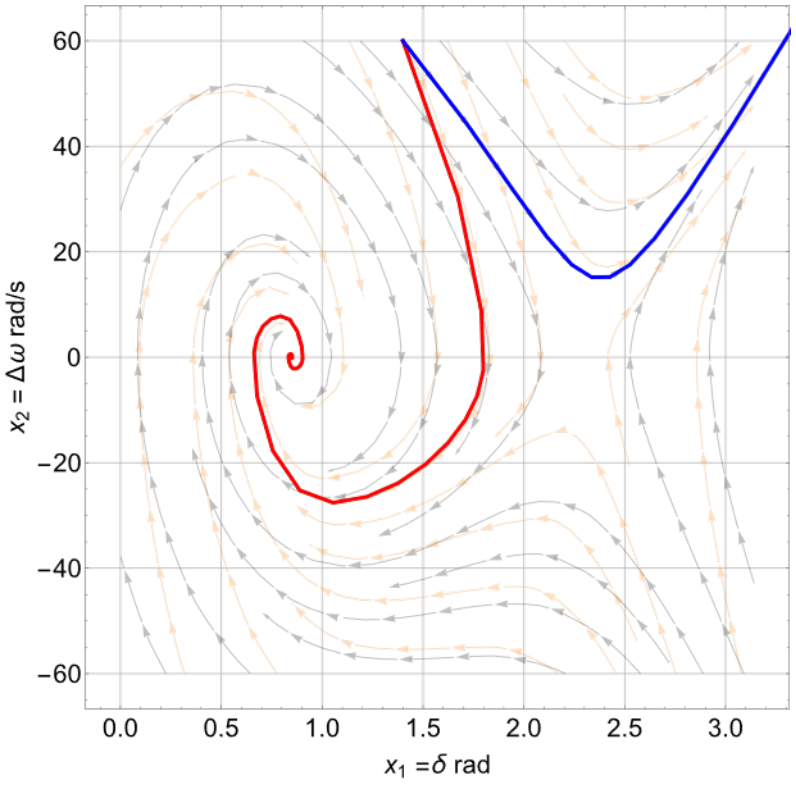

Fig. 5.11. VSG trajectories and dynamics in second case. Initial point is ($\delta = 1.4\,rad$, $\omega = 60\,rad/s$). Conventional inertia controller in blue and proposed EVIC in red.

As the initial conditions in this case are closer to the first case and the system exhibits similar dynamics as observed by integral solutions (shown in orange lines). The only difference is a slight increase in the upper transient inertia value, which is within the controller design. This test shows that, the proposed EVIC does not only help in reducing oscillation, power loss and settling time. It also increases converter's stability region (area

of attraction) beyond conventional inertia controllers, while maintaining the desired inertial characteristics.

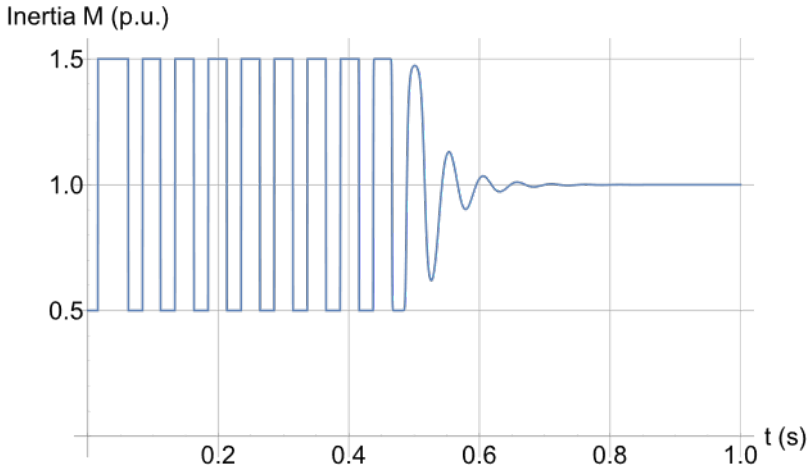

Fig. 5.12. Alternating inertia profile of proposed EVIC in second case

3- the initial point is chosen to be close to the equilibrium point ($\delta = 0.84\, rad$, $\omega = 1\, rad/s$). As can be seen from the corresponding trajectories (Fig. 5.13) that within the vicinity of the equilibrium point, both the proposed EVIC and the conventional inertia controller act almost identically. This proves the advantage of the proposed controller (EVIC) as it does not affect the converter's linear behavior (i.e., eigenvalues and eigenvectors). This is better shown with the help of Fig. 5.14, which shows a small variation around the nominal inertia coefficient value M_{nom} (stated in Table 5.1), hence, it can be assumed constant in linearization. This means that, all linearized models, analysis, and results are valid under the proposed controller, this saves time and effort that would have to be used to build other linear models and study their stability boundaries and so on.

Such behavior shown in these three cases combined (and summarized in Fig. 5.15) is unique to the proposed controller (EVIC) compared with other types of inertial controllers such as conventional inertia, alternative discontinuous inertia, and droop control-based inertia emulator. Moreover, the proposed controller does not require any additional measurements, sensors, or complicated adaptive algorithms or artificial intelligence ones

[39]. On the contrary, it is easy to be implemented, does not add any complexity in linear analysis and control, while adding more robustness to VSG converters and widen their regions of stability.

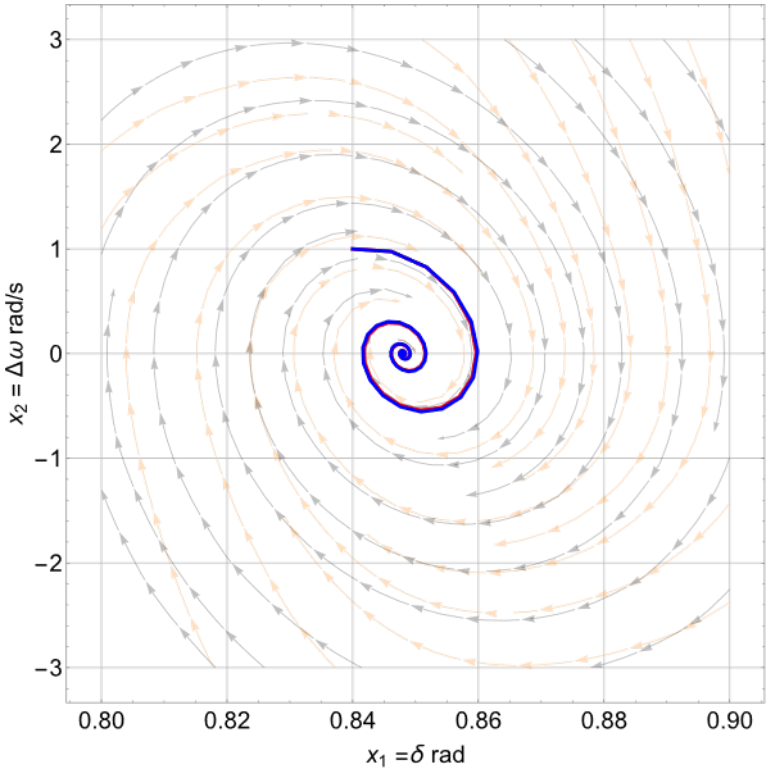

Fig. 5.13. VSG trajectories and dynamics in third case. Initial point is ($\delta = 0.84\ rad$, $\omega = 1\ rad/s$). Conventional inertia controller in blue and proposed EVIC in red.

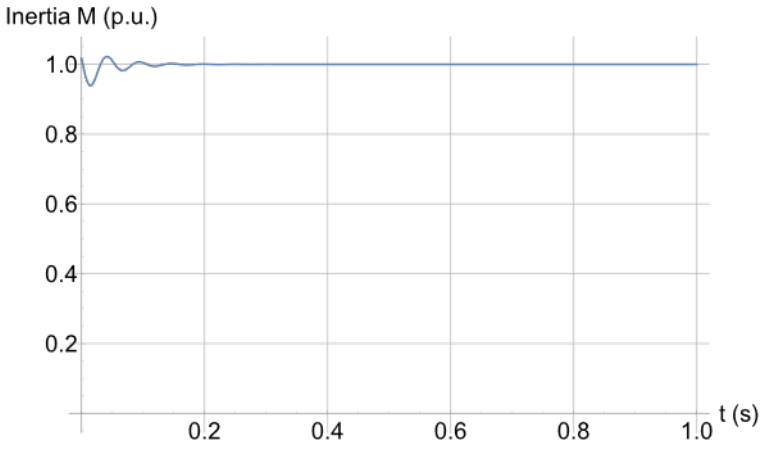

Fig. 5.14. Alternating inertia profile of proposed EVIC in third case

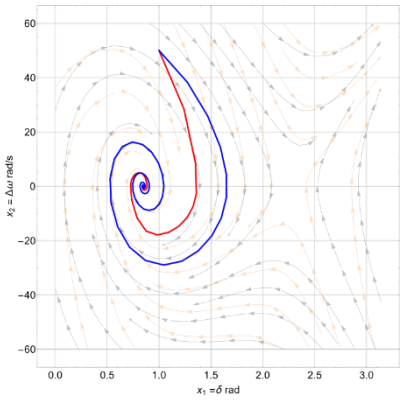

VSG trajectories and dynamics in first case. Initial point is ($\delta = 1\,rad,\ \omega = 50\,rad/s$). Conventional inertia controller in blue and proposed EVIC in red.

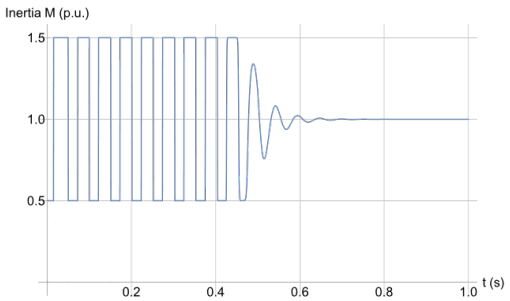

Alternating inertia profile of proposed EVIC in case (1) showing reduced oscillation.

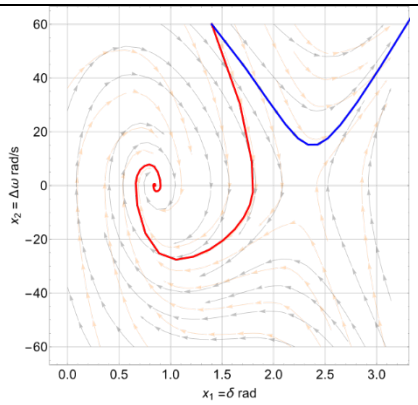

VSG trajectories and dynamics in second case. Initial point is ($\delta = 1.4\,rad,\ \omega = 60\,rad/s$). Conventional inertia controller in blue and proposed EVIC in red.

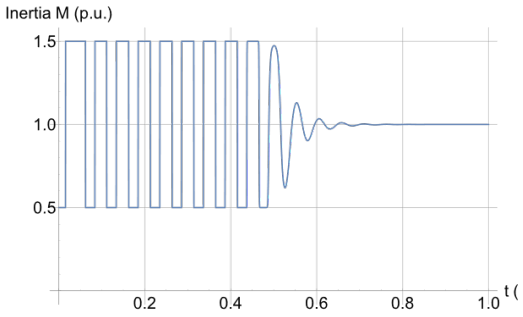

Alternating inertia profile of proposed EVIC in case (2) showed increase region of asymptotic stability

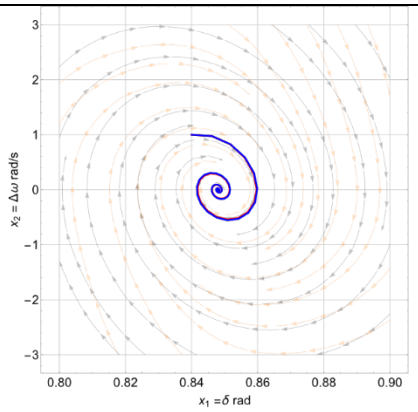

VSG trajectories and dynamics in third case. Initial point is ($\delta = 0.84\,rad,\ \omega = 1\,rad/s$). Conventional inertia controller in blue and proposed EVIC in red.

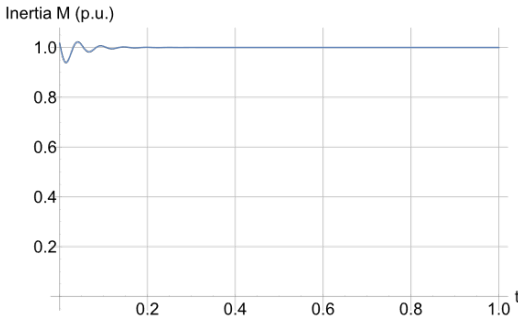

Alternating inertia profile of proposed EVIC in case (3) showing response to small disturbances

Fig. 5. 15. Summary of VSG dynamics at all cases

5. 5. Simulation results

Simulation of the proposed controller is done to verify its performance. A VSG is connected to an infinite bus using a transformer and a double circuit transmission line, as shown in Fig. 5.16. The per unit voltage of the infinite bus is set to be 1 p.u. while the terminal per unit voltage of the VSG is set to $1.05\,\mathrm{p.u.}$ The per unit reactance of the converter's output filter is $\mathrm{j}0.2\ \mathrm{p.u.}$, the transformer reactance is $\mathrm{j}0.1$ p.u. and the reactance of each transmission line is $\mathrm{j}0.4\ \mathrm{p.u.}$ The VSG inertia coefficient is $\mathrm{M} = \frac{10}{377}$. VSG reference power is 0.8 p.u. The base voltage is 13.8 kV, and the base power is 100 MVA. The single line diagram of the system is shown in Fig. 5.17. and the parameters are listed in Table 5.2.

The system model under conventional virtual inertia controller is given by:

$$\dot{\delta} = \omega$$
$$\dot{\omega} = \frac{377}{10}\,(0.8 - 2.10\,Sin(\delta) - 0.1\omega) \tag{5.8}$$

Also, the system model under EVIC and system model is given by:

$$\dot{\delta} = \omega$$
$$\dot{\omega} = \frac{377}{10 + 5\tanh(100\,\Delta P\,\omega)}(0.8 - 2.10\,Sin(\delta) - 0.1\omega) \tag{5.9}$$

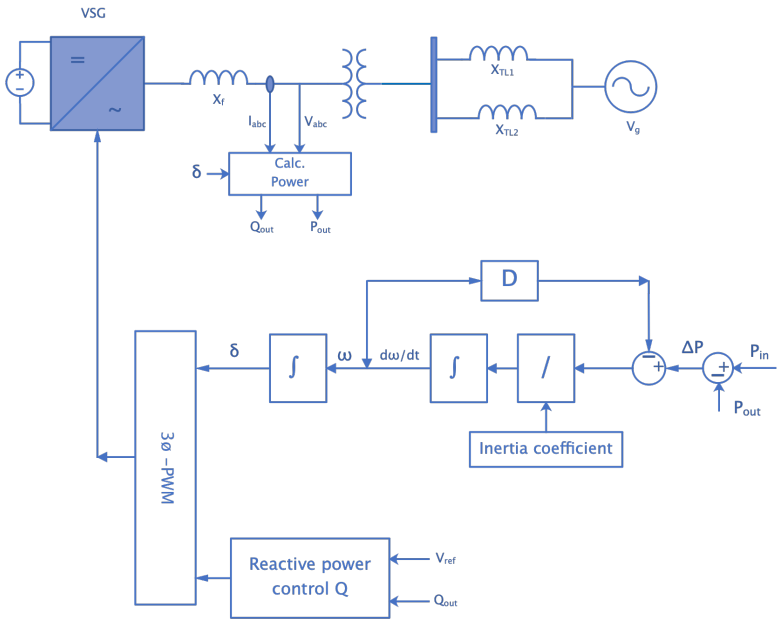

Fig. 5.16. System of VSG connect to infinite bus

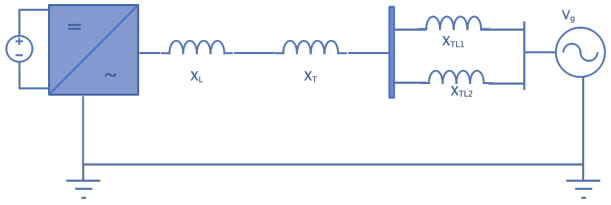

Fig. 5.17. System single line diagram

The adaptive performance of the proposed controller is evaluated here using the three cases mentioned in the previous section. In every case, the exact network is simulated twice, once with the conventional inertia controller and the other with the proposed EVIC controller, while keeping all other parameters unchanged.

In the first case, the converter is connected to the infinite bus and its reference power is set to 0.8 p.u. the initial power angle $\delta_o = 0\,rad$ and the frequency deviation from infinite bus frequency $\omega_o = 10\,rad\,/s$. This demonstrates the case where the VSG is subjected to a large load disturbance. The results shown in Fig. 5.18 prove the validity and superiority of the proposed controller. Compared with the conventional controller, the

overshoot/undershoot of the power angle is reduced by 30% while the oscillation and transient time is reduced by more than 50% from 2.5 s using conventional controller to 1 s using the proposed EVIC, as shown in Fig. 5.18 (a). Similarly, both oscillation and transient time in frequency deviation of the VSG are reduced by 50%, as shown in Fig. 5.18 (b). This is translated as reduction in the oscillation of the VSG output power as shown in Fig. 5.18 (c). The proposed controller was not only effective in quickly damping the oscillation and shorting the transient time of the VSG, but also was able to do so with significant reduction in the amplitude of the overshoot/undershoot of the it output power. In other words, the proposed controller was able to combine the merits of the low inertia systems which have short transient time, and the high inertia systems have lower oscillation amplitude. The frequency – power angle trajectories and as well as the resultant variation in the VSG inertia coefficient are shown in Fig. 5.18 (d) and (e) respectively which agree with the theoretical and mathematical model derived in the previous sections.

Table 5.2. VSG simulation parameters

Parameter	Value
Virtual input reference power P_m	0.8 p. u.
Base power S	100 MVA
Grid line voltage v_g	13.8 kV
Power angle at steady state δ	0.3908 rad
Grid power angle δ_g	0 rad
Total Line impedance	j0.5 p. u.
Infinite bus voltage v_g	1 p. u.
VSG voltage v_g	1.05 p. u.
Damping constant D	0.1
Inertial Constant M_{nom} normalized	5 s
Inertial Constant M_{min} normalized	2.5 s
Inertial Constant M_{max} normalized	7.5 s
Simulation time step	10 us

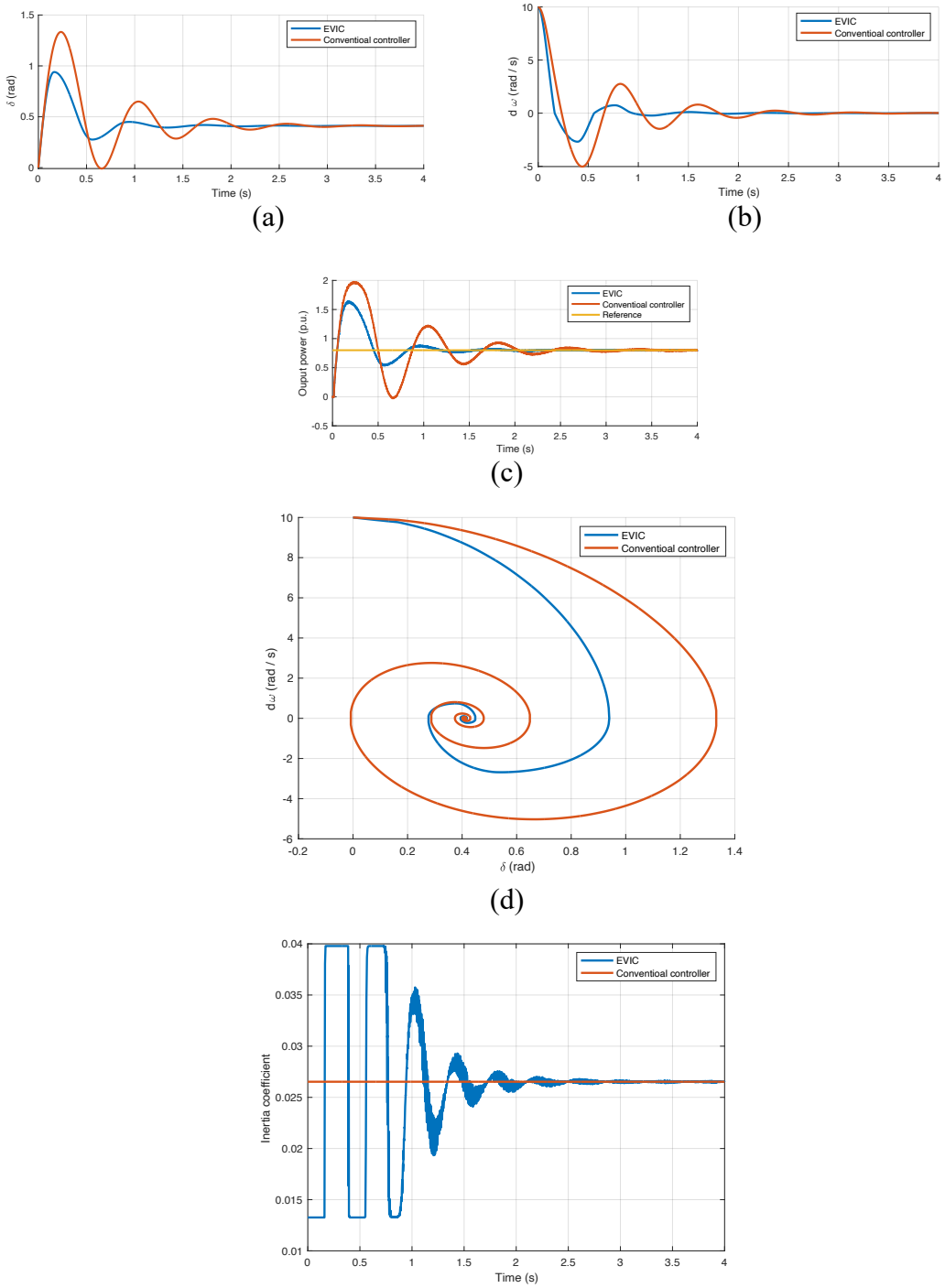

Fig. 5.18. VSG converter performance under large disturbance, case I (orange is conventional inertia controller and blue is EVIC); (a) VSG power angle vs. time; (b) VSG frequency deviation vs. time; (c) VSG output power; (d) VSG power angle – frequency trajectory; (e) VSG inertia coefficient.

The second case is considered to demonstrate the advantage of the proposed controller in increasing the VSG stability range, in comparison with the conventional controllers. In this case, the initial power angle is set to $\delta_o = 0\ rad$ and the frequency deviation from the infinite bus frequency is set to $\omega_o = 15\ rad/s$. The results are shown in Fig. 5.19. The conventional inertia controller was not able to bring the VSG back to stability as clearly shown in its power angle and frequency, Fig. 5.19 (a) and (b) respectively. On the other hand, the proposed controller under the same conditions was able to bring the VSG back to it steady state operating point δ_o without compromising neither power oscillation nor the transient time. The resultant output power in both cases is shown in Fig. 5.19 (c). The frequency – power angle trajectories and as well as the resultant variation in the VSG inertia coefficient are shown in Fig. 5.19 (d) and (e) respectively. It is worth mentioning that for the proposed EVIC controller to maintain system stability, it had to aggressively change the inertial coefficient for longer time between its maximum and minimum values before entering its linear region, as shown in Fig. 5.519 (e).

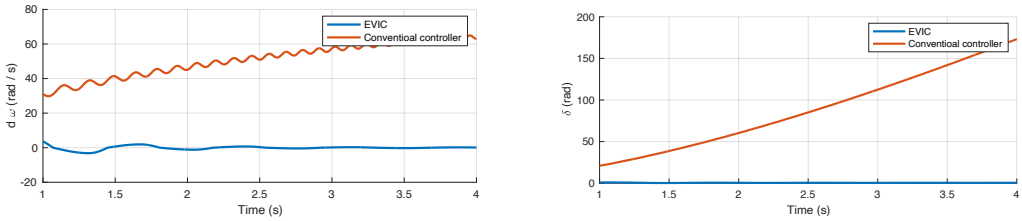

(a)

(b)

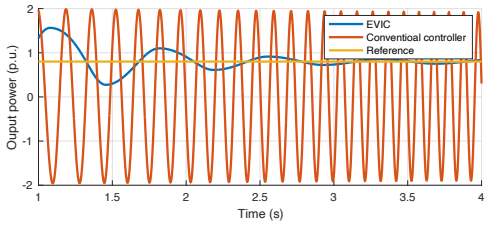

(c)

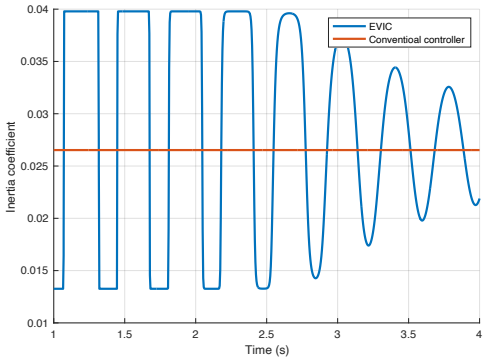

(d)

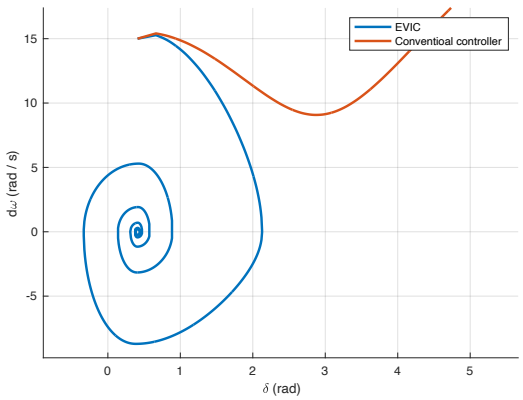

(e)

Fig. 5.19. VSG converter performance under large disturbance, case II (orange is conventional inertia controller and blue is EVIC); (a) VSG power angle vs. time; (b) VSG frequency deviation vs. time; (c) VSG output power; (d) VSG power angle – frequency trajectory; € VSG inertia coefficient.

Finally, the third case is when the VSG is subjected to small load disturbance. Here the power reference is increased by 1% from its original value 0.8 p.u. the initial power angle $\delta_o = 0.3908\, rad$ and the frequency deviation from infinite bus frequency $\omega_o = 0\, rad\ /s$. The results shown in Fig. 5.20 (a) to (e) show that both conventional inertia controller and the proposed controller perform identically when being subjected to small amplitude disturbances. As discussed, this is an advantage of the proposed controller. That is, from small-signal point of view, the proposed controller has as well-defined inertia as opposed to other alternating inertia controller. Fig. 5.20 (e) shows a very small variation around the nominal inertia coefficient value which is identical to its value in the conventional controller. Hence, it can be assumed constant in linearization. This means that all linearized models, analysis, and results are valid under the proposed controller, which saves time and effort that would have to be used to build other linear models and study their stability boundaries and so on.

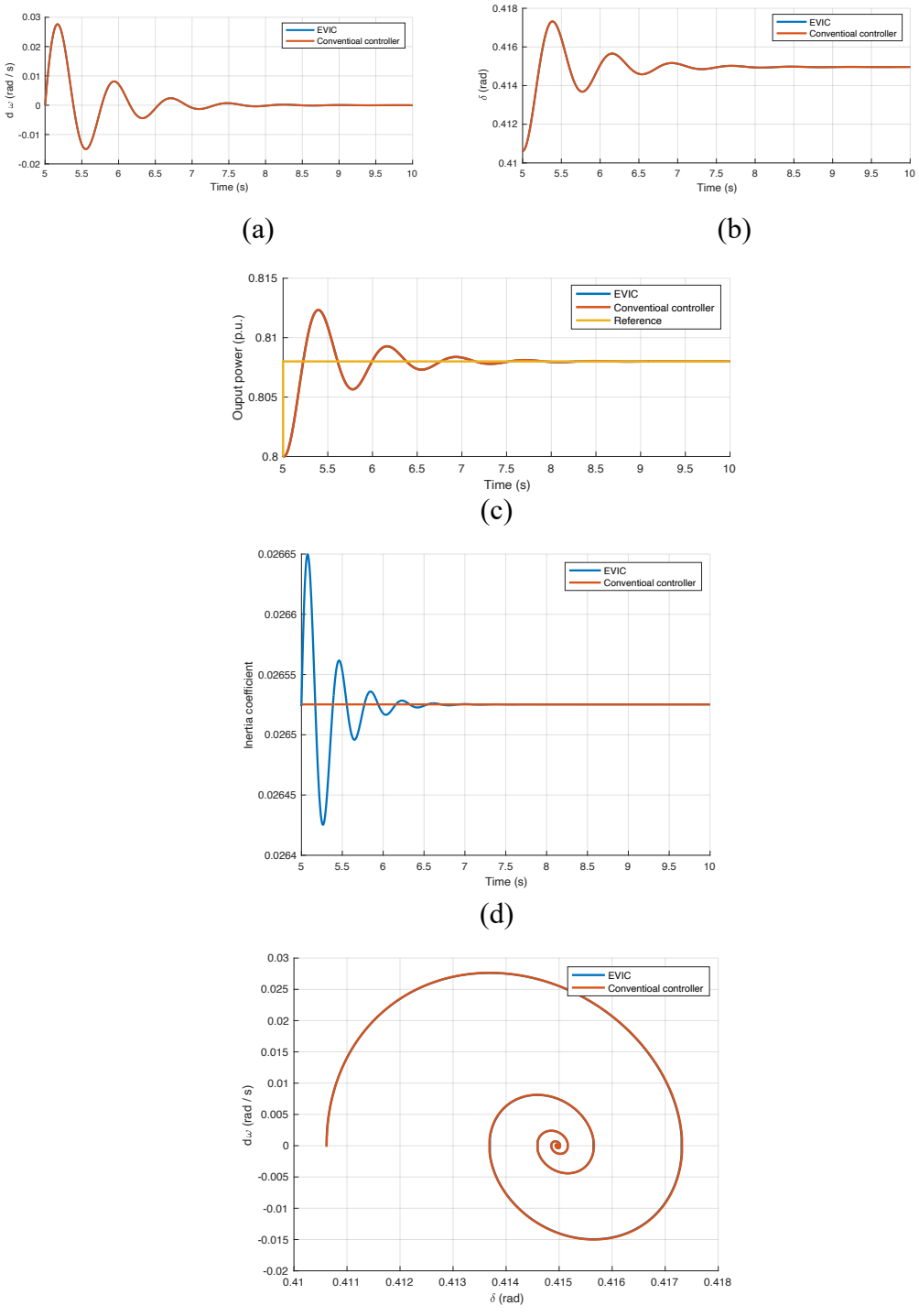

Fig. 5.20. VSG converter performance under small disturbance, case III (orange is conventional inertia controller and blue is EVIC); (a) VSG power angle vs. time; (b) VSG frequency deviation vs. time; (c) VSG output power; (d) VSG power angle – frequency trajectory; (e) VSG inertia coefficient.

6. Conclusion and Future Work

6. 1. Conclusion

The legacy power system is steadily transforming into one having more power electronics converters fed from RESs. In this new system, the conventional large-scale utility grid has been broken down into smaller interconnected MGs which are more suitable for taking advantage of the distributed nature of RES. However, PE converters, fed from RESs in these MGs, do not show the same inertia as SG did in the legacy power system. Therefore, PE converters need to be controlled using virtual inertia techniques and become VSGs. This is done to maintain the operational behavior of the legacy power system. This means maintaining the concept of the infinite (slack) bus that was used in power system stability analysis.

A MG system is modeled here without assuming the existence of an infinite bus or limiting it to only two parallel VSGs; the concept can be extended to n number of VSGs. This new concept models the characteristics that are unique to VSGs such as the implementation of a dc-link based inertia.

Due to the relatively small size of MGs, they are more vulnerable to large amplitude disturbances imposed by the loss of one of the DGs (VSGs), a significant load transient, or line fault. Due to the large number of connected VSGs, a stability study of such MGs using linear techniques becomes inaccurate and leads to more conservative boundaries at best.

The nonlinear stability study of a multi-VSG MG is provided in this work. The stability boundary of a given MG is quantitatively measured by calculating its maximum clearing time t_{cr} under a given fault. Two methods are introduced in this work:

1. First, is a Lyapunov based method, in which, a systematic approach to construct system energy function in the sense of Lyapunov is introduced. It eases the calculations required when n number of DGs are considered. The implementation of this method involves two steps; First, the MG model is used to derive the Lyapunov energy function for multiple interconnected VSGs based on Popov's criterion (KYP criterion). Second, different energy levels are calculated based on nearby unstable operating points of all VSGs. The resultant minimum energy level then dictates the maximum frequency deviation $\boldsymbol{\Delta\omega}$ and power angle difference $\boldsymbol{\delta}$ with respect to rotating frame before the MG under investigation becomes unstable. This energy level defines the area of attraction within which the MG is stable. The critical clearing time $\boldsymbol{t_{cr}}$ is then calculated by integrating the derived Lyapunov function at that energy level. The validity of the introduced model and approach is discussed in detail and proven for a single VSG and then extended for multiple VSGs.

2. The second method is a proposed convex hull-based trajectory reversing. It is used to estimate and enlarge the ROA of grid connected VSG. The algorithm and the flow chart of the proposed method is developed and discussed in detail. It starts by generating a family of reversed trajectories that are initiated close to the VSG(s) equilibrium points. Then, convex hull algorithm finds the minimum region that contains all these trajectories. Finally, at progressive time steps, the algorithm checks if the faulted trajectory is still within the convex region. The time the faulted trajectory takes to reach any of the region edges is the system's $\boldsymbol{t_{cr}}$. Moreover, this work proposed a new technique to define the set of initial points needed by the algorithm. The proposed technique provides an easy and direct method that balances the computational time with the number of initial points and their corresponding trajectories. It ensures uniform distribution of the initial points despite the ROA over their targeted number.

A case study is conducted to validate the algorithm performance and its estimated ROA. The algorithm was able to provide accurate prediction of the network t_{cr} under the given fault. It proves the validity of the algorithm without relying on finding a specific Lyapunov

function which can be challenging, especially with the increasing complexity of modern power system networks and their components.

Finally, to increase the MG stability and its area of attraction, a modified virtual inertia controlled EVIC is proposed. It adopts the alternating inertia control technique which changes the converter's inertia between two levels to quickly damp frequency and power oscillations. The proposed EVIC improves on that concept by adding three different modes of inertia alternation.

- The first mode is equal to converter nominal inertia defined by desired system response to small disturbances.
- The second mode varies the inertia coefficient of a given VSG linearly in proportion to the amount of applied large disturbances.
- The third mode provides a hard switching between two levels of inertia to quickly bring the system closer to its stability point when VSG is subjected to very large disturbances.

Moreover, the proposed control is implemented using smooth continuous equation unlike other techniques which uses discontinuous functions or complicated artificial intelligence algorithms. This is of importance when system nonlinear stability study is performed. The results show the validity of the proposed controller in not only improving system dynamic responses but also increasing the MG overall area of attraction and hence its stability boundaries.

The main contributions of this work can be summarized as follows:

- Providing a large-signal stability study of power electronics dominated MG based on Popov's multivariable criterion which systematically constructs the Lyapunov function. Then estimation of the MG region of attraction (stability margins) is done based on the nearest unstable point. This is used to calculate the critical time of an MG in the presence of faults.
- Proposing an alternative method to study the large signal stability of power electronic dominated MGs. The proposed method and algorithm can be applied to any MGs regardless of its construction or model. moreover, the proposed

method defines a fast and systematic way to solve its initial points problem and to reduce them to increase computational efficiency.

- Proposing a new enhanced virtual inertia controller EVIC which can further improve the MG stability margins and reduced power oscillations. The proposed controller provides adaptive alternating inertial dynamics in proportion to the applied disturbances.

6. 2. Future work

This work focused on finding direct systematic techniques to quantify the large signal stability of any given MG. Lyapunov function, once it is derived, can be directly used to determine the limits on the MG dynamics before spiralling out of its stable region. Trajectory reversing method does the same but without imposing any constrains on MG's model or dimensions i.e., number of interconnected VSGs. A future extension of this work is to use convex hull-based trajectory reversing method and Taguchi method to study the stability of MG with higher VSGs. For such high number of interconnected VSGs, the number of possible faults increases rapidly, making studying the MG stability a time consuming and cumbersome process.

While trajectory reversing technique can be applied to any number of VSGs with advanced and complex control schemes. Taguchi method can be applied to significantly reduce the number of faults scenarios by only considering the ones that will have the highest impact on the stability.

This method is originally developed for quality control process as it can define the manufacturing variables that have the highest impact the product quality. It is found later to be effective in many other applications. It is considered here as a natural progression to this work as it is a numerical based method that can be implemented in conjunction with the reverse trajectory method to form a software stability engine, that can quickly; 1) define the stability region, 2) define the most vulnerable points in the MG and 3) generate stability report in computationally efficient way.

Moreover, the future extension of this work would include investigating the effectiveness of the proposed EVIC controller against IEEE 1547, LVRT especially when

it comes to its voltage ride through capability. Another area of reach is to extend the stability study to consider constant power loads effect on the MG dynamics and stability instead of the constant impedance loads utilized in this study.

Publications

Under submission

1. Ahmed Sheir and V. K. Sood, "***Enhanced Virtual Inertia Controller***," *Energies 2022 (under review)*.

2. J. Patel, **Ahmed Sheir** and V. K. Sood, **"*Modified Wavelet-Based Modulation Technique for Self-Balancing High Voltage Power Converter*,"** (to be submitted)**.**

Accepted

1. Ahmed Sheir, Ruth Milman and V. K. Sood, "***Large Signal Stability of Grid-Tied Virtual Synchronous Generator Using Trajectory Reversing***," IEEE Electrical Power and Energy Conference (EPEC 2022).

2. Ahmed Sheir and V. K. Sood, "***Effect of Low Pass Filter in Governor Model on Large Signal Stability of Virtual Synchronous Generator***," IEEE 12th International Symposium on Power Electronics for Distributed Generation Systems, (PEDG 2021).

3. J. Patel, **Ahmed Sheir** and V. K. Sood**, "*Impact of Sampling Time of Digital Controllers on The Harmonic Spectrum in Power Converters*,"** IEEE 12th International Symposium on Power Electronics for Distributed Generation Systems, (PEDG 2021).

4. Ahmed Sheir and V. K. Sood, "***Dual-Input H-bridge Based Three-Phase Cascaded Multilevel Converter for Utility-Scale Battery Applications***," IEEE Electrical Power and Energy Conference (EPEC), ON, 2021.

5. Youssef El Haj, **Ahmed Sheir**, Ruth Milman and V. K. Sood, "***Design of a Nonlinear Controller for a Two-Stage DC-AC Converter For DC-Link Drive Applications***," IEEE Electrical Power and Energy Conference (EPEC), ON, 2021.

6. Youssef El Haj, **Ahmed Sheir**, Ruth Milman and V. K. Sood, "***Robust Integral Sliding Mode Control of Non-minimum Phase DC-DC Converters***," 2020 IEEE Electrical Power and Energy Conference (EPEC), Edmonton, ON, 2020.

7. Ahmed Sheir and V. K. Sood, "***Cascaded Modular Converter with Reduced Output Voltage Ripple***," 2019 IEEE Electrical Power and Energy Conference (EPEC), Montreal, ON, 2019.

8. Ali Sunbul, **Ahmed Sheir** and V. K. Sood, "***High Performance Multilevel Power Factor Correction Boost-Buck Converter***," 2019 IEEE Electrical Power and Energy Conference (EPEC), Montreal, ON, 2019.

7. References

[1] P. Kundur, *Power System Stability and Control*, 1st Edition. New York: McGraw-Hill Education, 1994.

[2] H. Saadat, *Power System Analysis*, 3rd edition. United States: PS AS, 2010.

[3] H. Holttinen *et al.*, "System impact studies for near 100% renewable energy systems dominated by inverter based variable generation," *IEEE Trans. Power Syst.*, pp. 1–1, 2020, doi: 10.1109/TPWRS.2020.3034924.

[4] V. K. Sood, *HVDC and FACTS Controllers: Applications of Static Converters in Power Systems*. Springer US, 2004. doi: 10.1007/b117759.

[5] M. Hoffmann *et al.*, "Grid Code-Dependent Frequency Control Optimization in Multi-Terminal DC Networks," *Energies*, vol. 13, no. 24, Art. no. 24, Jan. 2020, doi: 10.3390/en13246485.

[6] J. Fang, H. Li, Y. Tang, and F. Blaabjerg, "On the Inertia of Future More-Electronics Power Systems," *IEEE J. Emerg. Sel. Top. Power Electron.*, vol. 7, no. 4, pp. 2130–2146, Dec. 2019, doi: 10.1109/JESTPE.2018.2877766.

[7] J. Fang, H. Li, Y. Tang, and F. Blaabjerg, "Distributed Power System Virtual Inertia Implemented by Grid-Connected Power Converters," *IEEE Trans. Power Electron.*, vol. 33, no. 10, pp. 8488–8499, Oct. 2018, doi: 10.1109/TPEL.2017.2785218.

[8] F. Blaabjerg, R. Teodorescu, M. Liserre, and A. V. Timbus, "Overview of Control and Grid Synchronization for Distributed Power Generation Systems," *IEEE Trans. Ind. Electron.*, vol. 53, no. 5, pp. 1398–1409, Oct. 2006, doi: 10.1109/TIE.2006.881997.

[9] G. Delille, B. Francois, and G. Malarange, "Dynamic Frequency Control Support by Energy Storage to Reduce the Impact of Wind and Solar Generation on Isolated Power System's Inertia," *IEEE Trans. Sustain. Energy*, vol. 3, no. 4, pp. 931–939, Oct. 2012, doi: 10.1109/TSTE.2012.2205025.

[10] J. Driesen and K. Visscher, "Virtual synchronous generators," in *2008 IEEE Power and Energy Society General Meeting - Conversion and Delivery of Electrical Energy in the 21st Century*, Jul. 2008, pp. 1–3. doi: 10.1109/PES.2008.4596800.

[11] T. Loix, S. D. Breucker, P. Vanassche, J. V. den Keybus, J. Driesen, and K. Visscher, "Layout and performance of the power electronic converter platform for the VSYNC project," *2009 IEEE Bucharest PowerTech*, Jun. 2009, pp. 1–8. doi: 10.1109/PTC.2009.5282160.

[12] M. P. N. van Wesenbeeck, S. W. H. de Haan, P. Varela, and K. Visscher, "Grid tied converter with virtual kinetic storage," in *2009 IEEE Bucharest PowerTech*, Jun. 2009, pp. 1–7. doi: 10.1109/PTC.2009.5282048.

[13] H. Beck and R. Hesse, "Virtual synchronous machine," *2007 9th International Conference on Electrical Power Quality and Utilisation*, Oct. 2007, pp. 1–6. doi: 10.1109/EPQU.2007.4424220.

[14] Q. Zhong and G. Weiss, "Synchronverters: Inverters That Mimic Synchronous Generators," *IEEE Trans. Ind. Electron.*, vol. 58, no. 4, pp. 1259–1267, Apr. 2011, doi: 10.1109/TIE.2010.2048839.

[15] K. Visscher and S. W. H. D. Haan, "Virtual synchronous machines (VSG's) for frequency stabilisation in future grids with a significant share of decentralized generation," *CIRED Seminar 2008: SmartGrids for Distribution*, Jun. 2008, pp. 1–4.

[16] V. Karapanos, “Testing a Virtual Synchronous Generator in a Real Time Simulated Power System,” p. 7.
[17] M. Albu, A. Nechifor, and D. Creanga, “Smart storage for active distribution networks estimation and measurement solutions,” *2010 IEEE Instrumentation Measurement Technology Conference Proceedings*, May 2010, pp. 1486–1491. doi: 10.1109/IMTC.2010.5488083.
[18] T. V. Van *et al.*, “Virtual synchronous generator: An element of future grids,” in *2010 IEEE PES Innovative Smart Grid Technologies Conference Europe (ISGT Europe)*, Oct. 2010, pp. 1–7. doi: 10.1109/ISGTEUROPE.2010.5638946.
[19] M. Albu *et al.*, “Measurement and remote monitoring for virtual synchronous generator design,” in *2010 IEEE International Workshop on Applied Measurements for Power Systems*, Sep. 2010, pp. 7–11. doi: 10.1109/AMPS.2010.5609328.
[20] M. Albu, M. Calin, D. Federenciuc, and J. Diaz, “The measurement layer of the Virtual Synchronous Generator operation in the field test,” *2011 IEEE International Workshop on Applied Measurements for Power Systems (AMPS)*, Sep. 2011, pp. 85–89. doi: 10.1109/AMPS.2011.6090438.
[21] V. Karapanos, S. de Haan, and K. Zwetsloot, “Real time simulation of a power system with VSG hardware in the loop,” *IECON 2011 - 37th Annual Conference of the IEEE Industrial Electronics Society*, Nov. 2011, pp. 3748–3754. doi: 10.1109/IECON.2011.6119919.
[22] Y. Chen, R. Hesse, D. Turschner, and H. Beck, “Improving the grid power quality using virtual synchronous machines,” in *2011 International Conference on Power Engineering, Energy and Electrical Drives*, May 2011, pp. 1–6. doi: 10.1109/PowerEng.2011.6036498.
[23] Y. Hirase, K. Abe, K. Sugimoto, and Y. Shindo, “A grid-connected inverter with virtual synchronous generator model of algebraic type,” *Electr. Eng. Jpn.*, vol. 184, no. 4, pp. 10–21, 2013, doi: 10.1002/eej.22428.
[24] J. Alipoor, Y. Miura, and T. Ise, “Power System Stabilization Using Virtual Synchronous Generator With Alternating Moment of Inertia,” *IEEE J. Emerg. Sel. Top. Power Electron.*, vol. 3, no. 2, pp. 451–458, Jun. 2015, doi: 10.1109/JESTPE.2014.2362530.
[25] K. Sakimoto, Y. Miura, and T. Ise, “Stabilization of a power system with a distributed generator by a Virtual Synchronous Generator function,” *8th International Conference on Power Electronics - ECCE Asia*, May 2011, pp. 1498–1505. doi: 10.1109/ICPE.2011.5944492.
[26] J. Alipoor, Y. Miura, and T. Ise, “Distributed generation grid integration using virtual synchronous generator with adoptive virtual inertia,” in *2013 IEEE Energy Conversion Congress and Exposition*, Sep. 2013, pp. 4546–4552. doi: 10.1109/ECCE.2013.6647309.
[27] J. Alipoor, Y. Miura, and T. Ise, “Voltage sag ride-through performance of Virtual Synchronous Generator,” *2014 International Power Electronics Conference (IPEC-Hiroshima 2014 - ECCE ASIA)*, May 2014, pp. 3298–3305. doi: 10.1109/IPEC.2014.6870160.
[28] Jia Liu, Y. Miura, and T. Ise, “Dynamic characteristics and stability comparisons between virtual synchronous generator and droop control in inverter-based distributed

generators," in *2014 International Power Electronics Conference (IPEC-Hiroshima 2014 - ECCE ASIA)*, May 2014, pp. 1536–1543. doi: 10.1109/IPEC.2014.6869789.
[29] R. Rosso, S. Engelken, and M. Liserre, "Robust Stability Analysis of Synchronverters Operating in Parallel," *IEEE Trans. Power Electron.*, vol. 34, no. 11, pp. 11309–11319, Nov. 2019, doi: 10.1109/TPEL.2019.2896707.
[30] R. Rosso, J. Cassoli, G. Buticchi, S. Engelken, and M. Liserre, "Robust Stability Analysis of LCL Filter Based Synchronverter Under Different Grid Conditions," *IEEE Trans. Power Electron.*, vol. 34, no. 6, pp. 5842–5853, Jun. 2019, doi: 10.1109/TPEL.2018.2867040.
[31] H. R. Chamorro *et al.*, "Analysis of the Gradual Synthetic Inertia Control on Low-Inertia Power Systems," in *2020 IEEE 29th International Symposium on Industrial Electronics (ISIE)*, Jun. 2020, pp. 816–820. doi: 10.1109/ISIE45063.2020.9152448.
[32] P. Unruh, M. Nuschke, P. Strauß, and F. Welck, "Overview on Grid-Forming Inverter Control Methods," *Energies*, vol. 13, no. 10, Art. no. 10, Jan. 2020, doi: 10.3390/en13102589.
[33] M. Kabalan, P. Singh, and D. Niebur, "Nonlinear Lyapunov Stability Analysis of Seven Models of a DC/AC Droop Controlled Inverter Connected to an Infinite Bus," *IEEE Trans. Smart Grid*, vol. 10, no. 1, pp. 772–781, Jan. 2019, doi: 10.1109/TSG.2017.2752146.
[34] D. Pan, X. Wang, F. Liu, and R. Shi, "Transient Stability of Voltage-Source Converters With Grid-Forming Control: A Design-Oriented Study," *IEEE J. Emerg. Sel. Top. Power Electron.*, vol. 8, no. 2, pp. 1019–1033, Jun. 2020, doi: 10.1109/JESTPE.2019.2946310.
[35] H. Cheng, Z. Shuai, C. Shen, X. Liu, Z. Li, and Z. J. Shen, "Transient Angle Stability of Paralleled Synchronous and Virtual Synchronous Generators in Islanded Microgrids," *IEEE Trans. Power Electron.*, vol. 35, no. 8, pp. 8751–8765, Aug. 2020, doi: 10.1109/TPEL.2020.2965152.
[36] N. Kant, R. Mukherjee, D. Chowdhury, and H. K. Khalil, "Estimation of the Region of Attraction of Underactuated Systems and Its Enlargement Using Impulsive Inputs," *IEEE Trans. Robot.*, vol. 35, no. 3, pp. 618–632, Jun. 2019, doi: 10.1109/TRO.2019.2893599.
[37] Y. Chen, M. Tanaka, K. Tanaka, and H. O. Wang, "Stability Analysis and Region-of-Attraction Estimation Using Piecewise Polynomial Lyapunov Functions: Polynomial Fuzzy Model Approach," *IEEE Trans. Fuzzy Syst.*, vol. 23, no. 4, pp. 1314–1322, Aug. 2015, doi: 10.1109/TFUZZ.2014.2347993.
[38] M. Mao, J. Hu, Y. Ding, and L. Chang, "Multi-parameter Adaptive Power Allocation Strategy for Microgrid with Parallel PV/Battery-VSGs," in *2019 IEEE Energy Conversion Congress and Exposition (ECCE)*, Sep. 2019, pp. 2105–2111. doi: 10.1109/ECCE.2019.8913012.
[39] T. Kerdphol, M. Watanabe, K. Hongesombut, and Y. Mitani, "Self-Adaptive Virtual Inertia Control-Based Fuzzy Logic to Improve Frequency Stability of Microgrid With High Renewable Penetration," *IEEE Access*, vol. 7, pp. 76071–76083, 2019, doi: 10.1109/ACCESS.2019.2920886.
[40] N. Hatziargyriou *et al.*, "Definition and Classification of Power System Stability Revisited Extended," *IEEE Trans. Power Syst.*, pp. 1–1, 2020, doi: 10.1109/TPWRS.2020.3041774.

[41] M. A. Pai and C. L. Narayana, “Stability of Large Scale Power Systems,” *IFAC Proc. Vol.*, vol. 8, no. 1, Part 2, pp. 215–224, Aug. 1975, doi: 10.1016/S1474-6670(17)67646-8.
[42] J. Machowski, J. W. Bialek, and J. Bumby, *Power System Dynamics: Stability and Control*, 2 edition. Chichester, U.K: Wiley, 2008.
[43] P. W. Sauer and M. A. Pai, *Power System Dynamics And Stability*, 1st edition. Upper Saddle River, N.J: Pearson, 1997.
[44] W. D. Stevenson, *Elements of Power System Analysis*. New York: McGraw-Hill Science/Engineering/Math, 1982.
[45] S. Sastry, *Nonlinear Systems: Analysis, Stability, and Control*, 1999 edition. New York: Springer, 1999.
[46] H. Bevrani, B. FranÃ§ois, and T. Ise, *Microgrid Dynamics and Control*. Hoboken, NJ: Wiley, 2017.
[47] S. Banerjee and G. C. Verghese, Eds., *Nonlinear Phenomena in Power Electronics: Bifurcations, Chaos, Control, and Applications*, 1 edition. New York: Wiley-IEEE Press, 2001.
[48] S. H. Strogatz, *Nonlinear Dynamics And Chaos: With Applications To Physics, Biology, Chemistry, And Engineering*, 1st edition. Cambridge, Mass: Westview Press, 2001.
[49] H. Khalil, *Nonlinear Systems*, 3rd edition. Upper Saddle River, N.J: Pearson, 2001.
[50] D. Jordan and P. Smith, *Nonlinear Ordinary Differential Equations: An Introduction for Scientists and Engineers*, Fourth edition. Oxford England: Oxford University Press, 2007.
[51] J. Liu, Y. Miura, H. Bevrani, and T. Ise, “Enhanced Virtual Synchronous Generator Control for Parallel Inverters in Microgrids,” *IEEE Trans. Smart Grid*, vol. 8, no. 5, pp. 2268–2277, Sep. 2017, doi: 10.1109/TSG.2016.2521405.
[52] Y. Ling, Y. Li, Z. Yang, and J. Xiang, “A Dispatchable Droop Control Method for Distributed Generators in Islanded AC Microgrids,” *IEEE Trans. Ind. Electron.*, pp. 1–1, 2020, doi: 10.1109/TIE.2020.3013547.
[53] E. Kreyszig, *Advanced Engineering Mathematics*, 10 edition. Hoboken, NJ: Wiley, 2011.
[54] N. S. Nise, *Control Systems Engineering, 7th Edition*, 7th edition. Wiley, 2014.
[55] Y. Huang, X. Zhai, J. Hu, D. Liu, and C. Lin, “Modeling and Stability Analysis of VSC Internal Voltage in DC-Link Voltage Control Timescale,” *IEEE J. Emerg. Sel. Top. Power Electron.*, vol. 6, no. 1, pp. 16–28, Mar. 2018, doi: 10.1109/JESTPE.2017.2715224.
[56] N. Kant, D. Chowdhury, R. Mukherjee, and H. K. Khalil, “An algorithm for enlarging the region of attraction using trajectory reversing,” in *2017 American Control Conference (ACC)*, May 2017, pp. 4171–4176. doi: 10.23919/ACC.2017.7963596.
[57] *Nonlinear Dynamical Systems and Control*. 2008. Accessed: Nov. 25, 2020. [Online]. Available: https://press.princeton.edu/books/hardcover/9780691133294/nonlinear-dynamical-systems-and-control
[58] D. del Puerto-Flores, J. M. A. Scherpen, M. Liserre, M. M. J. de Vries, M. J. Kransse, and V. G. Monopoli, “Passivity-Based Control by Series/Parallel Damping of Single-Phase PWM Voltage Source Converter,” *IEEE Trans. Control Syst. Technol.*, vol. 22, no. 4, pp. 1310–1322, Jul. 2014, doi: 10.1109/TCST.2013.2278781.

[59] S. V. Gusev, “Kalman—Yakubovich—Popov Lemma And Hilbert’s 17th Problem∗∗Supported by SPbSU, grant 6.38.230.2015.,” *IFAC-Pap.*, vol. 48, no. 11, pp. 238–241, Jan. 2015, doi: 10.1016/j.ifacol.2015.09.190.
[60] M. A. PAI and P. G. MURTHY, “New Lyapunov functions for power systems based on minimal realizations,” *Int. J. Control*, vol. 19, no. 2, pp. 401–415, Feb. 1974, doi: 10.1080/00207177408932638.
[61] G. P. Szegö, “On a New Partial Differential Equation for the Stability Analysis of Time Invariant Control Systems,” *J. Soc. Ind. Appl. Math. Ser. Control*, vol. 1, no. 1, pp. 63–75, Jan. 1962, doi: 10.1137/0301005.
[62] G. P. Szegö and G. R. Geiss, “A Remark on ‘A New Partial Differential Equation for the Stability Analysis of Time Invariant Control Systems,’” *J. Soc. Ind. Appl. Math. Ser. Control*, vol. 1, no. 3, pp. 369–376, Jan. 1963, doi: 10.1137/0301021.
[63] “Numerical applications of Lyapunov stability theory.” https://www.infona.pl/resource/bwmeta1.element.ieee-art-000004168699 (accessed Oct. 31, 2022).
[64] R. Genesio and A. Vicino, “New techniques for constructing asymptotic stability regions for nonlinear systems,” *IEEE Trans. Circuits Syst.*, vol. 31, no. 6, p. 574, 1984.
[65] H. Miyagi and T. Taniguchi, “Lagrange-Charpit method and stability problem of power systems,” *IEE Proc. Control Theory Appl.*, vol. 128, no. 3, pp. 117–122, May 1981, doi: 10.1049/ip-d.1981.0021.
[66] J. LaSalle, “Some Extensions of Liapunov’s Second Method,” *IRE Trans. Circuit Theory*, vol. 7, no. 4, pp. 520–527, Dec. 1960, doi: 10.1109/TCT.1960.1086720.
[67] E. J. Davison and E. M. Kurak, “A computational method for determining quadratic lyapunov functions for non-linear systems,” *Automatica*, vol. 7, no. 5, pp. 627–636, Sep. 1971, doi: 10.1016/0005-1098(71)90027-6.
[68] A. N. Michel, N. R. Sarabudla, and R. K. Miller, “Stability analysis of complex dynamical systems: Some computational methods,” in *1981 20th IEEE Conference on Decision and Control including the Symposium on Adaptive Processes*, Dec. 1981, pp. 277–282. doi: 10.1109/CDC.1981.269528.
[69] J. Willems, “Direct method for transient stability studies in power system analysis,” *IEEE Trans. Autom. Control*, vol. 16, no. 4, pp. 332–341, Aug. 1971, doi: 10.1109/TAC.1971.1099743.
[70] R. Genesio, M. Tartaglia, and A. Vicino, “On the estimation of asymptotic stability regions: State of the art and new proposals,” *IEEE Trans. Autom. Control*, vol. 30, no. 8, pp. 747–755, Aug. 1985, doi: 10.1109/TAC.1985.1104057.
[71] R. Balestriero, Z. Wang, and R. G. Baraniuk, “DeepHull: Fast Convex Hull Approximation in High Dimensions,” in *ICASSP 2022 - 2022 IEEE International Conference on Acoustics, Speech and Signal Processing (ICASSP)*, May 2022, pp. 3888–3892. doi: 10.1109/ICASSP43922.2022.9746031.
[72] “DBSCAN Clustering Algorithm - File Exchange - MATLAB Central.” https://www.mathworks.com/matlabcentral/fileexchange/52905-dbscan-clustering-algorithm?s_tid=prof_contriblnk (accessed Oct. 31, 2022).
[73] H. R. Chamorro, F. R. S. Sevilla, F. Gonzalez-Longatt, K. Rouzbehi, H. Chavez, and V. K. Sood, “Innovative primary frequency control in low-inertia power systems based on wide-area RoCoF sharing,” *IET Energy Syst. Integr.*, vol. 2, no. 2, pp. 151–160, 2020, doi: 10.1049/iet-esi.2020.0001.

[74] S. D'Arco, J. A. Suul, and O. B. Fosso, "A Virtual Synchronous Machine implementation for distributed control of power converters in SmartGrids," *Electr. Power Syst. Res.*, vol. 122, pp. 180–197, May 2015, doi: 10.1016/j.epsr.2015.01.001.
[75] J. Meng, Y. Wang, C. Fu, and H. Wang, "Adaptive virtual inertia control of distributed generator for dynamic frequency support in microgrid," in *2016 IEEE Energy Conversion Congress and Exposition (ECCE)*, Sep. 2016, pp. 1–5. doi: 10.1109/ECCE.2016.7854825.